Wave and setup dynamics on fringing reefs

Mark L. Buckley

BA Oceanography (University of San Diego)

MSc Ocean Engineering (University of Rhode Island)

This thesis is presented for the degree of

Doctor of Philosophy at the University of Western Australia

UWA Oceans Institute and

School of Earth and Environment

2016

Declaration of Authorship

The work contained herein is entirely my own, except where otherwise stated. For all work that has been published or prepared for publication with other authors, I have the permission of all co-authors to include this work in my thesis and my contributions, as well as those of my co-authors are clearly indicated.

Student Signature.  **.....**

Coordinating Supervisor Signature..  **.....**

Abstract

The steep slopes and large bottom roughness of coral reefs contrast with the milder slopes and smoother bottoms of sandy beaches where most historical research on surf zone processes has been targeted. These physical characteristics of reefs may thus explicitly violate the underlying assumptions of existing surf zone models when applied to reef systems. Given the importance of surf zone dynamics to a range of physical dynamics (e.g., coastal inundation and sediment transport) and biological processes (e.g., larval and nutrient transport and dispersal), there is a need to rigorously assess existing theory and, where necessary, develop new theory appropriate for reef environments. This thesis was directed at addressing these open questions through three chapters. In chapter two, the suitability of commonly used numerical models in steep-slope reef environments was assessed using existing laboratory observations on a smooth reef profile. In chapter three, the dynamics of wave setup were evaluated with higher spatial-resolution data collected in a 1:36 scale wave flume with a smooth bottom and characteristic fringing reef profile. Finally in chapter four, the effect of large bottom roughness on wave setup was determined by comparing the results from the smooth laboratory flume experiments with the same experiments conducted over scaled roughness elements.

In chapter two, we find that existing nearshore numerical models are capable of reproducing observations of waves and wave setup across a laboratory reef profile with reasonable accuracy, despite the steep (1:11) reef slope explicitly violating the mild-slope and other fundamental assumptions that underpin the numerical models. However, a partial explanation for the good agreement with observations reported in chapter two, and elsewhere, may be owing to the tuning of empirical coefficients and hence not be physically meaningful. Indeed, in many cases tuning model parameters to best reproduce the observed wave height decay resulted in a reduction in the accuracy of wave setup predictions, which indicates a fundamental breakdown in the dynamical relationship between the predicted radiation stress gradients and the observed wave setup. However, as detailed surf zone measurements were not available, it was not possible to further evaluate the details of wave and setup dynamics.

The general lack of detailed surf zone measurements on reefs was rectified by conducting the high-resolution laboratory experiments detailed in chapters three and four. In these chapters, we utilized new datasets to evaluate the time-averaged cross-shore momentum equation from observations of water levels and velocities, rather than

the traditional approach of using empirical models to predict wave transformation through the surf zone. For runs without roughness (chapter three), the momentum equation collapsed to a balance between pressure and radiation stress gradients, and revealed a significant underestimation of wave setup when radiation stress gradients were approximated from observations using linear wave theory alone. Including the radiation stress contribution from wave rollers was found to reduce the under prediction of setup from 21% to only 3% on average.

Using an array of roughness elements affixed to the same reef profile as in chapter three, the influence of the large bottom roughness typical of coral reefs was evaluated in chapter four. Despite the presence of roughness modifying the setup profiles near the reef crest and changing the partitioning between wave and bottom stress forces, roughness did not affect the net setup on the reef flat. These results are in contrast to the often reported large increases in setup predicted by the presence of roughness in numerical models. The consistency between the setup on the smooth and rough laboratory profiles is accounted for by an 18% (on average) reduction in setup generated by radiation stress gradients in the rough versus smooth cases coupled with a 16% (on average) increase in setup generation by bottom roughness resistance forces in the rough cases. These results highlight the need for precise predictions of the wave field and the time-averaged bottom stress to accurately predict the setup response on steep-slope reefs. This thesis contributes to the understanding and prediction of the complex wave and setup dynamics on steep slopes and in areas of large bottom roughness.

Table of Contents

Declaration of Authorship....3
Abstract....v
Table of Contents....vii
List of tables....xi
List of figures....xiii
Publications arising from this thesis....xxi
Acknowledgements....xxiii
Notation....xxv
1. General Introduction....27

1.1. Introduction....27
1.2. Background....27
1.3. Motivation and Aims....29
1.4. Thesis Structure....29

2. Evaluation of nearshore wave models in steep reef environments....31

2.1. Abstract....31
2.2. Introduction....31
2.3. Numerical wave models....33

2.3.1. Wave breaking....35
2.3.2. Bottom stress....38

2.4. Model application to a laboratory reef....38

2.4.1. Model setup....39
2.4.2. Data processing and performance metrics....40

2.5. Results....43

2.5.1. Test no. 35....43
2.5.2. Summary of all Test conditions....47

2.6. Discussion....48

2.6.1. The role of α in SWASH....48
2.6.2. The role of the breaker parameter γ (XBeach and SWAN)....49
2.6.3. Prediction of α and γ....52

2.7. Conclusions....54

3. Dynamics of wave setup over a steeply-sloping fringing reef....57

3.1. Abstract 57
3.2. Introduction 57
3.3. Background 59
3.3.1. Cross-shore mean momentum equation 59
3.3.2. Radiation stresses 60
3.3.3. Wave roller theory 61
3.4. Methods 62
3.4.1. Experimental setup 62
3.4.2. Evaluation of the mean momentum equation 64
3.4.3. Uncertainty estimation 67
3.5. Results 68
3.5.1. Wave transformation 68
3.5.2. Radiation stresses, momentum balances, and setup/setdown 70
3.5.3. Parameterization of the wave roller model 76
3.6. Discussion 79
3.7. Conclusions 83
3.8. Appendix A: Approximation of the time-averaged bottom stress 84
3.9. Appendix B: Separation of shoreward and seaward propagating waves 85
4. Wave setup over a fringing reef with large bottom roughness 87
4.1. Abstract 87
4.2. Introduction 87
4.3. Methods 91
4.3.1. Experimental setup 91
4.3.2. Calculation of radiation stresses 93
4.3.3. Evaluation of velocities 95
4.3.4. Evaluation of the mean momentum equation 97
4.3.5. Uncertainty estimates 97
4.4. Results 98
4.4.1. Wave transformation and setup dynamics 98
4.4.2. Evaluation of the mean bottom stress 100
4.4.3. Predicted wave setup 103
4.4.4. Bottom stress decomposition 104

4.5. Discussion 108
4.6. Conclusions 112

5. General Discussion 115

5.1. Introduction 115
5.2. Model evaluation (chapter 2) 115
5.3. Wave setup dynamics on a smooth reef profile (chapter 3) 117
5.4. Wave setup dynamics on a reef profile with large roughness (chapter 4) 118
5.5. Conclusions 118
5.6. Future work 119

References 121

List of tables

Table 2.1: Open source numerical wave models evaluated in this study. 34
Table 2.2: Summary of the 29 test conditions, tuned values of the key breaking parameter for SWASH, SWAN, and XBeach, and percent error reduction owing to model tuning (*BSS*). Negative values of *BSS* indicate a decrease in the accuracy of the tuned model predictions relative to the untuned model predictions. 56
Table 3.1: Simulated wave and water level conditions including the deep water *rms* wave height ($H_{rms,0}$), the peak period (T_p), the still water depth on the reef flat ($h_{0,r}$), the deep water wave steepness ($H_{rms,0}/L_0$), and the deep water surf similarity parameter (ξ_0). Parameter values are given for both the laboratory scale (1:36 geometric scaling and 1:6 scaling of time) and the equivalent field scale. 63
Table 4.1: Simulated wave and water level conditions, including the deep water *rms* wave height ($H_{rms,0}$), peak period (T_p), still water depth on the reef flat ($h_{0,r}$), deep water wave steepness ($H_{rms,0}/L_0$), and deep water surf similarity parameter (ξ_0). Parameter values are given for both the laboratory scale (i.e., 1:36 geometric scaling and $1:\sqrt{36}$ scaling of time) and the equivalent field scale. 90
Table 4.2: The instantaneous near-bottom velocity (u_b) was composed of a near-bottom current (U_b) and a wave component (u_b') that had both asymmetry (*Au*) and skewness (*Su*) (Figure 4.7B). The full velocity approximation following Eq. (4.12) and (4.13) is presented in row four, as well as velocity estimates neglecting: 1) u_b' and the contribution of the wave roller mass flux (M_r), 2) u_b', and 3) *Au* and *Su*. These velocity approximations are implemented in various classes of models as indicated in the "application" column. Large discrepancies in the predicted velocities (Figure 4.11) result in variation in the bulk bottom drag coefficients (C_d) (Figure 4.12). 104

List of figures

Figure 2.1: Laboratory setup for the University of Michigan flume experiment (Demirbilek et al., 2007). 38

Figure 2.2: (A) Normalized wave energy spectrum (normalized by maximum spectral density at each location) and (B) *rms* wave heights for sea-swell ($H_{rms,SS}$) and infragravity ($H_{rms,IG}$) waves across (C) the reef profile for Test no. 35 ($H_{rms,SS}$ = 0.032 m; T_p = 1.42 s; $h_{0,r}$ = 0.00 m). 42

Figure 2.3: Measured and predicted $H_{rms,SS}$, $H_{rms,IG}$, and $\overline{\eta}$ across the fringing reef profile for Test no. 35 ($H_{rms,SS}$ = 0.032 m; T_p = 1.42 s; $h_{0,r}$ = 0.00 m). Model predictions are shown with untuned (left column) and tuned (right column) breaking parameters. The reef profile is shown on the bottom row. 43

Figure 2.4: Measured and predicted wave energy spectra at Gauge 6 (shoaling region; left column) and Gauge 8 (reef flat; right column) for Test no. 35 ($H_{rms,SS}$ = 0.032 m; T_p = 1.42 s; $h_{0,r}$ = 0.00 m). Model predictions with untuned (upper row) and tuned (lower row) breaking parameters are shown for SWASH (blue line), SWAN (red line), and Xbeach (green line). The peak forcing frequency (vertical solid black line) and the *SS-IG* frequency cut-off (vertical dashed black line) are shown for reference. XBeach simulates *SS* waves using a single representative frequency, so it is only possible to compare the low-frequency spectra for XBeach. 45

Figure 2.5: Comparison of the untuned model predictions with the observations of: $H_{rms,SS}$ (first row), $H_{rms,IG}$ (second row), and $\overline{\eta}$ (third row). Measured values are given on the *x*-axis and simulation results are given on the *y*-axis for SWASH (first column), SWAN (second column), and XBeach (third column). The 1:1 line (solid black diagonal lines) and 50% error bounds (dashed black lines) are given for reference. Point colors correspond to gauge locations as given in the legend. Stars are used to highlight Test no. 35 46

Figure 2.6: Comparison of the tuned model predictions with the observations of: $H_{rms,SS}$ (first row), $H_{rms,IG}$ (second row), and $\overline{\eta}$ (third row). Measured values are given on the *x*-axis and simulation results are given on the *y*-axis for SWASH (first column), SWAN (second column), and XBeach (third column). The 1:1 line (solid black diagonal lines) and 50% error bounds (dashed black lines) are given for reference. Point colors correspond to gauge locations as given in the legend. Stars are used to highlight Test no. 35 47

Figure 2.7: Comparison of untuned (*x*-axis) and tuned (*y*-axis) *WRPE SS*, *WRPE IG*, and *WRPE* $\bar{\eta}$ for the 29 test conditions for SWASH, SWAN, and XBeach. The 1:1 line is shown as the solid black line. Points above the 1:1 line are test conditions were the tuned model was less accurate than the untuned model; points below the 1:1 line are test conditions were the tuned model was more accurate than the untuned model. Stars are used to highlight Test no. 35. Note the scale change for *WRPE* $\bar{\eta}$ 48

Figure 2.8: Observed $H_{rms,SS} / (h_0 + \bar{\eta})$ and dissipation (as expressed by $F_{SS,8}/F_{SS,0}$ where $F_{SS,8}$ and $F_{SS,0}$ are *SS* wave energy flux on the reef flat (Gauge 8) and deep water respectively) versus the non-linearity parameter (F_{c0}) (see Section 2.6.3 for a definition and discussion of F_{c0}). Stars are used to highlight Test no. 35. 49

Figure 2.9: Tuned α values for SWASH (top row) and tuned γ values for SWAN (bottom row; red triangles) and XBeach (bottom row; green triangles) versus S_0, $H_{rms0,SS}$, and $H_{rms0,SS} / (h_{0,r} + \bar{\eta})$. The Battjes and Stive (1985) (BS) and the Nairn (1990) (NA) S_0 dependent γ formulations are shown in (A). The Apotsos et al. (2008) $H_{rms0,SS}$ dependent γ formulation for BJ78 (SWAN) is shown in (B) for laboratory scale and field scale (1:64 geometric scaling). 50

Figure 2.10: Error in $H_{rms,SS}$ predictions (*WRPE SS* shown with color bands) for SWASH as a function of F_{c0} and α. Individual color bands give *WRPE SS* for a given test condition and α. Yellow dots give the optimum α for each test condition. The yellow star is the optimum α for Test no. 35 ($H_{rms,SS}$ = 0.032 m; T_p = 1.42 s; $h_{0,r}$ = 0.00 m). 51

Figure 2.11: Error in $H_{rms,SS}$ predictions (*WRPE SS* shown with color bands) for (A) SWAN and (B) Xbeach as a function of F_{c0} (*x*-axis) and γ (*y*-axis). Individual color bands give *WRPE SS* for a given test condition and γ. Yellow dots give the optimum γ for each test condition. The yellow star is the optimum γ for Test no. 35 ($H_{rms,SS}$ = 0.032 m; T_p = 1.42 s; $h_{0,r}$ = 0.00 m). 53

Figure 3.1: (A) Schematic of the fringing reef showing the reef slope (1:5), reef flat length (14 m; ~500 m field scale), beach slope (1:12), and instrument locations. "Directional" measurement sites have co-located water level and velocity measurements, whereas other "non-directional" sites have only water level measurements. Many of the subsequent figures will focus on the area in the vicinity of the reef crest (black box) where radiation stress gradients and pressure gradients were the largest. (B) An example of the wave setup profile ($\bar{\eta}$) in the vicinity of the reef crest for Run 4, defining the still water depth (h_0) and the total water depth ($h_0 + \bar{\eta}$)...64

Figure 3.2: (A) The bathymetric profile (h_0), (B) the shoreward propagating component of *rms* wave height, and (C) the seaward propagating component of *rms* wave height are shown for Run 4. In each subplot the total (*SS*+*IG*), sea-swell (*SS*), and infragravity (*IG*) components are shown. In (B) and (C), closed circles are direct estimates of the shoreward and seaward components (i.e., locations with water level and velocity data), while open circles rely on interpolation of the seaward component as described in Section 3.4.2.....68

Figure 3.3: (B-I) Wave plunging sequence taken during Run 4 in the immediate vicinity of the reef crest (solid box in subplot A). In subplots B-J the notation t_0 denotes the start of the breaking sequence with a frame rate of ~25 Hz. The area of the photos is where the most intense wave breaking occurred and only covers a small portion of the total reef slope and reef flat shown in (A). (J) Larger area (subplot A dashed box) showing the development of a steady bore at x = 0.8 m propagating shoreward on the reef flat. (K) Oblique photograph showing a bore on the reef flat and a wave steepening on the reef slope. 69

Figure 3.4: (A) The bathymetric profile (h_0)and (B) the shoreward propagating components of the wave energy flux (F^+) are shown in the vicinity of the reef crest for Run 4 (black box in Figure 3.1A). Subscripts *SS* and *IG* denote sea-swell and infagravity, respectively. (C) The radiation stresses S_{xx} and R_{xx} are the contribution from linear wave theory Eq.(3.12) and the wave roller Eq. (3.6), respectively. The “effective” radiation stress ($S_{xx,eff}$) is the radiation stress needed to close the mean momentum equation via Eq. (3.14). (D) Radiation stresses S_{xx} (“No roller”) and S_{xx}+R_{xx} (“Roller”) were used to evaluate $\overline{\eta}_{pred}$ via Eq. (3.13) and compared with observations “Obs”. Vertical error bars are given for $S_{xx,eff}$ and $\overline{\eta}_{pred}$ (see Section 3.4.3). Vertical black lines give:(B) the start of wave dissipation and hence wave roller growth, (C) maximum S_{xx}, and (D) the region of maximum setdown. 71

Figure 3.5: (A,C) Radiation stresses S_{xx} (“No roller”) and S_{xx}+R_{xx} (“Roller”) were used to evaluate (B,D) $\overline{\eta}_{pred}$ via Eq. (3.13) and compared with observations “Obs” in the vicinity of the reef crest for Run 13 (first column) and Run 16 (second column). Vertical error bars are given for $S_{xx,eff}$ and $\overline{\eta}_{pred}$ (see Section 3.4.3). 72

Figure 3.6: Variation of $\overline{\eta}_r$ with -ΔS_{xx} calculated from offshore to x = 4 m. Symbols denote runs with shared conditions and a single variable changed. A quadratic, least-

squares trend line is given of Runs 1-6. Numbers adjacent to symbols denote the run number (refer to Table 3.1). 72

Figure 3.7: Variation of the cross-shore integrated (x = -2 to 4 m) pressure gradient with the cross-shore integrated radiation stress gradient ($-\Delta S_{xx}$; Eq. (3.15)) for the sixteen wave and water level conditions. As the cross-shore integration spans the entire surf zone, this analysis is independent of the wave roller (i.e., $-\Delta(S_{xx}+R_{xx})= -\Delta S_{xx}$). The mean momentum equation Eq. (3.2) predicts a 1:1 relationship (black line) should exist. Vertical and horizontal (typically not visible) error bars show the uncertainties due to instrument accuracy (see Section 3.4.3). 74

Figure 3.8: Variation of the pressure and radiation stress gradients cross-shore integrated from offshore (x = -2 m) to maximum setdown (first row; A,B) and from maximum setdown to shoreward of the surf zone (x = 4 m) (second row; C,D). The radiation stress gradients were evaluated without ($-\Delta S_{xx}$) (first column) and with ($-\Delta(S_{xx} + R_{xx})$) (second column) the wave roller. The mean momentum equation Eq. (3.2) predicts a 1:1 relationship (black lines) should exist for any integration region. Note the ~2x change in the axis scale between subplots A,B and subplots C,D. Vertical and horizontal (typically not visible) error bars show the uncertainties due to instrument accuracy (see Section 3.4.3)..... 75

Figure 3.9: Comparison of predicted wave setdown (A) and setup (B) with observations. Predictions are evaluated from Eq. (3.13) without (i.e., S_{xx}) and with (i.e., $S_{xx} + R_{xx}$) the wave roller contribution to S_{xx}. Run 8 (discussed in the text) is highlighted by the cyan circles. Vertical and horizontal (generally not visible) error bars show the uncertainties due to instrument accuracy (see Section 3.4.3). Note the scale change between (A) and (B), which renders error bars in (B) less visible. 76

Figure 3.10: Relative *rms* error ϵ_{rms} (Eq. (3.16)) in the predicted setdown/ setup profiles ($\overline{\eta}_{pred}$) calculated from Eq. (3.13) with the wave roller contribution to radiation stress (R_{xx}) evaluated via Eq. (3.6) - (3.8) using various values of the roller slope coefficient (β_D). Magenta dots give the lowest ϵ_{rms} for each run, and the horizontal cyan dashed line gives the mean optimum β_D = 0.19 ($\theta_r = 11^o$) for the array of runs. For comparison, ϵ_{rms} without the wave roller is shown below the main plot. 77

Figure 3.11: (A) Estimated wave front inclination angle (θ_w; Eq. (3.17)) across (B) the reef profile from well offshore of the break point to near the shoreline. Vertical black lines give the averaging area used to calculate the θ_w values shown in Figure 3.12. 78

Figure 3.12: Variation of the optimum wave roller inclination angle (θ_r; the equivalent wave roller dissipation coefficient β_D is given on the secondary y-axis) with the measured wave front inclination angle (θ_w; Eq. (3.17)) spatially-averaged over the surf zone region indicated by the vertical black lines in Figure 3.11.....79

Figure 4.1: (A) Schematic of the fringing reef showing the reef slope (1:5), reef flat length (14 m; ~500 m field scale), beach slope (1:12), and instrument locations. Sections of the bathymetry (reef slope and reef flat) highlighted in dashed yellow were affixed with roughness elements as shown in Figure 4.2. (B) An example of the wave setup profile ($\overline{\eta}$) in the vicinity of the reef crest for Run 4, defining the still water depth (h_0) and the total water depth (h). 91

Figure 4.2: (A) View of the dry flume with roughness elements looking shoreward from offshore of the reef slope. (B) Roughness elements used were (D) 1.8 cm concrete cubes affixed in the repeating staggered pattern shown in (C). This pattern gave N = 400 m^{-2} cubes per unit plan area, with 7,000 cubes in total covering the reef slope and flat. 93

Figure 4.3: (A) Wave height (H_{rms}) and (B) wave setup ($\overline{\eta}$) across (C) the fringing reef profile for Run 4 both including ("rough") and without ("smooth") roughness. Vertical error bars show the uncertainties due to instrument accuracy and are negligible here (see Section 4.3.5). 98

Figure 4.4: (A) Comparison of the *rms* wave heights (H_{rms}) and (B) wave height-to-water depth ratios (H_{rms}/h) on the reef flat for runs including ("rough") and without ("smooth") roughness. 99

Figure 4.5: (A) Comparison of maximum setdown, (B) setup on the reef flat ($\overline{\eta}_r$), and (C) setup generation ($\Delta\overline{\eta}$) for runs including ("rough") and without ("smooth") roughness. Solid red lines give the linear least squares trend lines ("fit") and dashed red curves give the upper and lower bounds of the 95% confidence interval ("CI") for the trend line. Vertical and horizontal error bars show the uncertainties due to instrument accuracy (see Section 4.3.5). Note the scale change between (A) and (B) and (C), which renders error bars in (B) and (C) less visible. 100

Figure 4.6: Comparison of the cross-shore integrated radiation stress ($-\Delta\left(S_{xx}+R_{xx}\right)$) and pressure gradient terms for runs including ("rough") and without ("smooth") roughness. Vertical and horizontal (generally not visible) error bars show the uncertainties due to instrument accuracy (see Section 4.3.5). 101

Figure 4.7: Comparisons of the observed ("obs") and predicted ("pred") time-averaged (A) *rms* wave velocities (u_b') and (B) mean velocities (U_b). Data are shown for both smooth runs (open circles) and with roughness (open squares). Dashed lines give the linear least squares trend lines while the solid line indicates 1:1. 101

Figure 4.8: (A) Ursell number (a measure of wave nonlinearity; Doering and Bowen 1995) and (B) velocity skewness (*Su*) and asymmetry (*Au*) are shown over (C) the bathymetric profile for runs including roughness. In (B) small filled squares and connecting lines are *Su* and *Au* approximated from water level time-series and large open squares are values calculated from the velocity time-series. 102

Figure 4.9: Comparison of the cross-shore integrated time-averaged velocity term with the sum of the cross-shore integrated pressure and radiation stress gradient terms for runs including roughness. Per Eq. (4.16), the linear least squares trend line ("fit"; solid red lines) gives the estimated bulk bottom drag coefficient (C_d = 0.028) cross-shore averaged and averaged across all runs with roughness. The dashed red curves show the upper and lower bounds of the 95% confidence interval ("CI") for the trend line. Vertical error bars show the uncertainties due to instrument accuracy (see Section 4.3.5). 103

Figure 4.10: (A) Shoreward wave energy flux from sea-swell (F_{SS}^{+}) and infragravity (F_{IG}^{+}) waves, (B) radiation stresses (S_{xx} + R_{xx}), and (C) mean bottom stresses ($\overline{\tau}_b$) across (E) the fringing reef profile for Run 4 including ("rough") and without ("smooth") roughness. (D) Radiation stress gradients and mean bottom stresses were used to predicted ("pred") setup ($\overline{\eta}$) via Eq. (4.15) and compared with observations ("obs"). For the smooth run, $\overline{\eta}$ was well predicted without $\overline{\tau}_b$ (i.e., C_d = 0). However, for the rough run $\overline{\eta}$ was underpredicted without $\overline{\tau}_b$ (i.e., C_d = 0) but was well predicted with the estimated $\overline{\tau}_b$ (C_d = 0.028). 105

Figure 4.11: Comparison of observed ("obs") and predicted ("pred") wave setup on the reef flat ($\overline{\eta}_r$) for runs with roughness. Wave setup is predicted from observation of radiation stress gradients via Eq. (4.15) neglecting (red circles; C_d = 0) and including (black squares; C_d = 0.028) the predicted mean bottom stress. 106

Figure 4.12: Comparisons of the observed ("obs") and predicted ("pred") velocity term $\overline{|u_b|u_b}$ relevant to the calculation of mean bottom stress per Eq. (4.2), for instrument sites with velocity data on the reef flat. Data are shown for both smooth runs (open circles) and with roughness (open squares). Dashed linear least squares trend lines are

shown for each method of predicting velocity (Table 4.2). The estimated velocity used in this study (shown in black) includes a near-bottom current (U_b) and a wave component (u_b') with velocity asymmetry (A_u) and skewness (S_u). 107

Figure 4.13: The velocity approximations given in Table 4.2 and Figure 4.11 were used to compute the cross-shore integrated time-averaged velocity term in Eq. (4.16) (x-axis) and compared with the sum of the cross-shore integrated pressure and radiation stress gradients (y-axis) for runs with roughness. Per Eq. (4.16), the linear least squares trend lines (dashed lines) give the estimated bulk bottom drag coefficients (C_d) for each velocity approximation (values given in legend). The estimated velocity used in this study (shown in black) includes a near-bottom current (U_b) and a wave component (u_b') with velocity asymmetry (A_u) and skewness (S_u)..... 108

Publications arising from this thesis

This thesis is presented as a series of papers in accordance with standards set by The University of Western Australia. Chapters that have been published or submitted to be published in peer reviewed journals are listed below, as well as my contribution to the publication and the contributions of my co-authors.

Buckley, M., R. Lowe, and J. Hansen, 2014: Evaluation of nearshore wave models in steep reef environments. *Ocean Dyn.*, **64,** 847-862. (Chapter 2)

This work is primarily my own, including numerical modeling, data analysis, and writing. Co-authors Ryan Lowe and Jeff Hansen provided advice on data interpretation and significant editorial feedback on the manuscript.

Buckley, M., R. Lowe, J. Hansen, and A. Van Dongeren, 2015a: Dynamics of wave setup over a steeply-sloping fringing reef. *J. Phys. Oceanogr.*, **45**. (Chapter 3)

This work is primarily my own, including experimental design, data analysis, and writing. Co-authors Ryan Lowe, Jeff Hansen, and Ap Van Dongeren provided significant advice on data interpretation and editorial feedback on the manuscript.

Buckley, M., R. Lowe, J. Hansen, and A. Van Dongeren, 2015b: Wave setup over a fringing reef with large bottom roughness. *J. Phys. Oceanogr.*, **In review**. (Chapter 4)

This work is primarily my own, including experimental design, data analysis, and writing. Co-authors Ryan Lowe, Jeff Hansen, and Ap Van Dongeren provided significant advice on data interpretation and editorial feedback on the manuscript.

Acknowledgements

First, I would like to thank my primary supervisors Ryan Lowe and Jeff Hansen for their guidance, support, and patience during my whole PhD candidature. I would also like to thank my external supervisors Ap Van Dongeren and Dano Roelvink for their assistance during laboratory experiments and their continued guidance. I thank the laboratory technicians at Deltares for their assistance and expertise. I thank Prof Tom Baldock, Prof Johanna Rosman, and Prof Janet Becker for their helpful feedback.

I would like to personally thank my parents Betty and Larry Buckley for their support and encouragement throughout the years.

This project forms part of a PhD study by M. Buckley at The University of Western Australia and is supported by an International Postgraduate Research Scholarship. The experiments were funded by an ARC Future Fellowship grant (FT110100201) and ARC Discovery Project grant (DP140102026) to R.J.L. as well as a UWA Research Collaboration Award to R.J.L., M.L.B., and AVD. M.L.B. and R.J.L. also acknowledges support through the ARC Centre of Excellence for Coral Reef Studies (CE140100020).

Notation

Symbol	Definition	Unit
Au, Su	Velocity asymmetry A_u and velocity skewness S_u	-
α	Wave breaking criteria within SWASH	-
B	Parametric wave breaking intensity coefficient	-
BSS	Brier Skill Score	-
β	Reef slope	-
β_D	Wave roller dissipation coefficient	-
C_d	Bulk bottom drag coefficient	-
$C_{\eta\eta}, C^+_{\eta\eta}, C^-_{\eta\eta}$	Wave power spectral density for the total, shoreward, and seaward components, respectively	$m^2\,Hz^{-1}$
c	Wave celerity	$m\,s^{-1}$
c_g	Wave group velocity	$m\,s^{-1}$
D_{bore}	Wave energy dissipation rate of a bore	$J\,m^{-2}\,s^{-1}$
D_{br}	Wave energy dissipation rate due to breaking	$J\,m^{-2}\,s^{-1}$
D_{fric}	Wave energy dissipation rate due to roughness	$J\,m^{-2}\,s^{-1}$
E	Wave energy density	$J\,m^{-2}$
E_r	Kinetic energy of the wave roller	$J\,m^{-2}$
ξ_0	Deep water surf similarity parameter	-
η	Free surface deviation from h_0	m
$\overline{\eta}'$	Variation of η on the wave group time-scale	m
$\overline{\eta}$	Time-averaged η (e.g., wave setup or setdown)	m
$\overline{\eta}_{pred}$	Predicted $\overline{\eta}$	m
$\overline{\eta}_r$	Time-averaged η on the reef flat	m
$\Delta\overline{\eta}$	Difference between maximum setdown and $\overline{\eta}_r$	m
F, F^+, F^-	Wave energy flux for the total, shoreward, and seaward components, respectively	$J\,m^{-1}\,s^{-1}$
F_{c0}	Nonlinearity parameter	-
f	Frequency	Hz
f_p	Peak wave frequency	Hz
f_{rep}	Representative wave frequency	Hz
f_l	Boundary between *SS* and *IG* frequency bands	Hz
$f_{SS,mean}$, $f_{IG,mean}$	Mean frequency of the sea-swell and infragravity waves, respectively	Hz
f_w	Wave bottom drag coefficient	-
g	Acceleration due to gravity	$m\,s^{-2}$
γ	Parametric maximum wave height to water depth ratio	-
k	Wave number	$radians\,m^{-1}$
H_{rms}	Root mean squared (*rms*) wave height	m
$H_{rms,0}$	Deep water root mean squared (*rms*) wave height	m
h_0	Still water depth	m
$h_{0,r}$	Still water depth on the reef flat	m
KE, PE	Wave kinetic and potential energy, respectively	$J\,m^{-2}$
L_0	Deep water wave length	m
λ_f	Frontal area of roughness elements per unit plan area	-
λ_p	Plane area of roughness elements per unit plan area	-

l_h, l_v	Horizontal (l_h) and vertical (l_v) dimensions of roughness elements	m
M_T	Depth- and time- averaged Lagrangian mass flux	kg m^{-1} s^{-1}
M_w	Wave mass flux	kg m^{-1} s^{-1}
M_r	Wave roller mass flux	kg m^{-1} s^{-1}
N	Number of roughness elements per unit plan area	m^{-2}
θ_d	Wave propagation direction in SWAN	^{o}
θ_η	Instantaneous free surface inclination angle	^{o}
θ_r	Wave roller inclination angle	^{o}
θ_w	Wave front inclination angle	^{o}
P	Pressure	N m^{-2}
P_h, P_{nh}	Hydrostatic and non-hydrostatic pressure, respectively within SWASH	N m^{-2}
Ψ	Periodic forcing function	-
Q_{br}	Fraction of breaking waves within parametric wave model	-
ρ	Density of water	kg m^{-3}
SS, IG	Sea-swell and infragravity frequency bands, respectively	Hz
S_0	Offshore wave steepness	-
S_{tot}	Wave energy source/ sink within SWAN	J m^{-2} s^{-1}
S_{xx}	Cross-shore component of the radiation stress tensor	N m^{-1}
$S_{xx,eff}$	Cross-shore component of the effective radiation stress	N m^{-1}
R_{xx}	Cross-shore component of the wave roller radiation stress	N m^{-1}
$\Delta\left(S_{xx}+R_{xx}\right)$	Cross-shore integrated radiation stress gradient	N m^{-1}
σ_f	Wave frequency band in SWAN	Hz
σ_u	Standard deviation of u_b'	m s^{-1}
T_p	Peak wave period	s
τ	Stress tensor with in SWASH	N m^{-2}
$\overline{\tau}_b$	Time-averaged (mean) bottom stress	N m^{-2}
$\overline{\tau}_t$	Time-averaged shear stress at the boundary of the wave and the wave roller	N m^{-2}
U_b	Cross-shore time-averaged near-bottom velocity	m s^{-1}
u, w	Velocity in the cross-shore and vertical directions, respectively	m s^{-1}
u', w'	Wave orbital velocities in the cross-shore and vertical directions, respectively	m s^{-1}
u_b	Cross-shore instantaneous near-bottom velocity	m s^{-1}
u_b'	Cross-shore instantaneous near-bottom wave velocity	m s^{-1}
WRPE	Weighted *rms* percent error metric	%
ω	Wave angular frequency	radians s^{-1}

1. General Introduction

1.1. Introduction

Fringing coral reefs are common features for a large portion of the world's tropical coastlines, providing a natural buffer between the land and the sea. Reefs also provide a multitude of eco-system services (Moberg and Folke 1999; Barbier et al. 2011). However, coral reefs are in decline worldwide due to a combination of local and global stressors, including overfishing, climate change-induced coral bleaching, eutrophication, and disease (Hughes et al. 2003). Unlike sandy beaches, much of the bathymetry of reefs is owing to live organisms, which create the calcium carbonate skeletons that establish the morphologies and bottom roughness characteristics that define reefs (Alvarez-Filip et al. 2009). The growth pattern of hard corals and the long-term response to sea-level variations create the unique structure of fringing reefs, which are typically characterised by steep reef slopes and long shallow reef flats (Monismith 2007; Lowe and Falter 2015).

Surf zone wave and wave setup dynamics are paramount to understanding a number of other physical (e.g., coastal inundation and sediment transport) and biological processes in the coastal ocean (e.g., larval and nutrient transport and dispersal) (Roberts et al. 1975; Monismith 2007; Lowe et al. 2010; Lowe and Falter 2015). This is particularly true for coral reefs, as the reef building organisms require water motion for nutrient and gas exchange as well as reproduction through larval dispersal (Monismith 2007). Despite surf zone processes being analogous between reefs and sandy beaches, the high slopes and roughness of reefs often exceed the theoretical limits of validity and the validation range for existing surf zone models, which have historically been developed and validated for use in sandy beach environments. As such, there is a need to quantifiably investigate existing theory and potentially develop new theory for application to reef environments.

1.2. Background

When ocean waves approach a shoreline the height of the waves increase, their wavelength contracts (via shoaling), and the waves steepen until their form becomes unstable and collapse in the form of a breaking wave (Hamm et al. 1993). The form of the breaking wave and the associated rate of energy loss are dependent on the offshore wave steepness and the bottom slope (Iribarren and Nogales 1949). In the breaking process, ordered wave energy is transferred to turbulent energy as well as higher and

lower frequencies (Elgar et al. 1992). Decay of wave energy shoreward of the break point and the associated momentum flux gradients (Longuet-Higgins and Stewart 1962) are usually well-balanced by an increase in the mean water level shoreward of the break point (wave setup; Longuet-Higgins and Stewart 1964; Bowen et al. 1968; Guza and Thornton 1981; Gourlay 1994).

Wave and setup dynamics are governed by physical laws and have been studied in great detail for the last few decades in areas of mild sandy slopes primarily in Europe, the United States, and areas of Australia (Birkemeier and Thornton 1994; Raubenheimer et al. 1996; Elgar et al. 2001; Raubenheimer et al. 2001; Ruessink et al. 2001; Raubenheimer 2002; Thomson et al. 2006). Analogous processes take place on the estimated 80% of coastlines fronted by steep rocky or coral reef slopes (Emery and Kuhn 1982), but have been much less studied (Massel and Gourlay 2000; Sheremet et al. 2011). Though the relevant processes are believed to be the same, due to the complex morphologies and extreme slopes of reef systems, the relative importance of these processes and their highly nonlinear interactions differ from beach environments (Massel and Gourlay 2000; Sheremet et al. 2011). The underlying assumptions used to investigate and predict dynamics in sandy mild-slope environments are often technically violated when applied to steep rocky or coral reef environments (Massel and Gourlay 2000; Demirbilek and Nwogu 2007; Sheremet et al. 2011). For example, the steep slopes may violate the mild-slope assumption found in many weakly dispersive models (Demirbilek and Nwogu 2007). Additionally on steep slopes, parameterizations of bed stress, wave breaking, and other processes developed for mild slopes and found in many models, may not be applicable.

In comparison to sandy beaches, wave and setup observations on reefs are severely lacking. In part due to the difficulties in obtaining measurements within the surf zone of reefs, there is an absence of field observations between water depths of five meters and reef crests where rapid wave transformation and setup generation occur (Péquignet et al. 2009; Vetter et al. 2010; Pomeroy et al. 2012; Becker et al. 2014). The only available surf zone observations on reef profiles have come from laboratory flume experiments, including those by Gerritsen (1980), Seelig (1983), Nelson and Lesleighter (1985), Gourlay (1994, 1996b), Demirbilek et al. (2007), and Yao et al. (2012b). These laboratory studies have led to some understanding of how setup responds to offshore wave height, wave period, and still water depth. Laboratory data have also been the basis for empirical formulas for predicting setup on fringing reefs, including the formulas of Gourlay (1996a) that have been commonly applied (e.g., Sheppard et al.

2005). However, these laboratory studies targeted bulk wave dissipation and setup trends and do not provide the spatial-resolution of surf zone measurements required to evaluate the details of wave and setup dynamics. In addition, prior to this thesis there has not been a rigorous experimental investigation of the effect the large roughness that is a characteristic of reefs has on wave and setup dynamics.

1.3. Motivation and Aims

This thesis contributes to the understanding and prediction of the complex wave and setup dynamics on steep slopes and in areas of large bottom roughness by:

1. Evaluating how three of the most common classes of existing nearshore models perform in predicting both the wave transformation and setup dynamics across a steep fringing reef (chapter two)
2. Investigating the detailed surf zone momentum balances that control setup dynamics on a steep-slope profile, including how models can be modified to improve these predictions (chapter three)
3. Quantifying and predicting the effect that large roughness has on wave and setup dynamics (chapter four)

1.4. Thesis Structure

This thesis comprises a general introduction (chapter one) followed by three chapters presented in manuscript format (chapters two, three, and four) and a general discussion (chapter five). In chapter two, commonly used nearshore numerical models are reviewed and compared with observations from Demirbilek et al. (2007). Model evaluation in chapter two focuses on bulk wave and setup statistics on a smooth reef, as datasets including roughness, measurements of velocity and wave direction, and detailed surf zone measurements were not available. This lack of data was addressed by conducting the new high-resolution laboratory experiment detailed in chapters three and four. In both chapters three and four, we utilize the new dataset to evaluate the time-averaged cross-shore momentum equation from observations of waves and wave setup, rather than the traditional approach of using empirical or idealized models to predict wave transformation through the surf zone. Finally, chapter five, integrates the findings from the previous chapters and discusses the broader implications of this work.

2. Evaluation of nearshore wave models in steep reef environments

2.1. Abstract

To provide coastal engineers and scientists with a quantitative evaluation of nearshore numerical wave models in reef environments, we review and compare three commonly used models with detailed laboratory observations. These models are: 1) SWASH (Zijlema et al. 2011) a phase-resolving nonlinear shallow water wave model with added non-hydrostatic terms; 2) SWAN (Booij et al. 1999) a phase-averaged spectral wave model; and 3) XBeach (Roelvink et al. 2009) a coupled phase-averaged spectral wave model (applied to modeling sea-swell waves) and nonlinear shallow water model (applied to modeling infragravity waves). A quantitative assessment was made of each model's ability to predict sea-swell (*SS*) wave height, infragravity (*IG*) wave height, wave spectra, and wave setup ($\bar{\eta}$) at 5 locations across the laboratory fringing reef profile of Demirbilek et al. (2007). Simulations were performed with the "recommended" empirical coefficients as documented for each model, and then the key wave breaking parameter for each model (α in SWASH and γ in both SWAN and XBeach) was optimized to most accurately reproduce the observations. SWASH, SWAN, and XBeach were found to be capable of predicting *SS* wave height variations across the steep fringing reef profile with reasonable accuracy using the default coefficients. Nevertheless, tuning of the key wave breaking parameter improved the accuracy of each model's predictions. SWASH and XBeach were also able to predict *IG* wave height and spectral transformation. Although SWAN was capable of modeling the *SS* wave height, in its current form it was not capable of modeling the observed spectral transformation into lower frequencies, as evident in the under prediction of the low-frequency waves.

2.2. Introduction

Historically nearly all nearshore wave models have primarily (or exclusively) been developed, calibrated, and tested on mild-slope sandy beaches. As a result, it is unclear if these models are suitable to simulate waves in reef systems that often have steep, sometimes nearly vertical, slopes and complex morphology. Here we review three commonly used numerical nearshore wave models and quantitatively compare the model predictions with data from a detailed laboratory experiment of wave transformation across a model fringing reef. This evaluation provides insight into the suitability of each model to simulate a full range of hydrodynamic processes (sea-swell,

infragravity waves, and wave setup) within reef systems, as well as an assessment of where each model tends to break down and thus could be further improved.

Numerical wave models used to investigate field scale processes on the order kilometres to 10s of kilometers loosely fall into two categories: phase-averaged and phase-resolving (Cavaleri et al. 2007). Phase-averaged models simulate wave processes in a stochastic manner, often based on linear wave theory with empirical formulations derived from field or laboratory data. Phase-resolving models simulate wave processes based on conservation laws (mass and momentum), but may also include empirical formulations calibrated to field or laboratory data. Phase-resolving models resolve individual waveforms, requiring a grid resolution fine enough to capture the shortest wave length (highest frequency waves) of interest in a study. This further increases the computational demand of such simulations, as the maximum allowable computational time step (dictated by the Courant condition) required to resolve wave propagation is dependent on the horizontal grid resolution and depth. Due to this computational demand, the application of phase-resolving wave models has been largely restricted to studies of lower frequency motions (e.g., infragravity waves, tsunamis, and tides), small scale (e.g., a harbor entrance) and/or short duration dynamics, or idealised one-dimensional (1D) studies. Phase-averaged models, on the other hand, do not have the same restriction on grid resolution or time steps, allowing much larger scale and longer duration studies to be conducted. For larger scale and/or longer duration studies which require modelling physical processes at a range of time scales (e.g., wind-waves, tides, and currents) both phase-resolving and phase-averaged models are often coupled.

The underlying assumptions embedded in existing nearshore wave models, e.g., spectral models and Boussinesq-type, that were originally developed for mild-slope beach environments are often technically violated when applied to reef environments (Massel and Gourlay 2000; Demirbilek and Nwogu 2007; Sheremet et al. 2011). For example, the steep slopes of coral reefs may violate the mild-slope assumption found in many weakly dispersive models (Demirbilek and Nwogu 2007). Additionally, parameterizations of bed stress, wave breaking, and other processes developed originally for sandy beach environments may not be applicable. Due to the rapid bathymetric changes on reef slopes, wave breaking is particularly intense and occurs across a much narrower region than the broad surf zone typically found on dissipative beaches. Further, due to the increased roughness, rates of bottom friction dissipation have also been shown to be much greater than on sandy beaches (e.g., Lowe et al. 2005b).

Despite these theoretical limitations, models and parameterizations originally derived for mild sandy slopes have often been applied to steep slope reef environments with little or no modification. Symonds et al. (1995) first formulated a one-dimensional (1D) analytical model for wave-driven currents on reefs, based on a linearized set of momentum equations and radiation stress theory. Subsequent 1D analytical models have been formulated by Hearn (1999) and Gourlay and Colleter (2005). Sheremet et al. (2011) compared a 1D nonlinear phase-averaged model and a 1D phase-resolving numerical model to laboratory data. Demirbilek and Nwogu (2007) and others have applied 1D Boussinesq-type models to laboratory data. Zijlema (2012) and Torres-Freyermuth et al. (2012) applied a non-hydrostatic nonlinear shallow water wave model to laboratory and field datasets. Phase-averaged spectral wave models have been applied in field studies by Lowe et al. (2009b), Hoeke et al. (2011), and Storlazzi et al. (2011), and tested against both laboratory and field data by Filipot and Cheung (2012). Pomeroy et al. (2012) and Van Dongeren et al. (2013) applied a coupled wave action and nonlinear shallow water model to investigate the field-scale dynamics of short- and long-period wave motions across a fringing reef.

In this present study, three widely used open-source nearshore wave models are reviewed, and their performance is quantitatively compared against a comprehensive laboratory data set of wave transformation across a steep fringing reef profile under a range of different conditions. A particular focus of the assessment is on the dynamics of wave breaking in the surf zone region, and how this also influences predictions of low-frequency wave motions and wave setup. Each model was applied to 29 laboratory test conditions of Demirbilek and Nwogu (2007), which incorporated a wide range of incident spectral wave conditions and still water levels. Models were assessed for their performance in predicting sea-swell (*SS*) wave heights, infragravity (*IG*) wave heights, wave spectra, and wave setup ($\overline{\eta}$, the mean deviation from still water) at 5 locations across the fringing reef profile.

2.3. Numerical wave models

We selected three common nearshore wave models (Table 2.1). They are open-source, widely used, and span a range of modeling approaches (both phase-averaged and phase-resolving), theoretical complexities, and computational expense. These include: 1) SWASH (Simulating WAves till Shore; Version 1.20 downloaded from http://swash.sourceforge.net) (Zijlema et al. 2011), a phase-resolving non-hydrostatic free surface model; 2) SWAN (Simulating Waves Nearshore; Version 40.91 downloaded

from http://swanmodel.sourceforge.net) (Booij et al. 1999), a phase-averaged spectral wave model; and 3) XBeach (Version 19; downloaded from http://oss.deltares.nl/web/xbeach) (Roelvink et al. 2009), a nearshore wave and circulation model that combines phase-averaged and phase-resolving approaches. As detailed descriptions of these three models are already widely available in the literature, only a brief overview of each is included here.

Table 2.1: Open source numerical wave models evaluated in this study.

Model	Class	Wave breaking formulation	Reference
SWASH	NLSW+ non-hydrostatic terms	Shock-capturing	(Zijlema et al., 2011)
SWAN	Wave action balance	Parametric	(Booij et al., 1999)
XBeach	Wave action balance with phase resolving IG	Parametric	(Roelvink et al., 2009)

SWASH solves the nonlinear shallow-water equations with added non-hydrostatic pressure (Zijlema et al. 2011). Though the model is 3-dimensional for reasons of exposition Smit et al. (2013) describe the governing equations in the 2-dimensional vertical plane with Cartesian, cross-shore (x) and vertical (z) coordinates, and time (t) as:

$$\frac{\partial u}{\partial t}+\frac{\partial uu}{\partial x}+\frac{\partial wu}{\partial z}=-\frac{1}{\rho}\frac{\partial\left(P_h+P_{nh}\right)}{\partial x}+\frac{\partial \tau_{xx}}{\partial x}+\frac{\partial \tau_{xz}}{\partial z}, \tag{2.1}$$

$$\frac{\partial w}{\partial t}+\frac{\partial uw}{\partial x}+\frac{\partial ww}{\partial z}=-\frac{1}{\rho}\frac{\partial P_{nh}}{\partial z}+\frac{\partial \tau_{zz}}{\partial z}+\frac{\partial \tau_{zx}}{\partial x}, \text{ and} \tag{2.2}$$

$$\frac{\partial u}{\partial x}+\frac{\partial w}{\partial z}=0, \tag{2.3}$$

where $u(x,z,t)$ and $w(x,z,t)$ are the horizontal and vertical velocities, respectively; ρ is water density; P_h and P_{nh} are the hydrostatic and non-hydrostatic pressures, respectively, and τ_{xx}, τ_{xz}, τ_{zz}, and τ_{zx} are the turbulent stresses.

SWAN predicts the spectral evolution of wave action in space and time (Booij et al. 1999). Wave action (A) is defined as $A=E(\sigma_f,\theta_d)/\sigma_f$, where $E(\sigma_f,\theta_d)$ is the wave energy spectrum that distributes wave energy over frequencies (σ_f) and propagation directions (θ_d). The governing wave action equation is (Booij et al. 1999):

$$\frac{\partial A}{\partial t}+\frac{\partial c_x A}{\partial x}+\frac{\partial c_y A}{\partial y}+\frac{\partial c_\sigma A}{\partial \sigma_f}+\frac{\partial c_\theta A}{\partial \theta_d}=\frac{S_{tot}}{\sigma_f}, \tag{2.4}$$

where, c_x, c_y, c_σ, and c_θ are the propagation velocities of wave energy in spatial (x, y), frequency (σ_f), and directional (θ_d) space, respectively. The S_{tot} term can include

dissipation terms, in particular due to depth-limited wave breaking and bottom friction, as well as growth and energy transfer terms.

XBeach models *SS* wave processes in a phase-averaged manner, solving the wave action equation similar to Eq. (2.4) (Roelvink et al. 2009). However, the wave action equation in XBeach is solved for a single representative *SS* wave frequency and is applied at the time-scale of individual wave groups. Applying the wave action equation at the time-scale of individual wave groups allows variation in *SS* wave height and total water depth on the time-scale of individual wave groups. Infragravity (*IG*) wave motions and mean flows are instead modelled in a phase-resolving manner, solving the nonlinear shallow-water equations (i.e., Eq. (2.1)-(2.3)) but in a depth-averaged, hydrostatic form) (Roelvink et al. 2009). This allows XBeach to treat *SS* wave processes in a phase-averaged manner and long-wave processes (e.g., *IG* waves and tides) in a phase-resolving manner. This reduces the computational demand compared to a full (all frequencies) phase-resolving model.

2.3.1. Wave breaking

There is no analytical solution for wave breaking. Commonly used depth-integrated numerical wave models do not describe overturning of the free surface and thus cannot fully reproduce wave breaking processes (Cienfuegos et al. 2010). Phase-resolving models of the Boussinesq-type commonly include wave breaking effects by adding an ad-hoc dissipation term, sometimes including roller effects, to the momentum equations (Svendsen 1984a; Schäffer et al. 1993; Madsen et al. 1997). This method was referred to as an eddy viscosity approach. Eddy viscosity formulations require scaling coefficients with no direct physical or measurable meaning (Cienfuegos et al. 2010). The nonlinear shallow-water equations can be formulated to satisfy exact conservation laws (mass and momentum) for non-dispersive waves (Zijlema et al. 2011; Smit et al. 2013). Implementation of exact conservation laws and use of numerical shock-capturing schemes, which solve for discontinuous hydraulic problems, allow wave breaking dissipation to be modeled in a manner similar to hydraulic jumps (Zijlema and Stelling 2008).

SWASH accounts for depth-limited wave breaking with a shock-capturing conservation scheme (Zijlema and Stelling 2008). In SWASH with a large number of vertical layers, as waves steepen and approach breaking, a saw tooth waveform develops. At this discontinuity, the correct amount of energy is dissipated numerically via a shock-capturing scheme (Zijlema et al. 2011). When using only a single vertical layer, the saw tooth waveform is unable to develop due to the lack of vertical resolution

of flow velocity. This requires an additional metric to determine the onset of wave breaking, i.e. (Smit et al. 2013):

$$\frac{\partial \eta}{\partial t} > \alpha \sqrt{g\left(h_0 + \bar{\eta}\right)}, \tag{2.5}$$

where α is an empirical tuning parameter that determines the onset of the breaking process, g is acceleration due to gravity, h_0 is still water depth, and $\bar{\eta}$ is the time-averaged deviation of the free surface (η) from h_0 (also referred to as wave setup). When the condition in Eq. (2.5) is met, non-hydrostatic pressure terms are removed locally allowing for the development of a saw tooth waveform. The default value of $\alpha = 0.6$ corresponds to a local wave front slope of roughly 25^o. This wave breaking dissipation method applies to both sea-swell waves and infragravity waves where wave steepness exceeds the breaking threshold value per Eq. (2.5).

Phase-averaged models use empirical (parametric) formulations to predict the rate of wave energy dissipation during the wave breaking process. These formulations generally include a method for estimating a probability distribution for the fraction of waves that are breaking (Q_{br}) and apply an energy dissipation rate using a theory for idealized bores (D_{bore}) (Battjes and Janssen 1978; Roelvink 1993; Baldock et al. 1998b; Alsina and Baldock 2007; Apotsos et al. 2007). SWAN and XBeach both implement parametric wave breaking formulations. Though there are numerous parametric wave breaking models available, we choose to focus on the most highly used wave breaking formulation for each model.

SWAN (by default) uses the Battjes and Janssen (1978) formulation (herein after BJ78). BJ78 calculates the mean energy dissipation rate per unit horizontal area due to depth-limited wave breaking (D_{br}) as:

$$D_{br} = D_{bore} Q_{br}, \tag{2.6}$$

where D_{bore} is the energy dissipation rate of an idealized individual breaking wave and Q_{br} is the time-averaged fraction of breaking or broken waves. D_{bore} is calculated as:

$$D_{bore} = \frac{1}{4} \rho g f_{mean} B H_{max}^2, \tag{2.7}$$

where f_{mean} is the mean wave frequency, B is an empirical breaking intensity coefficient (by default $B=1$), and H_{max} is the maximum possible individual wave height in a total local water depth. H_{max} is calculated as:

$$H_{max} = \gamma\left(h_0 + \bar{\eta}\right), \tag{2.8}$$

where γ is an empirical "breaker parameter". While γ is theoretically related to the

maximum wave height to water depth ratio $\left(\gamma = H_{max} / (h_0 + \bar{\eta})\right)$, in practice it is usually used as a model tuning parameter.

The time-averaged fraction of breaking waves Q_{br} varies between 0 to 1, with 0 representing no breaking and 1 representing complete breaking. In BJ78 Q_{br} is estimated from a Rayleigh wave height distribution truncated at H_{max} as:

$$\frac{1-Q_{br}}{\ln Q_{br}} = -8\frac{E}{H_{max}^2}, \tag{2.9}$$

where E is the total wave energy variance.

XBeach (by default) uses a modified form of the parametric dissipation formulation of Roelvink (1993) (herein after R93) to model sea-swell wave breaking dissipation. Energy dissipation due to wave breaking D_{br} is calculated in the same manner as in Eq. (2.6) but with D_{bore} calculated as:

$$D_{bore} = \frac{1}{4}\rho g f_{rep} B H_{rms,SS}^2 \frac{H_{rms,SS}}{h_0 + \bar{\eta}'}, \tag{2.10}$$

where f_{rep} is a representative frequency, B is the breaking intensity coefficient (by default B=1), $H_{rms,SS}$ is the root mean square (*rms*) wave height in the *SS* frequency band, and $\bar{\eta}'$ is the water level deviation from h_0 on the time-scale of individual wave groups. The fraction of breaking waves is calculated as (Roelvink 1993):

$$Q_{br} = 1 - exp\left[-\left(\frac{H_{rms,SS}}{H_{max}}\right)^n\right], H_{max} = \frac{\gamma \tanh k\left(h_0 + \bar{\eta}'\right)}{k}, \tag{2.11}$$

where n is a coefficient (n = 10 by default; see Roelvink (1993) for discussion) and k is the wave number. There are thus several key differences between BJ78 and R93, as they are implemented in SWAN and XBeach, respectively. The BJ78 D_{bore} formulation is dependent on wave frequency and water depth, whereas the R93 D_{bore} formulation is dependent on wave frequency, as well as the local values of $H_{rms,SS}^2$ and $H_{rms,SS} / (h_0 + \bar{\eta}')$. Also, in XBeach due to the separation of *SS* and *IG* waves D_{br} is applied only to *SS* waves, however in SWAN D_{br} is applied to the entire wave spectrum and distributed at a rate proportional to the wave energy variance at each frequency. Infragravity wave breaking in XBeach is modeled as in SWASH using a shock-capturing conservation scheme (Zijlema and Stelling 2008); however, by default XBeach does not include non-hydrostatic terms, eliminating the need for a metric to determine the onset of infragravity wave breaking.

2.3.2. Bottom stress

Wave energy and momentum are dissipated due to bottom stresses, which is related to the turbulent vertical fluxes of horizontal momentum (Feddersen et al. 2003). Wave and current bottom stresses are commonly treated independently using quadratic bottom friction formulations with an empirical friction coefficient. SWAN and XBeach each include a term for *SS* wave energy dissipation due to bottom roughness in the wave action equation. SWASH and XBeach both add terms to the momentum equations to account for dissipation due to bottom roughness. Although bottom stress is known to be an important source of wave dissipation in coral reef environments (e.g., Lowe et al. 2005b) in this paper we chose to focus mainly on wave breaking dissipation.

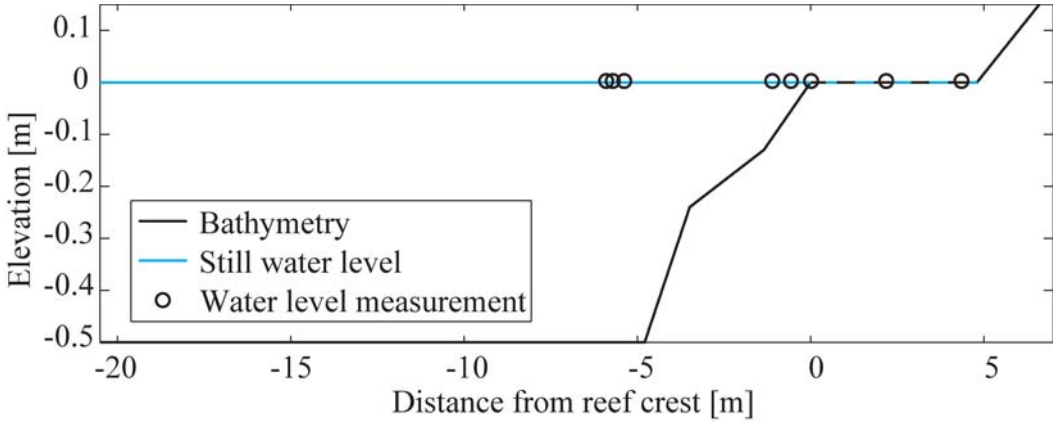

Figure 2.1: Laboratory setup for the University of Michigan flume experiment (Demirbilek et al., 2007).

2.4. Model application to a laboratory reef

Laboratory experiments by Demirbilek et al. (2007) were used to assess the performance of each of the numerical models. The laboratory study, conducted in a wind-wave flume at the University of Michigan, consisted of 29 tests conditions carried out on a 1:64 scale model of a fringing reef type profile typical of the southeast coast of Guam (Figure 2.1). The flume was 35 m long, 0.7 m wide and 1.6 m high, with smooth side walls and a smooth plastic bed. With the geometric scaling factor of 1:64, the flume length corresponds to a transect length of 2.24 km in the field. The fringing reef profile consisted of a composite slope with a 1:10.6 fore reef slope, a 4.8m (~300 m field scale) long horizontal reef flat, and a 1:12 sloping beach (Figure 2.1). The duration of simulations was 900 s (2 hours field scale with 1:8 Froude scaling of time) with the final 800 s used in the analysis. Water surface elevations were measured using eight capacitance type wave gauges with a sampling frequency of 20 Hz (2.5 Hz field scale). Irregular waves based on a JONSWAP (Hasselmann et al. 1980) spectrum (peak enhancement factor 3.3) were generated with a wedge type wave maker with significant

wave heights up to 10 cm (6.4 m field scale) and peak periods from 1.0 to 2.5 s (8 to 20 s field scale). The still water depth over the reef flat ($h_{0,r}$) was also varied. A summary of the conditions during the 29 test conditions are included in Table 2.2 (first column; Table 2.2).

Simulations were initially performed using "recommended" model coefficient values (hereafter referred to as "untuned" simulations) as documented for each model. This provides an estimate of the errors expected in the application of an untuned model. Testing the untuned models is crucial as in many cases limited or no calibration data is available, and in practice untuned models are frequently relied upon to provide predictive skill. This testing is particularly important in enviroments, including reefs, which differ from the environments used to establishing the "default" untuned wave breaking parameters. The key depth-limited wave breaking parameter for each model (α in SWASH and γ in both SWAN and XBeach) was then systematically varied over a full range of physically-reasonable values in order to determine the optimal values for each test condition. Extensive testing of the key wave breaking parameter within each model gives insight into each model's response to the free parameter allowing the sensitivity, tune-ability, and appropriate values to be assessed.

2.4.1. Model setup

Numerical simulations were performed with each model configured in a one-dimensional mode using a uniform horizontal grid size of 0.02 m with a minimum threshold water depth of 0.005 m. SWASH and XBeach simulations were run for durations of 900 s, with a time step determined by imposing a maximum Courant number of 0.5. SWAN simulations were performed in a stationary mode. All models were forced on the offshore boundary with a wave energy spectra derived for each test condition from the measured water level time series at the offshore gauges (Gauges 1-3; Figure 2.1). Directional filtering of the offshore water level gauges was performed, using a three point method (Mansard and Funke 1980), to remove offshore directed wave energy. To simulate the smooth plastic bed of the flume a dimensionless bottom drag coefficient of C_d = 0.001 was used for SWASH and XBeach simulations. This low C_d value had a negligible contribution to the overall wave dissipation, which was overwhelmingly dominated by wave breaking. The wave action equations for SWAN and XBeach include an optional term parameterizing wave frictional dissipation; by default this term is neglected in XBeach and included in SWAN. Here we do not include *SS* wave friction in the simulations. This is also consistent with Filipot and Cheung (2012), who neglect wave friction when applying SWAN to the same dataset.

Following Zijlema (2012), SWASH was run with the discrete upwind momentum-conservative advection scheme. Although, SWASH can be configured with multiple vertical layers here only a single vertical layer is implemented. Depth-limited wave breaking was accounted for with the onset of breaking controlled by $\alpha = 0.6$ in the untuned case. The coefficient α was varied from 0.1 to 5.0 in increments of 0.01 in the sensitivity analysis. Water level time series output from the model were then exported at the gauge locations at 20 Hz.

SWAN was run in a stationary mode with triad interactions and frequency shifts activated, wave setup activated, and white capping deactivated. The simulations were performed with 36 directional bins from 0 to 360^o, and 42 logarithmically distributed frequency bins from 0.01 to 10 Hz. Depth-limited wave breaking was modeled using the BJ78 formulation with the default $\gamma = 0.73$ for the untuned case. However, γ was varied from 0.1 to 1.2 in increments of 0.01 in the sensitivity analysis. One-dimensional wave energy spectra were exported from SWAN at the gauge locations.

Depth-limited wave breaking in XBeach was modeled using the R93 formulation with the default $\gamma = 0.55$ for the untuned case. Like SWAN, γ was varied from 0.1 to 1.2 in increments of 0.01 for the sensitivity analysis. By default XBeach includes a roller energy balance; this was activated in the current study with the default β_D (roller face slope) value of 0.1 (Reniers and Battjes 1997). Water level time series were exported at the gauge locations at 20 Hz.

2.4.2. Data processing and performance metrics

Measured and simulated water level time series were used to compute one dimensional wave energy spectra $C_{\eta\eta}(f)$ using the Welch's averaged, modified periodogram method with a Hanning window and a segment length of 2^9 samples (~26 s). The *SS rms* wave height ($H_{rms,SS}$) was calculated as:

$$H_{rms,ss} = \sqrt{8\int_{f_l}^{\infty} C_{\eta\eta}\, df}\,, \tag{2.12}$$

where f_l is the boundary between *SS* and *IG* frequency bands. In agreement with Sheremet et al. (2011) and others, f_l was taken as half the peak forcing frequency of each simulation (i.e. $f_l = 0.5 f_p$). XBeach uses a representative frequency for the *SS* band and does not model the *SS* spectra, thus the mean $H_{rms,SS}$ for XBeach was exported directly from the model. Likewise, for *IG rms* wave height ($H_{rms,IG}$) was calculated as:

$$H_{rms,IG} = \sqrt{8\int_{0}^{f_l} C_{\eta\eta}\, df}\,. \tag{2.13}$$

Following Apotsos et al. (2008), model performance was quantified using the weighted *rms* percent error metric (*WRPE*), defined as:

$$WRPE = \sqrt{\sum_n \left[\left(\frac{obs_n - pred_n}{obs_n} \right)^2 * weight_n \right]} *100\%, \text{ where} \quad (2.14)$$

$$weight_n = \frac{dist_{n-1} + dist_{n+1}}{dist_{tot}}, \quad (2.15)$$

where *n* is the gauge number, *obs* and *pred* are the observed and predicted values, respectively, *dist* is the distance between gauges, and $dist_{tot}$ is the total distance between all gauges. *WRPE* was calculated for $H_{rms,SS}$, $H_{rms,IG}$, and $\bar{\eta}$, denoted *WRPE SS*, *WRPE IG*, and *WRPE* $\bar{\eta}$, respectively. Offshore gauges used for the model boundary forcing condition were excluded from this analysis and hence only Gauges 5-9 (Figure 2.1) were used in the calculation. Model tuning was assessed using *WRPE SS* rather than a combination of *WRPE SS and WRPE IG*, given that depth-limited wave breaking occurs primarily in the *SS* frequency band through the surf zone and wave breaking formulations have been developed primarily to predict *SS* decay in the surf zone. The percent error reduction that can be achieved with model tuning was also estimated using the Brier Skill Score (*BSS*) (Murphy and Epstein 1989; Ruessink et al. 2003; Apotsos et al. 2008):

$$BSS = \left[1 - \frac{WRPE_{tuned}}{WRPE_{untuned}} \right] *100\%. \quad (2.16)$$

We define *BSS SS*, *BSS IG*, and *BSS* $\bar{\eta}$ as the *BSS* based on *WRPE SS*, *WRPE IG*, *and WRPE* $\bar{\eta}$, respectively.

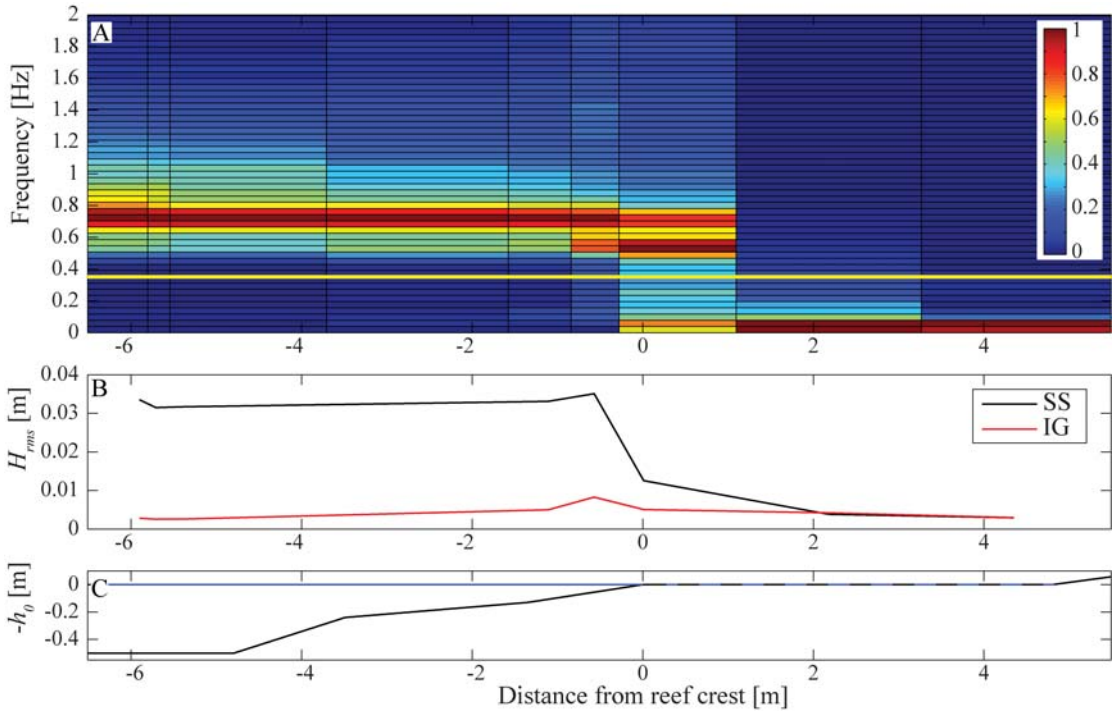

Figure 2.2: (A) Normalized wave energy spectrum (normalized by maximum spectral density at each location) and (B) *rms* wave heights for sea-swell ($H_{rms,SS}$) and infragravity ($H_{rms,IG}$) waves across (C) the reef profile for Test no. 35 ($H_{rms,SS}$ = 0.032 m; T_p = 1.42 s; $h_{0,r}$ = 0.00 m).

2.5. Results

2.5.1. Test no. 35

The laboratory observations showed a rapid dissipation of *SS* energy near the reef crest, an increase in the proportion of *IG* energy over the reef flat, and wave setup across the reef. Figure 2.2 shows an example of this observed wave transformation for Test no. 35 ($H_{rms,ss}$ = 0.032 m (2.0 m field scale); T_p = 1.42 s (11 s field scale); $h_{0,r}$ = 0.00 m (0.0 m field scale), which had an intermediate wave height and period. Test no. 35 also had its still water level located at the elevation of the reef flat, which should provide a challenge for the models. Test no. 35 is used throughout this paper to highlight many of the common features of the broader set of Test conditions. Wave breaking near the reef crest resulted in the largest dissipation of *SS* and *IG* energy between Gauges 6 (x = -0.57 m) and 7 (x = 0.010 m) (Figure 2.2). Offshore of the reef crest (x < 0 m) the majority of the incident wave energy is in the SS frequencies as expected (Figure 2.2 A). Between Gauges 6 and 7 the majority of wave breaking occurs with the strong dissipation of *SS* energy resulting in an increasing proportion of *IG* energy. The proportion of *IG* to *SS* energy further increases on the reef flat, with $H_{rms,SS}$ and $H_{rms,IG}$ becoming roughly equal magnitude over most of the reef flat (Figure 2.2 A,B).

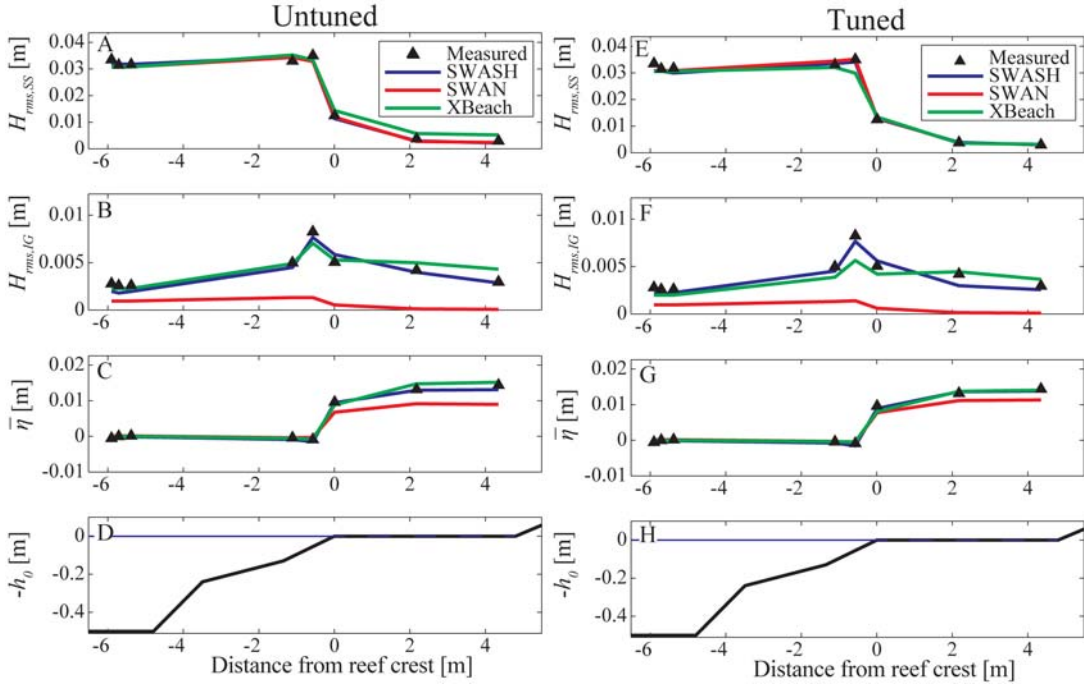

Figure 2.3: Measured and predicted $H_{rms,SS}$, $H_{rms,IG}$, and $\bar{\eta}$ across the fringing reef profile for Test no. 35 ($H_{rms,SS}$ = 0.032 m; T_p = 1.42 s; $h_{0,r}$ = 0.00 m). Model predictions are shown with untuned (left column) and tuned (right column) breaking parameters. The reef profile is shown on the bottom row.

With untuned wave breaking parameters, SWASH (α = 0.6) and SWAN (γ = 0.73) reproduced observed *SS* wave transformation well (Figure 2.3 A). XBeach (γ = 0.55) slightly over predicted $H_{rms,SS}$ on the reef flat (Figure 2.3 A). For this Test no. 35, tuning γ for XBeach gave a smaller than default optimal γ value of 0.33 (untuned γ = 0.55), which corrected the over prediction of $H_{rms,SS}$ on the reef flat and reduced the *WRPE SS* by 85% (Figure 2.3 A,E; Table 2.2). This tuning of XBeach, however, resulted in an underestimate of $H_{rms,SS}$ at Gauges 5 and 6 (Figure 2.3 E). Conversely, tuning SWAN gave a greater than default optimal γ value of 0.85 (untuned γ = 0.73) with a *WRPE SS* reduction of 72% (Table 2.2). Tuning SWASH gave a much greater optimal α value of 3.21 compared to the untuned value of α = 0.6, with a *WRPE SS* reduction of 91% (Table 2.2).

For Test no. 35 ($H_{rms,ss}$ = 0.032 m; T_p = 1.42 s; $h_{0,r}$ = 0.00 m) model performance in predicting the *IG* wave transformation was more varied (Figure 2.3 B,F). SWASH and XBeach reproduced the overall *IG* development across the reef relatively well using the untuned breaking parameters; however SWAN greatly under predicted *IG* energy across the reef profile, and showed nearly complete dissipation of *IG* energy on the reef flat (Figure 2.3 B,F).

When the key wave breaking parameters were tuned to minimize *WRPE SS*, this had varying effects on the accuracy of the *IG* prediction in both models (*BSS IG*; Table 2.2). For SWASH, tuning α to optimize the $H_{rms,ss}$ prediction resulted in a drastic decrease in the accuracy of the *IG* wave predictions (*BSS IG* = -115%; Table 2.2). Conversely, for XBeach tuning γ reduced the over prediction of $H_{rms,IG}$ on top of the reef and improved the *IG* prediction (*BSS IG* = 28%; Table 2.2). SWAN showed negligible improvement in the $H_{rms,IG}$ prediction with tuning(*BSS IG*=1%; Table 2.2).
Wave setup $\bar{\eta}$ over the reef profile was well-predicted with SWASH and XBeach for Test no. 35 using the untuned breaking parameters, but was under predicted using SWAN (Figure 2.3 C). These predictions were slightly improved when tuning the breaking parameters (Figure 2.3 G; Table 2.2).

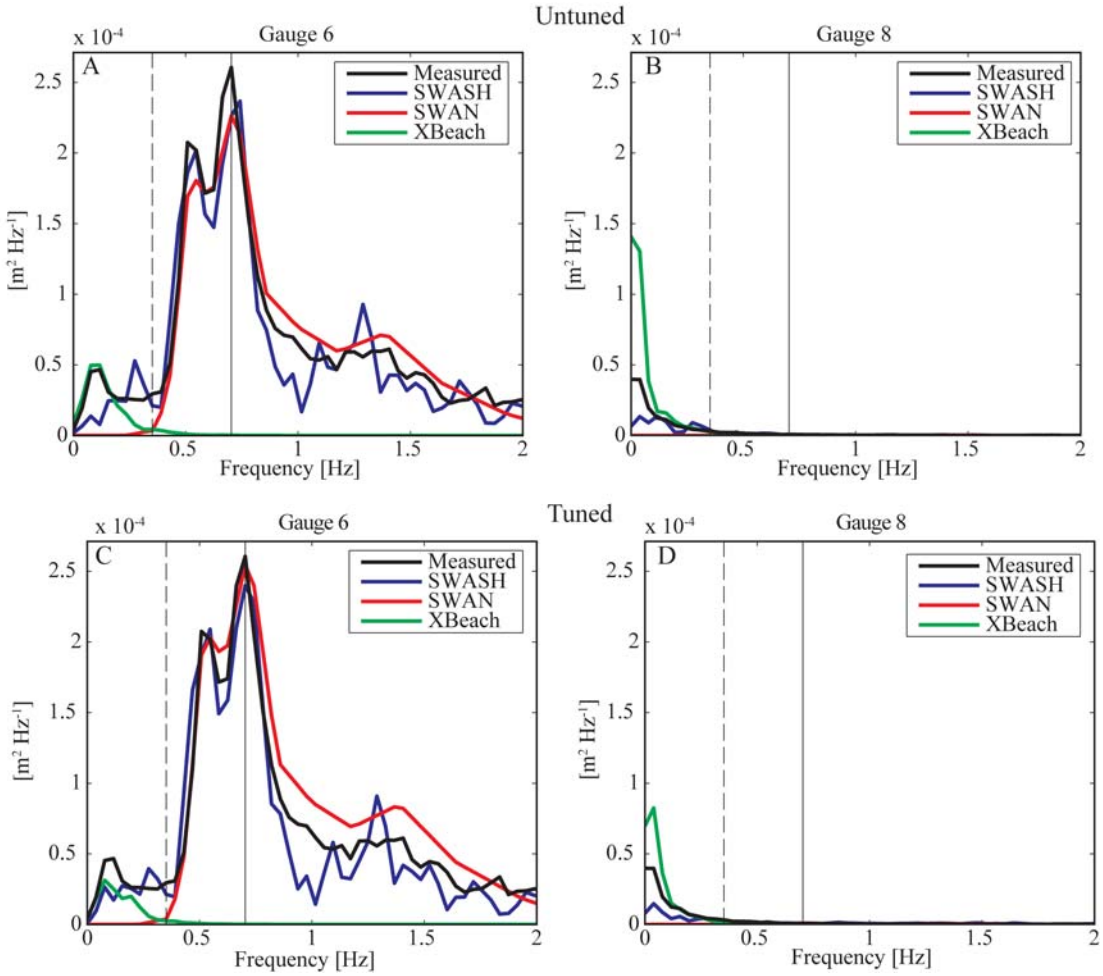

Figure 2.4: Measured and predicted wave energy spectra at Gauge 6 (shoaling region; left column) and Gauge 8 (reef flat; right column) for Test no. 35 ($H_{rms,SS}$ = 0.032 m; T_p = 1.42 s; $h_{0,r}$ = 0.00 m). Model predictions with untuned (upper row) and tuned (lower row) breaking parameters are shown for SWASH (blue line), SWAN (red line), and Xbeach (green line). The peak forcing frequency (vertical solid black line) and the *SS*-*IG* frequency cut-off (vertical dashed black line) are shown for reference. XBeach simulates *SS* waves using a single representative frequency, so it is only possible to compare the low-frequency spectra for XBeach.

Measured and predicted wave spectra are shown for Test no. 35 for two sites: the shoaling region (Gauge 6; Figure 2.4 A,C) and on the reef flat (Gauge 8; Figure 2.4 B,D). At Gauge 6 the majority of the energy was in the *SS* band, centered on peak forcing frequency (indicated by the vertical black line; Figure 2.4 A,C). Measured wave energy in the *IG* band was relatively constant between these two gauges. Directional (i.e., shoreward versus seaward) analysis of the offshore water level showed that a significant proportion of *IG* energy was propagating offshore. SWASH and SWAN accurately predicted the distribution of *SS* energy in the shoaling region (Gauge 6; Figure 2.4 A,C) and the dissipation of *SS* energy on the reef flat (Gauge 8; Figure 2.4 B,D). Note that XBeach simulates *SS* using a single representative frequency, so it is only possible to compare the low-frequency spectra for XBeach.

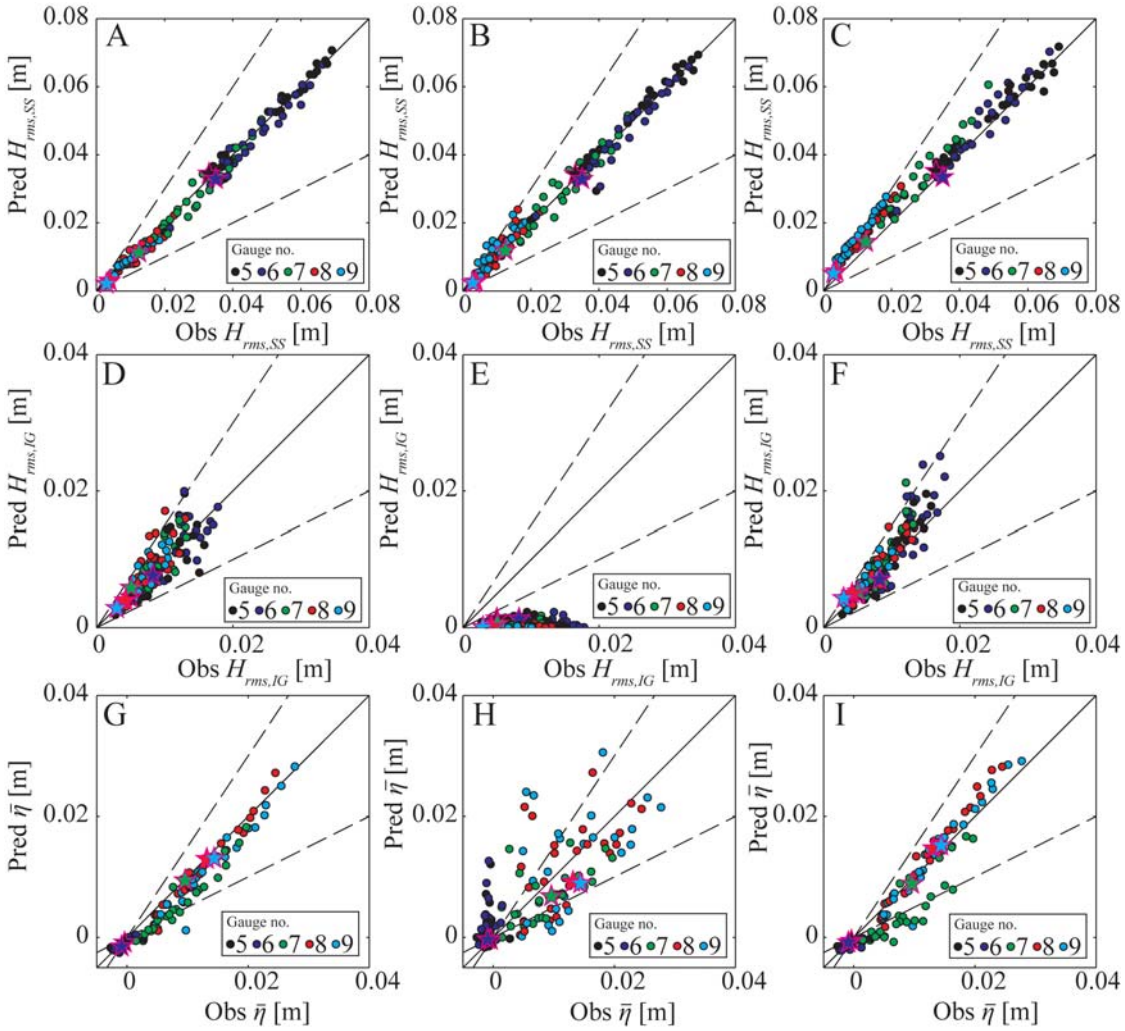

Figure 2.5: Comparison of the untuned model predictions with the observations of: $H_{rms,SS}$ (first row), $H_{rms,IG}$ (second row), and $\bar{\eta}$ (third row). Measured values are given on the *x*-axis and simulation results are given on the *y*-axis for SWASH (first column), SWAN (second column), and XBeach (third column). The 1:1 line (solid black diagonal lines) and 50% error bounds (dashed black lines) are given for reference. Point colors correspond to gauge locations as given in the legend. Stars are used to highlight Test no. 35.

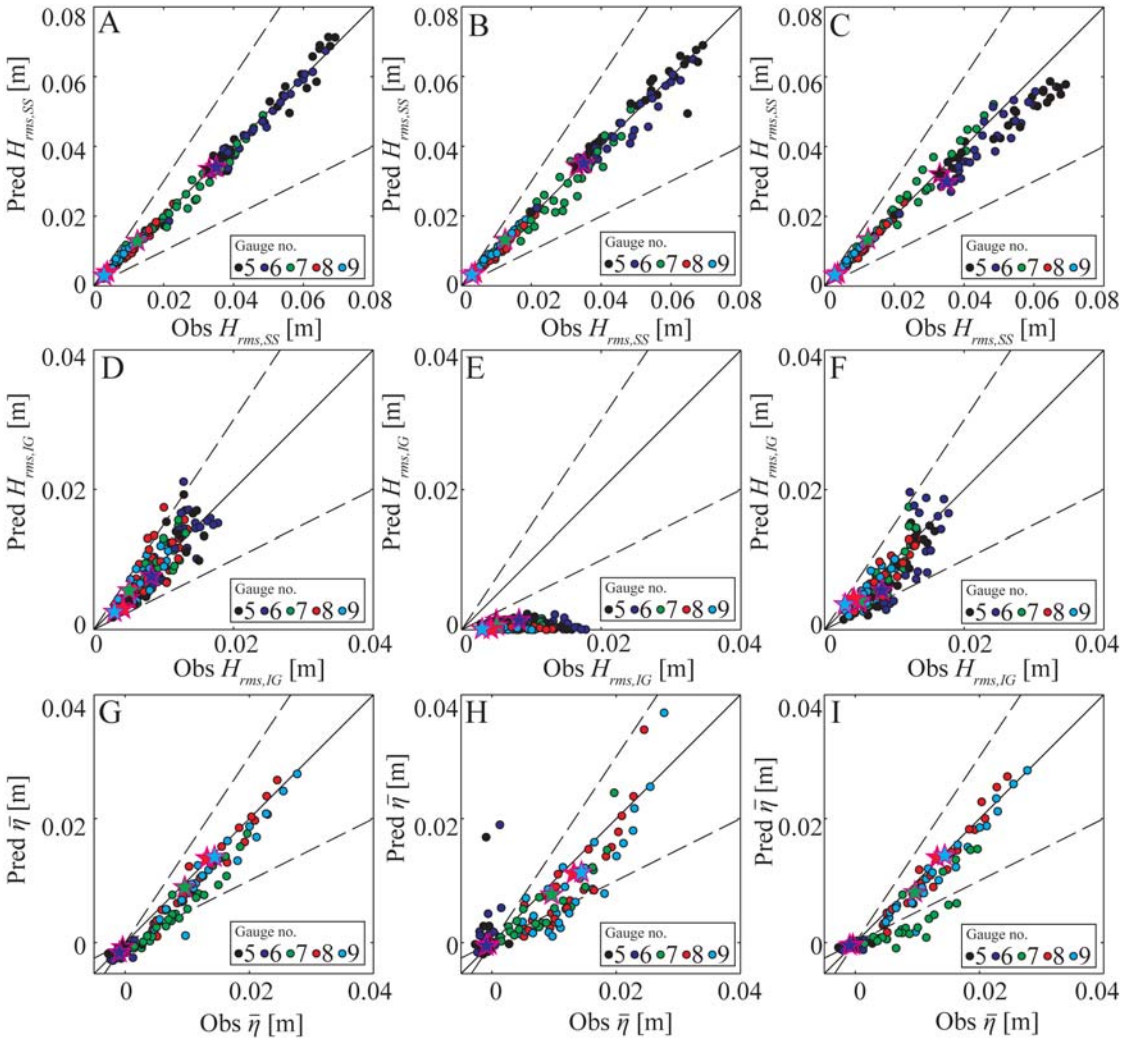

Figure 2.6: Comparison of the tuned model predictions with the observations of: $H_{rms,SS}$ (first row), $H_{rms,IG}$ (second row), and $\bar{\eta}$ (third row). Measured values are given on the *x*-axis and simulation results are given on the *y*-axis for SWASH (first column), SWAN (second column), and XBeach (third column). The 1:1 line (solid black diagonal lines) and 50% error bounds (dashed black lines) are given for reference. Point colors correspond to gauge locations as given in the legend. Stars are used to highlight Test no. 35.

2.5.2. Summary of all Test conditions

When evaluating all Test cases, SWASH and XBeach with untuned breaking parameters provided reasonable agreement with the measured wave heights (both $H_{rms,SS}$ and $H_{rms,IG}$) and $\bar{\eta}$ for all 29 conditions (Figure 2.5). SWAN accurately predicted $H_{rms,SS}$, but failed to predict $H_{rms,IG}$ (Figure 2.5, middle row). Predicted $\bar{\eta}$ for SWAN showed considerably more error than SWASH and XBeach (Figure 2.5, bottom row). For all three models, the accuracy of $H_{rms,SS}$ predictions were improved by tuning the wave breaking parameters (Table 2.2; Figure 2.6). The maximum *WRPE SS* for all of the untuned models and all Test cases was 92%, but with tuning the maximum *WRPE SS* was reduced to <17% (Table 2.2; Figure 2.7). Predictions of $H_{rms,SS}$ were

improved most notably with tuning for XBeach (Figure 2.7). Tuning the breaking parameters to minimize *WRPE SS*, gave mixed results in terms of the accuracy of both the $H_{rms,IG}$ and $\bar{\eta}$ predictions with some tests showing an improvement and others showing a substantial decrease in accuracy (Figure 2.7).

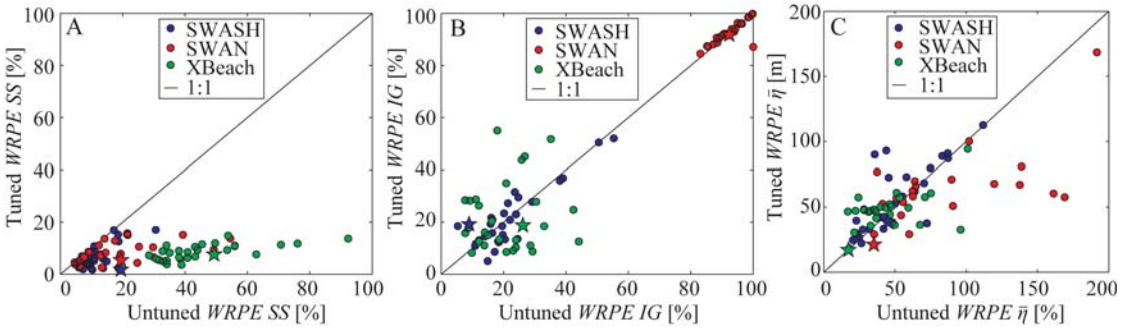

Figure 2.7: Comparison of untuned (*x*-axis) and tuned (*y*-axis) *WRPE SS*, *WRPE IG*, and *WRPE* $\bar{\eta}$ for the 29 test conditions for SWASH, SWAN, and XBeach. The 1:1 line is shown as the solid black line. Points above the 1:1 line are test conditions were the tuned model was less accurate than the untuned model; points below the 1:1 line are test conditions were the tuned model was more accurate than the untuned model. Stars are used to highlight Test no. 35. Note the scale change for *WRPE* $\bar{\eta}$.

2.6. Discussion

The key wave breaking parameters in SWASH (α), SWAN (γ), and XBeach (γ) have some physical basis, but in practice are mainly used as free parameters utilized to calibrate wave models.

2.6.1. The role of α in SWASH

The α breaking parameter within the shock-capturing scheme in SWASH controls the onset of breaking when the criteria given by Eq. (2.5) $\partial\eta/\partial t > \alpha\sqrt{g\left(h_0+\eta\right)}$ is satisfied. Given that $\partial\eta/\partial t$ is kinematically related to the slope of the free surface $\partial\eta/\partial x$ for a progressive wave, higher values of α increase the threshold surface slope for the on-set of wave breaking, thus allowing for steeper wave faces prior to wave breaking and moving the break point shoreward. In general increasing α allows for a larger wave height to develop prior to breaking, and in our case increases the maximum breaking dissipation (dissipation between Gauges 6 and 7), but decreases the width of the surf zone thereby increasing $H_{rms,SS}/(h_0+\bar{\eta})$ on the reef flat. Optimal α values averaged 1.5, considerably higher than the untuned value of 0.6 (Table 2.2), implying that the wave face prior to breaking was steeper (~55^o) than the default value of α = 0.6 (~25^o). This is physically consistent with the occurrence of plunging breakers on the steep forereef slope, although no detailed data to confirm breaking slope (e.g., from video imagery) are available in the Demirbilek et al. (2007)

study. The laboratory study of Ting and Kirby (1994) confirms that as expected $\partial\eta / \partial t$ is greater for plunging waves than spilling waves.

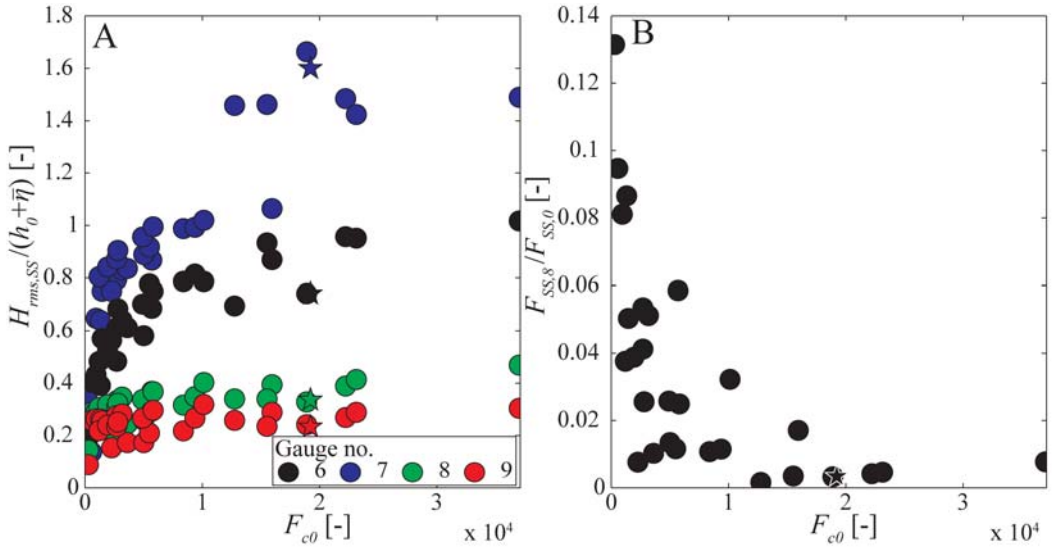

Figure 2.8: Observed $H_{rms,SS} / (h_0 + \bar{\eta})$ and dissipation (as expressed by $F_{SS,8}/F_{SS,0}$ where $F_{SS,8}$ and $F_{SS,0}$ are *SS* wave energy flux on the reef flat (Gauge 8) and deep water respectively) versus the non-linearity parameter (F_{c0}) (see Section 2.6.3 for a definition and discussion of F_{c0}). Stars are used to highlight Test no. 35.

2.6.2. The role of the breaker parameter γ (XBeach and SWAN)

The breaker parameter γ describes the maximum stable wave height to water depth ratio ($H_{max} / (h_0 + \bar{\eta})$), however optimal γ values were found to differ in magnitude between SWAN (using BJ78) and XBeach (using R93), and in some cases in the direction in which these parameters had to be tuned to generate optimal results. As seen in Figure 2.8 A (see Section 2.6.3 for a definition and discussion of F_{c0}), the measured values of $H_{rms,SS} / (h_0 + \bar{\eta})$ vary widely across the reef profile; for example for Test no. 35 values reach 1.6 at Gauge 7 and 0.34 at Gauge 8. As a consequence a single maximum stable value can be difficult to establish. XBeach using the R93 wave breaking formulation showed that lower γ values relative to the default (untuned) value were optimal; i.e., the average optimal γ for these test conditions was γ = 0.33 versus γ = 0.55 for the untuned case (Table 2.2). However, in contrast to XBeach, an average tuned value of γ ~0.70 (untuned γ = 0.73) was found for SWAN using BJ78, roughly equal to the untuned value. Importantly, γ in both R93 and BJ78 has a clear physical definition as $H_{rms,SS} / (h_0 + \bar{\eta})$; hence, optimal γ values should ideally not differ among different parametric wave breaking dissipation formulations.

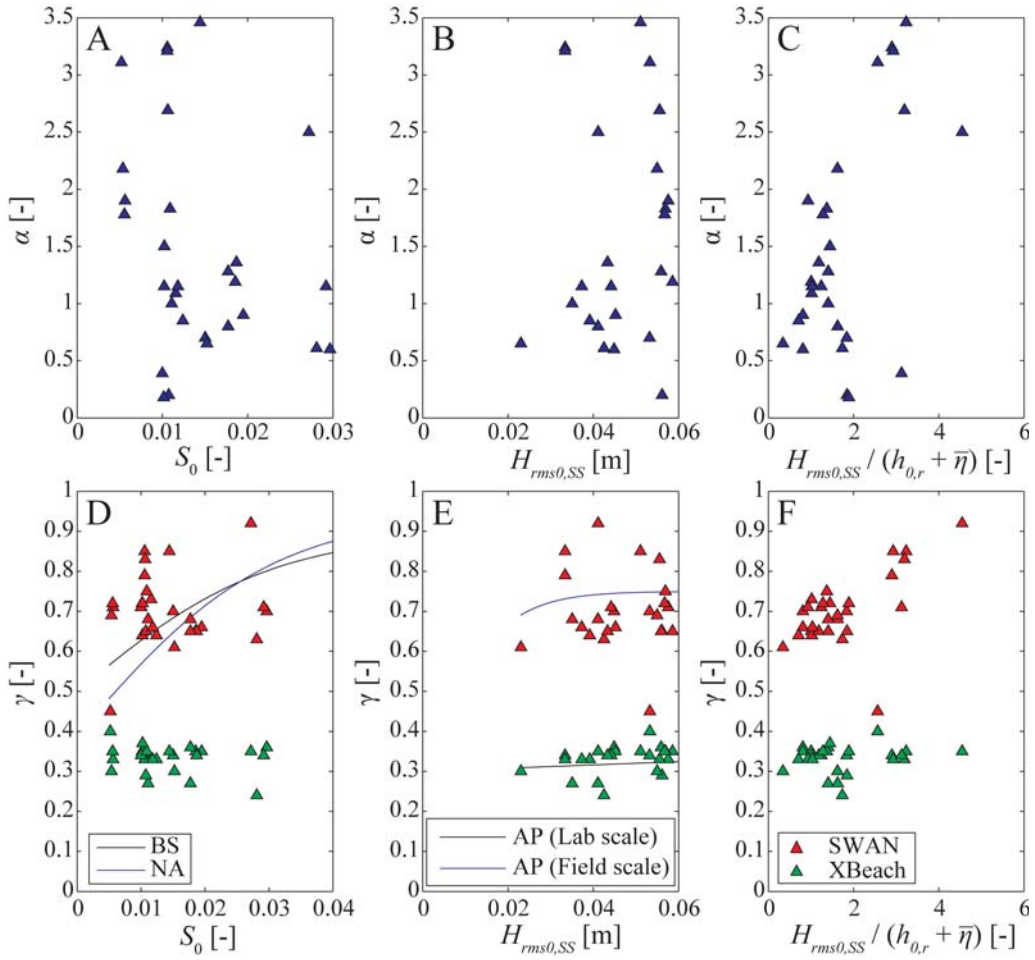

Figure 2.9: Tuned α values for SWASH (top row) and tuned γ values for SWAN (bottom row; red triangles) and XBeach (bottom row; green triangles) versus S_0, $H_{rms0,SS}$, and $H_{rms0,SS} / (h_{0,r} + \overline{\eta})$. The Battjes and Stive (1985) (BS) and the Nairn (1990) (NA) S_0 dependent γ formulations are shown in (A). The Apotsos et al. (2008) $H_{rms0,SS}$ dependent γ formulation for BJ78 (SWAN) is shown in (B) for laboratory scale and field scale (1:64 geometric scaling).

In SWAN the dissipation of an individual wave, D_{bore} is proportional to H_{max}^2 (Eq. (2.7)) and hence through Eq. (2.8) is proportional to γ^2. This is not the case for XBeach, where D_{bore} is proportional to $H_{rms,SS}^3 / \left(h_0 + \overline{\eta}\right)$ and hence dependent on the local (not maximum) wave height per Eq. (2.10). These deviations in the formulations are the result of assumptions made in their derivation. Both BJ78 and R93 model formulation begin with:

$$D_{br} = D_{bore} Q_{br}, \text{ and} \tag{2.17}$$

$$D_{bore} = \frac{1}{4} \rho g f B H^2 \frac{H}{\left(h_0 + \overline{\eta}\right)}, \tag{2.18}$$

where H is a representative local wave height. But BJ78 then assumes that $H / (h_0 + \overline{\eta})$ is roughly 1 and thus neglects the term; H is assumed to be H_{max} yielding Eq. (2.7). R93

assumes H to be equivalent to $H_{rms,SS}$ yielding Eq. (2.10). These seemingly minor differences in assumptions lead to divergence of the model predictions and are believed to be the main source in the difference in default and tuned γ values between the SWAN and XBeach. H_{max} and Q_{br} formulations also differ between the two models. Notably Q_{br} in R93 increases more rapidly than BJ78 as $H_{rms,SS} / (h_0 + \overline{\eta})$ approaches γ. When increasing γ in either model this results in shoreward shift of the break point and an increase in $H_{rms,SS} / (h_0 + \overline{\eta})$ on the reef flat. In SWAN increasing γ also results in a γ^2 increase in D_{bore} (assuming $\overline{\eta}$ remains constant). The breaking dissipation rate D_{bore} can be thought of as the maximum dissipation rate (with Q_{br} = 1 or 100% wave breaking $D_{br} = D_{bore}$). In SWAN the maximum dissipation rate can be tuned by changing γ, whereas in XBeach the maximum dissipation rate is independent of γ.

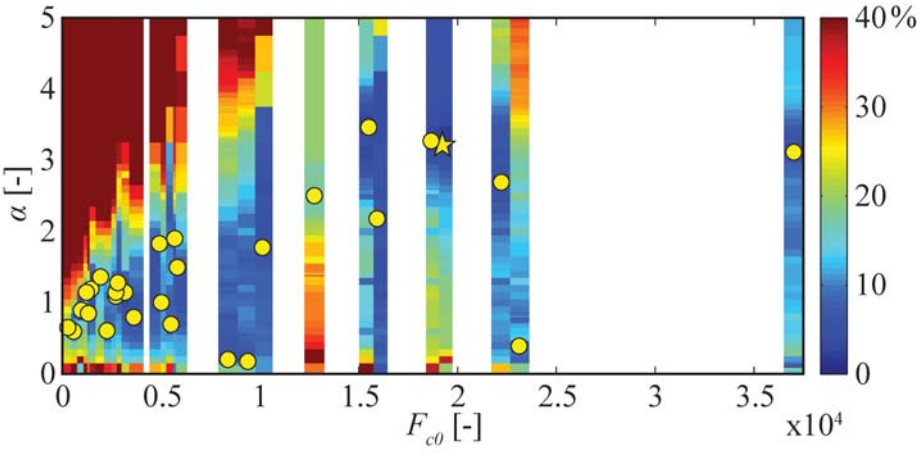

Figure 2.10: Error in $H_{rms,SS}$ predictions (*WRPE SS* shown with color bands) for SWASH as a function of F_{c0} and α. Individual color bands give *WRPE SS* for a given test condition and α. Yellow dots give the optimum α for each test condition. The yellow star is the optimum α for Test no. 35 ($H_{rms,SS}$ = 0.032 m; T_p = 1.42 s; $h_{0,r}$ = 0.00 m).

Test no. 35 provides an example of this difference in response to γ in SWAN and XBeach. Despite the smaller default value of γ in XBeach, with untuned γ values XBeach predicts higher $H_{rms,SS}$ on the reef flat than SWAN and over predicts wave height over the reef flat (Figure 2.3 A). This over prediction of $H_{rms,SS}$ on the reef flat by XBeach was also observed in most Test cases for the untuned simulations (Figure 2.5 G). To correct this over prediction, a much lower than default γ is needed (Table 2.2). Lowering γ results in a seaward shift of the break point and a broadening of the surf zone, thus under estimating the dissipation between Gauges 6 and 7 but better matching $H_{rms,SS}$ across the reef flat (Figure 2.3 E). This under estimate in dissipation, hence reducing the local radiation stress gradient, leads to a slight under estimate of $\overline{\eta}$ at Gauge 7 (Figure 2.3 G). This can also be observed at Gauge 7 for all Test cases in

Figure 2.6 I (green points below the 1:1 line). With the lower γ broadening the surf zone, dissipation continues between Gauges 7 and 8 and the overestimate in $H_{rms,SS}$ and under estimate of $\bar{\eta}$ are corrected (Figure 2.3 E,G for Test no. 35 and Figure 2.6 G,I for all Test cases).

2.6.3. Prediction of α and γ

Ideally, optimal α and γ values would be related to test conditions through a non-dimensional parameter. For both laboratory and field data, obtained on plane and barred beach environments, Battjes and Stive (1985) (herein after BS) found optimal γ values to be weakly dependent on offshore wave steepness (S_0), with γ given by:

$$\gamma = 0.5 + 0.4\left[\tanh\left(33S_0\right)\right]. \tag{2.19}$$

Nairn (1990) (herein after NA) modified the empirical coefficient in *BS*, with γ given by:

$$\gamma = 0.39 + 0.56\left[\tanh\left(33S_0\right)\right]. \tag{2.20}$$

The NA formulation has subsequently been adopted for application to steep beaches by Baldock et al. (1998a) and Janssen and Battjes (2007). In a review of existing predictive γ formulations, Apotsos et al. (2008) instead found that optimal γ values for field observations, on mild-sloping beaches, were dependent on the offshore wave height ($H_{rms0,SS}$) and varied between wave breaking formulations. Apotsos et al. (2008) (herein after AP) developed a universal empirical relationship between γ and $H_{rms0,SS}$, with the general form:

$$\gamma = c_1 + c_2\left[\tanh\left(c_3 H_{rms0,SS}\right)\right], \tag{2.21}$$

where c_1, c_2, and c_3 are empirical coefficients fitted to observations. From an extensive review of field observations on sandy beaches, Apotsos et al. (2008) gives $c_1 = 0.30$, $c_2 = 0.45$, and $c_3 = 0.90$ m^{-1} for BJ78; R93 was not included in Apotsos et al. (2008). The dimensional dependence of AP would imply that contrary to conventional thinking γ could differ between laboratory and field measurements. On fringing reef profiles measured γ values at the break point have been related to the non-dimensional relative water depth $(h_{0,r} + \bar{\eta}) / H_{rms0,SS}$ (see Yao et al. (2012b) and references therein).

For the steep-slope Demirbilek et al. (2007) dataset we do not find a clear dependence of the optimal α and γ values on S_0 (Figure 2.9) in contrast to the findings of Battjes and Stive (1985) and Nairn (1990). There does however appear to be a general trend of increasing optimal α and γ values with $H_{rms0,SS} / (h_{0,r} + \bar{\eta})$ (as well as with $H_{rms0,SS}$ for XBeach) (Figure 2.9).

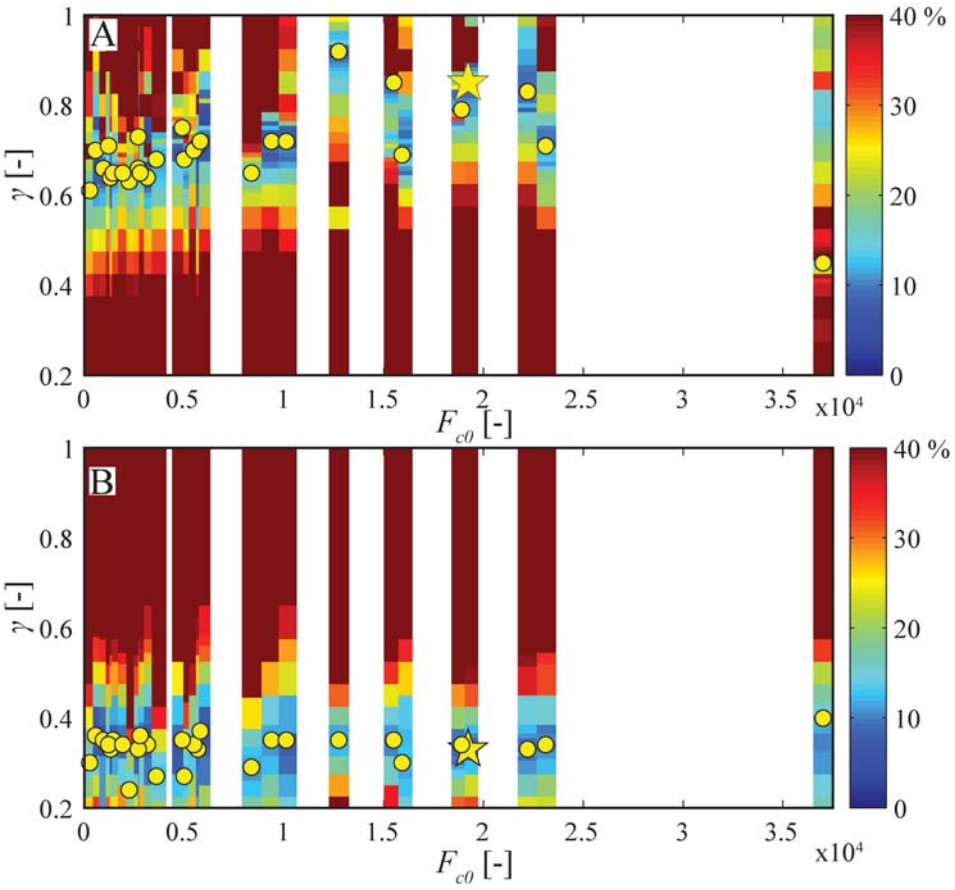

Figure 2.11: Error in $H_{rms,SS}$ predictions (*WRPE SS* shown with color bands) for (A) SWAN and (B) Xbeach as a function of F_{c0} (*x*-axis) and γ (*y*-axis). Individual color bands give *WRPE SS* for a given test condition and γ. Yellow dots give the optimum γ for each test condition. The yellow star is the optimum γ for Test no. 35 ($H_{rms,SS}$ = 0.032 m; T_p = 1.42 s; $h_{0,r}$ = 0.00 m).

The intensity of wave breaking has been related to the non-linearity parameter, F_{c0} (Gourlay 1994; Nelson 1994; Massel and Gourlay 2000; Sheremet et al. 2011):

$$F_{c0} = \frac{g^{1.25} H_{rms0}^{0.5} T_p^{2.5}}{\left(h_r + \bar{\eta}\right)^{1.75}}, \tag{2.22}$$

where T_p is the peak wave period. Based on field and laboratory data from reef profiles with near horizontal reef flats, Nelson (1994) and Gourlay (1994) proposed that F_{c0} was suitable parameter for classifying relative wave shape and wave transformation. From observations, Figure 2.8 shows that $H_{rms,SS} / (h_{0,r} + \bar{\eta})$ increases with F_{c0} for wave gauges on the fore reef (Gauge 6) and reef flat (Gauges 7 and 8). Relative wave breaking dissipation (as expressed by the energy flux ratio $F_{SS,8}/F_{SS,0}$ where $F_{SS,8}$ and $F_{SS,0}$ are the *SS* wave energy flux on the reef flat (Gauge 8) and offshore, respectively) generally increased with increased F_{c0}.

Optimal α values for SWASH and γ values for SWAN generally increase (though with some notable exceptions) with F_{c0} (Figure 2.10 and Figure 2.11). In

contrast, optimal γ values for XBeach however remain relatively constant over the range of test conditions (Figure 2.11). Figure 2.10 and Figure 2.11 show the *WRPE SS* error metric as a function of each model's key wave breaking parameter and F_{c0}, with optimal values of α and γ shown with points. For $F_{c0} < 1 \times 10^4$ SWASH had high *WRPE SS* errors for large values of α. As F_{c0} increased in the 3×10^2 to 1×10^4 range the values of α which predicted high *WRPE SS* errors increased. For $F_{c0} > 1 \times 10^4$ SWASH generally showed less sensitivity to α values. With the exception of three test conditions, optimal α values for SWASH increased with F_{c0}. Test no. 30, 31, and most notably 38 give lower than default optimal α (0.20, 0.18, and 0.39 respectively; Table 2.2). In these three scenarios the default α resulted in an over prediction of $H_{rms,SS}$ at gauges on the reef flat, lower α values were required to reduce $H_{rms,SS}$ on the reef flat. It is however unclear why the over prediction with the untuned α exists for these three scenarios, as the scenarios fit the general trend of increasing $H_{rms,SS} / (h_0 + \bar{\eta})$ with F_{c0} (Figure 2.8 A) and increased dissipation with F_{c0} (Figure 2.8 B). Overall, as depicted in Figure 2.5, we must emphasize that the SWASH results with the untuned $\alpha = 0.6$ still agree well with measurements, but further improvement was possible by this tuning of α (Table 2.2; Figure 2.7).

Over the range of F_{c0} values, for γ from 0.2 to 1 SWAN and XBeach showed contrasting regions of high *WRPE SS* (Figure 2.11). SWAN predictions gave high *WRPE SS* for $\gamma < \sim 0.5$, however XBeach predictions showed high *WRPE SS* for $\gamma > \sim 0.5$ (Figure 2.11). Also SWAN predictions showed a general increase in optimal γ values with F_{c0}, whereas this trend is not present for XBeach predictions. The differing optimal γ values and response to F_{c0} for SWAN and XBeach are believed to be due to differences in the breaking formulation discussed in Section 2.6.2.

2.7. Conclusions

In this test of three commonly used wave models (SWASH, SWAN, and XBeach), all were found to be capable of predicting *SS* wave height variations across a steep fringing reef profile with reasonable accuracy (Figure 2.5 A,D,G and Figure 2.7 A). Nevertheless, with tuning of the wave breaking parameters (α in SWASH and γ in both SWAN and XBeach) the accuracy of predictions could be further increased substantially (Table 2.2; Figure 2.6 A,D,G; Figure 2.7 A). SWASH and XBeach also predicted *IG* wave height (Figure 2.5 B,H; Figure 2.6 B,H; Figure 2.7 B) and spectral transformation into lower frequencies (Figure 2.4), albeit with higher error than for the *SS* waves. Although SWAN was capable of accurately modeling the *SS* wave heights, in

its current form it was not able to accurately model the observed spectral transformation into lower frequencies, as evident in the under prediction of *IG* waves across the reef flat (Figure 2.3-Figure 2.7). Recently Sheremet et al. (2011) showed that it is possible to accurately model spectral transformation (including *IG* waves) using a nonlinear spectral wave model with direct nonlinear triad interaction and frequency dependent wave breaking. Spectral transformation in SWAN may thus be improved by adopting some of the formulations found in Sheremet et al. (2011). The skill of either SWAN or XBeach could potentially be improved by using an alternative wave breaking dissipation formula or implementing a spatially variable γ formulation (e.g., van der Westhuysen 2010). Furthermore comparative testing needs to be conducted to look at other reef geometries and test cases that include larger more realistic bottom roughness. The accuracy of predictions of other metrics (e.g., skewness and asymmetry of velocity and acceleration), not just wave height, that are also important for predicting wave driven currents and sediment transport should also be further investigated.

Table 2.2: Summary of the 29 test conditions, tuned values of the key breaking parameter for SWASH, SWAN, and XBeach, and percent error reduction owing to model tuning (*BSS*). Negative values of *BSS* indicate a decrease in the accuracy of the tuned model predictions relative to the untuned model predictions.

					SWASH				SWAN				XBeach			
Test no.	$H_{rms,SS}$ [m]	T_p [s]	$h_{0,r}$ [m]	F_{c0} [-]	Tuned α [-]	*BSS SS* [%]	*BSS IG* [%]	*BSS* $\bar{\eta}$ [%]	Tuned γ [-]	*BSS SS* [%]	*BSS IG* [%]	*BSS* $\bar{\eta}$ [%]	Tuned γ [-]	*BSS SS* [%]	*BSS IG* [%]	*BSS* $\bar{\eta}$ [%]
15	0.04	1.0	0.05	4.8E+02	0.6	0	0	0	0.7	81	13	21	0.36	85	-47	-8
16	0.04	1.4	0.05	1.2E+03	0.85	57	-35	-5	0.64	82	-2	92	0.33	91	57	19
17	0.06	1.4	0.05	1.4E+03	1.19	57	-22	3	0.65	43	-1	19	0.35	83	-26	-14
18	0.06	2.0	0.05	2.7E+03	1.15	74	50	-19	0.64	21	0	-105	0.34	83	20	-13
19	0.06	2.6	0.05	4.6E+03	1.9	77	31	-32	0.71	49	0	-27	0.33	76	42	-19
20	0.04	1.2	0.05	8.3E+02	0.9	67	33	-7	0.66	85	-3	92	0.35	89	-105	17
21	0.06	1.8	0.05	2.0E+03	1.09	83	-8	-9	0.73	0	0	0	0.33	85	28	-6
26	0.04	1.0	0.02	2.0E+03	0.61	11	44	-26	0.63	30	-1	-9	0.24	85	-206	-136
27	0.04	1.2	0.02	3.1E+03	0.8	16	-5	-5	0.68	10	0	-2	0.27	84	-159	-71
28	0.03	1.4	0.02	4.7E+03	1	1	3	8	0.68	81	-2	43	0.27	84	-15	-47
29	0.05	1.5	0.02	4.4E+03	0.7	14	-4	-6	0.7	65	-1	66	0.34	76	-208	-68
30	0.05	1.8	0.02	6.2E+03	0.2	28	6	-8	0.65	75	-1	82	0.29	81	61	-111
31	0.06	2.0	0.02	8.1E+03	0.18	35	0	48	0.72	13	0	-36	0.35	76	59	27
32	0.06	2.6	0.02	1.3E+04	2.18	60	23	-152	0.69	4	0	-141	0.3	68	72	46
33	0.04	1.0	0.00	1.1E+04	2.5	44	-16	3	0.92	78	1	51	0.35	80	-68	-43
34	0.03	1.4	0.00	1.8E+04	3.24	87	-249	16	0.79	65	1	18	0.34	88	44	-3
35	0.03	1.4	0.00	1.8E+04	3.21	91	-115	15	0.85	72	1	40	0.33	85	28	2
36	0.05	1.5	0.00	1.3E+04	3.46	83	66	-59	0.85	44	0	42	0.35	83	-118	-175
37	0.05	1.8	0.00	1.7E+04	2.69	53	6	-372	0.83	59	0	12	0.33	84	70	66
38	0.06	2.0	0.00	2.0E+04	0.39	38	6	21	0.71	10	0	-9	0.34	79	45	20
39	0.05	2.6	0.00	3.0E+04	3.11	57	-19	-112	0.45	27	0	-1561	0.4	73	9	19
44	0.02	1.0	0.03	2.5E+02	0.65	1	4	-1	0.61	28	-2	2	0.3	72	-69	7
45	0.04	1.0	0.03	1.0E+03	1.15	18	5	-6	0.71	4	0	-12	0.34	75	-68	-9
46	0.04	1.2	0.03	1.7E+03	1.36	33	-27	-5	0.65	61	-3	92	0.34	79	-103	-13
47	0.04	1.4	0.03	2.5E+03	1.15	22	-27	0	0.66	58	-2	51	0.33	84	-3	5
48	0.05	1.4	0.03	2.6E+03	1.28	44	-34	-3	0.65	27	-2	63	0.36	76	-272	-44
57	0.05	1.8	0.03	3.6E+03	1.83	47	34	-20	0.75	15	0	3	0.35	85	0	-37
58	0.06	2.0	0.03	5.0E+03	1.5	50	5	-73	0.72	52	0	44	0.37	81	16	-28
59	0.06	2.6	0.03	8.1E+03	1.78	54	5	-20	0.72	18	0	7	0.35	74	61	-26

3. Dynamics of wave setup over a steeply-sloping fringing reef

3.1. Abstract

High-resolution observations from a 55-m long wave flume were used to investigate the dynamics of wave setup over a steeply-sloping reef profile with a bathymetry analogous to many fringing coral reefs. Sixteen runs incorporating a wide range of offshore wave conditions and still water levels were conducted using a 1:36 scaled fringing reef, with a 1:5 slope reef leading to a wide and shallow reef flat. Wave setdown and setup observations measured at seventeen locations across the fringing reef were compared with a theoretical balance between the local cross-shore pressure and wave radiation stress gradients. We found that when radiation stress gradients were calculated from observations of the radiation stress derived from linear wave theory, both wave setdown and setup were under predicted for the majority of wave and water level conditions tested. These under predictions were most pronounced for cases with larger wave heights and lower still water levels (i.e., cases with the greatest setdown and setup). Inaccuracies in the predicted setdown and setup were improved by including a wave roller model, which provides a correction to the kinetic energy predicted by linear wave theory for breaking waves and produces a spatial delay in the wave forcing that was consistent with the observations.

3.2. Introduction

Wave setup, or the increase in mean water level due to breaking waves, often represents a substantial portion of the total water depth over shallow coral reefs, and spatial gradients in setup are a primary driver of circulation (e.g., Monismith 2007; Lowe and Falter 2015). As a result, the accurate prediction of wave setup on reefs is crucial for predicting a wide range of coastal hazards, such as coastal inundation and erosion resulting from large storms (Sheppard et al. 2005; Vetter et al. 2010; Storlazzi et al. 2011; Baldock et al. 2014).

Predictions of wave setup in the surf zone are typically based on partitioning wave forces (e.g., radiation stress gradients) into either pressure gradients (associated with wave setup) or bottom stresses through conservation of the mean (wave-averaged) momentum (Longuet-Higgins and Stewart 1964). This theoretical balance is the foundation for most process-based nearshore hydrodynamic models. Wave forces in the surf zone are commonly approximated from linear wave theory, which assumes that waves are non-breaking and of a near constant form while propagating over an

effectively flat bed (Longuet-Higgins and Stewart 1962; Longuet-Higgins and Stewart 1964). Despite the violation of these assumptions in the surf zone, on mildly-sloping beaches radiation stress gradients derived from linear wave theory have often balanced observed cross-shore pressure gradients (Battjes and Stive 1985; Lentz and Raubenheimer 1999). The assumptions of linear wave theory are more questionable when applied to plunging waves on steep-slope beaches and reefs.

Despite the apparent misapplication of linear wave theory in these environments, models that predict wave forces using linear wave theory are still widely applied to steeply-sloping reefs, with many reporting that even simple models can accurately reproduce setup observations (Gourlay 1996a; Massel and Gourlay 2000; Becker et al. 2014; Buckley et al. 2014). However, in all of these studies the predicted setup was dependent on radiation stress gradients predicted using empirical or idealized models (rather than wave observations). Hence, the good agreement reported may be owing to the tuning of coefficients that may not necessarily be physically meaningful. For example, Buckley et al. (2014) reported that tuning the Simulating WAves Nearshore (SWAN) model (Booij et al. 1999) to best reproduce the observed wave height decay across a laboratory reef profile often resulted in a reduction in the accuracy of wave setup predictions, which indicates a fundamental breakdown in the theoretical relationship between the predicted radiation stress gradients and the observed wave setup. In general, the lack of detailed observational data on steeply-sloping reefs, particularly in the surf zone region, has made it very difficult to rigorously evaluate the theory used to predict wave transformation and wave setup.

In this paper we investigate the theoretical balance between cross-shore pressure and radiation stress gradients using high-resolution laboratory observations across a steeply-sloping reef profile. In particular, we assess the ability of linear wave theory derived radiation stress gradients approximated from observations to reproduce the observed setup and setdown responses. However, we also examine the contribution of a wave roller (Svendsen 1984b; Reniers and Battjes 1997; Apotsos et al. 2007) as a means of including the high onshore directed surface velocities observed in the crests of breaking waves and associated turbulent bores (e.g., Govender et al. 2002). While this study specifically focuses on a representative fringing reef, our results are also relevant to understanding the mechanisms of wave setup generation by wave breaking on steep slopes more generally. The experiments were conducted in a 55-m long flume (1:36 scale) with a 1:5 slope reef leading to a wide, shallow reef flat and sloping beach. Sixteen cases were simulated, spanning a wide range of offshore wave heights and still

water levels, over a smooth bed and then repeated with scaled bottom roughness. In this paper we focus on the smooth bed cases, to specifically focus on the surf zone processes that control the mean water level variability; a follow-up paper (Buckley et al. 2015b) will detail the effect of large bottom roughness.

3.3. Background

As our objective is to understand wave setup on a steep reef profile, we first outline the general theory and how it applies to our particular set of experiments.

3.3.1. Cross-shore mean momentum equation

For an along-shore uniform reef with normally incident waves, the wave-averaged, depth-integrated cross-shore (x-coordinate, positive shoreward from the reef crest) momentum equation can be written as (e.g., Mei 2005):

$$\frac{\partial M_T}{\partial t}+\frac{\partial}{\partial x}\left(\frac{M_T^2}{\rho(h_0+\overline{\eta})}\right)=-\rho g\left(h_0+\overline{\eta}\right)\frac{\partial \overline{\eta}}{\partial x}-\frac{\partial S_{xx}}{\partial x}-\overline{\tau}_b\sqrt{1+\left(\frac{\partial h_0}{\partial x}\right)^2}, \qquad (3.1)$$

where the overbars denote time-averaging over many wave periods, M_T is the depth-integrated and time-averaged Lagrangian mass flux, t is time, ρ is density, g is the gravitational acceleration, h_0 is still water depth, $\overline{\eta}$ is the time-averaged deviation of the free surface η from h_0, S_{xx} is the cross-shore component of the radiation stress tensor, and $\overline{\tau}_b$ is time-averaged bottom stress. In Eq. (3.1), we note that we have neglected two terms in the general form of the cross-shore momentum equation (see Mei 2005). A term containing the time-averaged dynamic pressure at the bottom, as it is considered to be of negligible magnitude compared to other terms included in Eq. (3.1), even on steep slopes (see Svendsen 2006 for discussion); and a depth-integrated viscous stress term that is negligible relative to the other terms at sufficiently high Reynolds numbers (i.e., $O(10^3) >> 1$ based on the wave orbital velocities in the present study)(Mei 2005). Due to the design of the experiment, further simplifications of Eq. (3.1) are possible. For all cases considered here, the system was in steady-state when averaged over many wave cycles (i.e., $\overline{\partial / \partial t} = 0$) and the shoreline was impermeable, such that the depth-integrated and time-averaged Lagrangian mass flux M_T was zero; thus, eliminating all terms on the left hand side (*LHS*) of Eq. (3.1). For the particular set of experiments described here, where the bottom was composed of smooth marine plywood to minimize the role of bottom roughness on setup, $\overline{\tau}_b$ was quantified to have a negligible effect on the closure of the mean momentum balance and the prediction of wave setup

(see Appendix A). Under these assumptions, Eq. (3.1) reduces to a dynamic balance between the radiation stress and pressure gradient terms:

$$\underbrace{\frac{\partial S_{xx}}{\partial x}}_{\substack{\text{radiation stress}\\ \text{gradient}}} + \underbrace{\rho g(h_0+\overline{\eta})\frac{\partial \overline{\eta}}{\partial x}}_{\substack{\text{pressure}\\ \text{gradient}}} = 0. \tag{3.2}$$

The approach used to evaluate S_{xx} is summarized briefly in Section 3.3.2.

3.3.2. Radiation stresses

The cross-shore component of the radiation stress tensor S_{xx} can be defined as (e.g., Mei 2005):

$$S_{xx} = \underbrace{\overline{\int_{-h_0}^{\eta} \left(p+\rho u^2\right) dz}}_{\substack{\text{total}\\ \text{momentum flux}}} - \underbrace{\frac{1}{2}\rho g(h_0+\overline{\eta})^2}_{\substack{\text{momentum flux}\\ \text{in the absence of waves}}}, \tag{3.3}$$

where z is the vertical coordinate (positive upwards from h_0), p (z) is pressure, and u (z) is defined as the deviation of the instantaneous velocity in the cross-shore direction from the depth- and time-averaged Lagrangian velocity. Typically when evaluating Eq. (3.3), all velocities other than wave orbital motion below $\overline{\eta}$ are neglected, the mean dynamic pressure below $\overline{\eta}$ is approximated as $-\rho\overline{w'^2}$ (where w' is the vertical component of the wave orbital velocity), and the mean dynamic pressure above $\overline{\eta}$ is approximated as being hydrostatic (Longuet-Higgins and Stewart 1964; Mei 2005; Svendsen 2006). These assumptions are violated for breaking waves, particularly plunging breakers (Battjes 1988); however, these assumptions are required for use in both practical numerical and analytical models based on Eq. (3.2). These assumptions, along with linear wave theory expressions for η and the wave orbital velocities u' and w' (where u' is the wave orbital velocity in the cross-shore direction), yield

$$S_{xx} = E\left(2\frac{c_g}{c} - \frac{1}{2}\right), \tag{3.4}$$

where E is the wave energy density (defined below), c_g is the wave group velocity, and c is the wave celerity. We note that Phillips (1977) derived an alternative S_{xx} to Eq. (3.4) based on a slightly different decomposition of the wave orbital and mean current velocities; however, as noted by Svendsen (2006) and Smith (2006), differences with Eq. (3.4) are generally small (on order of the wave steepness to the fourth power; Svendsen 2006).

From the experimental findings of Stive and Wind (1982), Govender et al. (2002), and Govender et al. (2009), as well as the three-dimensional fine-scale

numerical simulations of Torres-Freyermuth et al. (2007), it appears that the largest source of uncertainty in the evaluation of S_{xx} for surf zone waves arises from the evaluation of $\rho\overline{u^2}$, specifically the contribution of velocities in the crest of breaking waves that is neglected in Eq. (3.4). Due to the dependence of S_{xx} on wave energy density E, it is useful to show the general form of E, which is composed of both potential energy (*PE*) and kinetic energy (*KE*) as (e.g., Dean and Dalrymple 1991):

$$E = \underbrace{\frac{1}{2}\overline{\int_{-h_0}^{\eta}\left(\rho u'^2 + \rho w'^2\right)dz}}_{KE} + \underbrace{\frac{1}{2}\rho g\overline{\left(\eta-\overline{\eta}\right)^2}}_{PE}. \tag{3.5}$$

In linear wave theory and other non-breaking wave theories (e.g., cnoidal; Svendsen 2006), both *PE* and *KE* are equal (e.g., Dean and Dalrymple 1991; Dean and Bender 2006), allowing E to be approximated from observations of sea surface variance alone (a measure of *PE*, per the final term of Eq. (3.5)). However, the assumptions leading to $PE = KE$ are explicitly violated under breaking waves (Svendsen 1984b; Battjes 1988). This can have important implications from the evaluation of radiation stress gradients in the surf zone. Wave roller theory, has been introduced to account for the additional source of *KE* for breaking waves and therefore as an additional contribution to S_{xx}.

3.3.3. Wave roller theory

Detailed Particle Image Velocimetry (PIV) measurements of plunging waves (Govender et al. 2002) have shown much larger velocities in the crest region relative to non-breaking waves. In the surf zone, this can locally result in *KE* > *PE* (e.g., Iwata and Tomita 1992). In wave roller theory (Duncan 1981; Svendsen 1984b), some fraction of a breaking wave is partitioned into a wave roller with increased *KE* and shoreward mass flux. The wave roller is modeled independently of S_{xx} (similar to the approach of Apotsos et al. 2007) and does not contribute to η, but simply modifies *KE* resulting as an additional source of radiation stress R_{xx} according to (Svendsen 1984b)

$$R_{xx} = 2E_r, \tag{3.6}$$

where E_r is the kinetic energy of the wave roller modeled using an approximate energy balance following Stive and De Vriend (1994),

$$\frac{\partial}{\partial x}\left(2E_r c\right) = D_{br} - \overline{\tau}_t c, \tag{3.7}$$

where D_{br} is wave breaking dissipation and $\overline{\tau}_t$ is the mean shear stress at the boundary between the turbulent wave roller and the underlying organized wave motion. Conceptually, wave roller theory implies that *PE* is initially transferred to *KE* during

wave breaking and *KE* is dissipated via shear stresses (i.e., momentum exchange). The mean shear stress $\overline{\tau}_t$ is approximated as (Dally and Brown 1995):

$$\overline{\tau}_t = \frac{2gE_r}{c^2}\beta_D, \tag{3.8}$$

where $\beta_D = \sin\theta_r \cos\theta_r$ is a dissipation coefficient that depends on the angle θ_r of inclination of the boundary between the turbulent wave roller and the underlying organized wave motion (Dally and Brown 1995). This dissipation mechanism implies a slowly changing wave shape, i.e. a quasi- "steady" breaking process (Dally and Brown 1995) that may not develop in the initial overturning stage of plunging wave breaking. However, the plunging distance, which is generally less than the breaking wave height (Bowen et al. 1968; Grilli et al. 1997), is very small relative to the total surf zone width such that steady bores are usually observed to develop even for initially plunging waves (Okayasu et al. 1986; Bonmarin 1989). Furthermore, despite the decrease in *PE* in the plunging region, pressure gradients have been found to be small (e.g., Bowen et al. 1968) indicating that this region is less important for setup generation than the decrease in *PE* would suggest (Svendsen 1984b). Thus, with turbulent bores propagating over much of the total surf zone region, the basic assumptions of the wave roller dissipation model can still hold, although we evaluate this in detail using the observations below.

3.4. Methods

3.4.1. Experimental setup

Experiments were performed in a 55-m long wave flume (Eastern Scheldt Flume) at Deltares, the Netherlands (Figure 3.1). The reef profile was constructed from marine plywood and had a 1:5 reef slope, a 14 m horizontal reef flat and a 1:12 beach (Figure 3.1). Based on the 1:36 geometric scaling assumed in this study, this represents a 500-m long reef flat in field (prototype) scale that is comparable to the global median coral reef flat length of 450 m reported by Falter et al. (2013). Published reef slopes vary from being relatively mild (e.g., ~1:60 Kaneohe Bay, Hawaii; Lowe et al. 2009b) to nearly vertical (e.g., Gourlay 1996a). A 1:5 slope was chosen to be representative of the steeper range of natural reef slopes, yet still well within the typical range.

Table 3.1: Simulated wave and water level conditions including the deep water *rms* wave height ($H_{rms,0}$), the peak period (T_p), the still water depth on the reef flat ($h_{0,r}$), the deep water wave steepness ($H_{rms,0}/L_0$), and the deep water surf similarity parameter (ξ_0). Parameter values are given for both the laboratory scale (1:36 geometric scaling and 1:6 scaling of time) and the equivalent field scale.

	Lab scale			Field scale				
	$H_{rms,0}$	T_p	$h_{0,r}$	$H_{rms,0}$	T_p	$h_{0,r}$	$H_{rms,0}/L_0$	ξ_0
Run	[m]	[s]	[m]	[m]	[s]	[m]	[-]	[-]
1	0.03	2.26	0.04	1.1	13.6	1.4	0.004	3.3
2	0.06	2.26	0.04	2.2	13.6	1.4	0.007	2.4
3	0.09	2.26	0.04	3.2	13.6	1.4	0.011	1.9
4	0.12	2.26	0.04	4.3	13.6	1.4	0.015	1.7
5	0.14	2.26	0.04	5.0	13.6	1.4	0.018	1.5
6	0.17	2.26	0.04	6.1	13.6	1.4	0.021	1.4
7	0.06	1.31	0.04	2.2	7.9	1.4	0.021	1.4
8	0.06	3.20	0.04	2.2	19.2	1.4	0.004	3.4
9	0.06	2.26	0.00	2.2	13.6	0.0	0.009	2.2
10	0.06	2.26	0.02	2.2	13.6	0.7	0.009	2.2
11	0.06	2.26	0.06	2.2	13.6	2.2	0.008	2.3
12	0.06	2.26	0.09	2.2	13.6	3.2	0.008	2.3
13	0.12	2.26	0.00	4.3	13.6	0.0	0.015	1.7
14	0.12	2.26	0.02	4.3	13.6	0.7	0.015	1.7
15	0.12	2.26	0.06	4.3	13.6	2.2	0.015	1.7
16	0.12	2.26	0.09	4.3	13.6	3.2	0.015	1.6

Waves were generated with a piston-type wave maker with second-order wave generation and active reflection compensation of any seaward-propagating waves reflected back to the wave maker from the reef slope and beach (van Dongeren et al. 2002). Irregular waves were generated with a TMA type spectrum (Bouws et al. 1985). A total of sixteen runs were conducted with varying still water depths on the reef flat $h_{0,r}$ and offshore wave conditions (Table 3.1). Wave periods, and time scales in general, are scaled by matching the Froude number, which ensures that gravity forces are correctly scaled and yields a time scaling factor of 1:6. The surf similarity parameter $\left(\xi_0 = \beta / \sqrt{H_{rms,0} / L_0}\right)$ can provide an estimate of how waves should break on the reef slope (Battjes 1974), where β = 1/5 is the reef slope, $H_{rms,0}$ is the deep water root mean square (*rms*) wave height $H_{rms} = \sqrt{8\overline{(\eta - \overline{\eta})^2}}$, and L_0 is the deep water wave length. Waves in this study were typically plunging, as predicted by ξ_0 (plunging regime of $0.5 \leq \xi_0 \leq 3.3$) (Table 3.1) (Battjes 1974).

Water levels were measured using resistance wave gauges (GHM, Deltares) sampling synchronously at 40 Hz at seventeen locations, with the highest density of measurements in the surf zone region near the reef crest at x = 0 m (Figure 3.1). Horizontal velocities were also measured synchronously at 40 Hz using electromagnetic

current meters (P-EMS, Deltares) at six locations collocated with wave gauges (Figure 3.1). On the reef flat and reef slope, the GHMs and P-EMSs were recessed into the bed in order to be able to sample in the shallow depths (Eslami Arab et al. 2012); the P-EMSs at these locations sampled velocity at a height 2 cm above the bed, with the sample volume extending 0.5 cm above the sensor. P-EMSs at other offshore locations sampled at approximately the middle of the water column.

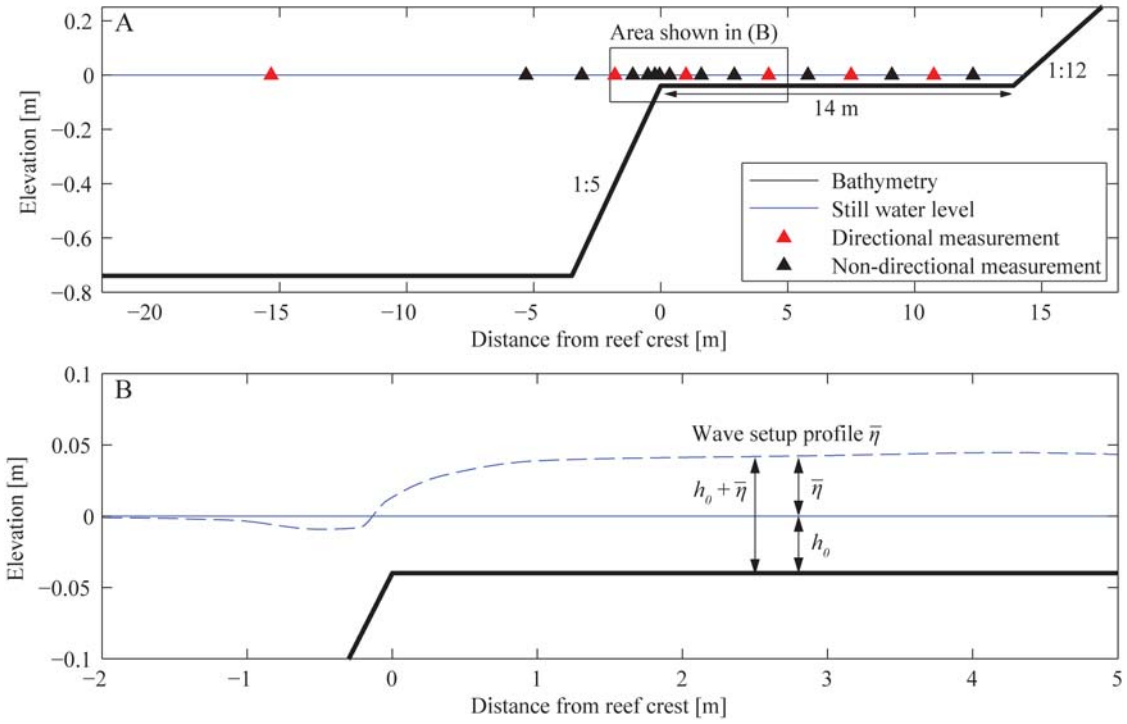

Figure 3.1: (A) Schematic of the fringing reef showing the reef slope (1:5), reef flat length (14 m; ~500 m field scale), beach slope (1:12), and instrument locations. "Directional" measurement sites have co-located water level and velocity measurements, whereas other "non-directional" sites have only water level measurements. Many of the subsequent figures will focus on the area in the vicinity of the reef crest (black box) where radiation stress gradients and pressure gradients were the largest. (B) An example of the wave setup profile ($\bar{\eta}$) in the vicinity of the reef crest for Run 4, defining the still water depth (h_0) and the total water depth ($h_0+\bar{\eta}$).

3.4.2. Evaluation of the mean momentum equation

Wave motions in the flume can in general be composed of both shoreward and seaward propagating components. As the evaluation of S_{xx} gradients is sensitive to the direction of wave propagation, a directional wave analysis was performed using a frequency domain algorithm (Appendix B), which required synchronous water level and velocity time series. This analysis yielded predictions of the shoreward ($^+$) and seaward ($^-$) propagating components of the instantaneous water level signal at instrument locations with co-located water level and velocity measurements (i.e., "directional" sites), other sites with only water level measurements are referred to as "non-

directional" sites (Figure 3.1). Wave spectra $C_{\eta\eta}$, as well as shoreward $C^{+}_{\eta\eta}$ and seaward $C^{-}_{\eta\eta}$ components (at directional sites), were computed from water level measurements using Welch's modified periodogram method with a Hanning window and a segment length of 2^{14} samples (410 s; 41 min in field scale). From $C^{+}_{\eta\eta}$ the radiation stress S_{xx} for a frequency-spread (i.e., random) wave field can be approximated using linear wave theory as (Battjes 1972):

$$S_{xx} = \int \rho g C^{+}_{\eta\eta} \left(2\frac{c_g}{c} - \frac{1}{2} \right) df, \tag{3.9}$$

where c_g (f) and c (f) are the group and phase velocities, respectively, at frequency f. Eq. (3.9) is the equivalent spectral form of Eq. (3.4). As the evaluation of Eq. (3.9) requires directional information not available at all locations, directional information was interpolated to the non-directional sites using linear wave energy flux (i.e., $F = c_g E$) of which the shoreward component of F^{+} is related to S_{xx} as:

$$S_{xx} = \frac{F^{+}}{c_g} \left(2\frac{c_g}{c} - \frac{1}{2} \right). \tag{3.10}$$

The non-directional linear wave energy flux F was calculated at all instrument sites from $C_{\eta\eta}$ as:

$$F = \int c_g \rho g C_{\eta\eta}\, df. \tag{3.11}$$

The definition $F^{+} = F - F^{-}$ was used to evaluate F^{+} from the computed F (Eq. (3.11)) and the seaward component F^{-}, which was computed at directional sites (via Eq. (3.11) using $C^{-}_{\eta\eta}$ rather than $C_{\eta\eta}$) and then linearly interpolated to adjacent non-directional sites. The seaward component F^{-} was used for the interpolation as it is independent of wave shoaling and less dependent on breaking dissipation than F^{+}. Furthermore, in the evaluation of Eq. (3.10) and (3.11), we distinguished between "sea-swell" (*SS*) defined as $f \geq f_p/2$, where f_p is the peak forcing frequency of each wave case, and "infragravity" (*IG*) defined as $0.025 \leq f < f_p/2$ components. This allowed S_{xx} to be evaluated at every instrument using Eq. (3.10) as:

$$S_{xx} = S_{xx,SS} + S_{xx,IG} = \frac{F^{+}_{SS}}{c_g(\overline{f}_{SS})} \left(2\frac{c_g(f_{SS,mean})}{c(f_{SS,mean})} - \frac{1}{2} \right) + \frac{F^{+}_{IG}}{c_g(\overline{f}_{IG})} \left(2\frac{c_g(f_{IG,mean})}{c(f_{IG,mean})} - \frac{1}{2} \right), \tag{3.12}$$

where $S_{xx,SS}$ and $S_{xx,IG}$ are the *SS* and *IG* components of radiation stress, respectively, $\overline{f}_{SS}$ and $\overline{f}_{IG}$ are the mean frequencies for the *SS* and *IG* waves, respectively, and

F_{SS}^{+} and F_{IG}^{+} are the *SS* and *IG* components of the shoreward wave energy flux, respectively. The use of mean frequencies in Eq. (3.12) (versus computing S_{xx} spectrally from Eq. (3.9)) introduces the assumption that *SS* and *IG* components were narrow banded (see Feddersen 2004 for discussion); however, comparisons with the full spectral integration Eq. (3.9) at directional sites showed minimal differences in the values of S_{xx} estimated from Eq. (3.12).

The cross-shore gradients required to estimate the pressure and radiation stress gradients were evaluated by interpolating the observations of $\overline{\eta}$, $f_{SS,mean}$, $f_{IG,mean}$, F_{SS}^{+}, and F_{IG}^{+} using a shape-preserving piecewise cubic algorithm onto a uniform 0.01 m grid extending from offshore (x = -2.0 m) to near the shoreline (x = 14 m). Over this domain, the cross-shore distance between wave gauges varied from 0.19 m in the surf zone to 1.7 m on the reef flat (Figure 3.1). This spacing is equivalent to as low as ~1/40 of the incident wave length in the surf zone to ~1/4 on the reef flat. Cross-shore gradients were computed using central differencing and cross-shore integration was done using trapezoidal integration. At each grid location, S_{xx} was evaluated from $f_{SS,mean}$, $f_{IG,mean}$, F_{SS}^{+}, and F_{IG}^{+} using Eq. (3.12). Similarly, R_{xx} was evaluated from $f_{SS,mean}$, F_{SS}^{+}, and F_{IG}^{+} using Eq. (3.6)-(3.8) and a simple forward integration scheme. The growth term in the wave roller model Eq. (3.7) is equivalent to the breaking wave energy dissipation, calculated as $D_{br} = -\partial(F_{SS}^{+} + F_{IG}^{+})/\partial x$. As the wave roller is predominantly associated with *SS* waves, wave celerity in Eq. (3.7) and (3.8) was taken as $c(f_{SS,mean})$. In Section 3.5.3, we evaluate how the results respond to different values of β_D (related to the wave roller slope) in the wave roller dissipation formula Eq. (3.8) and also compare these values with wave gauge estimates of the wave front inclination angle. In this study, β_D = 0.19 was found to be optimum (see Section 3.5.3) and is used by default throughout the paper.

The cross-shore mean momentum balance Eq. (3.2) was rearranged and integrated in the cross-shore direction to give a "prediction" of the setup $\overline{\eta}_{pred}$ across the reef as (e.g., Raubenheimer et al. 2001):

$$\overline{\eta}_{pred} = -\int_{x_0}^{x} \frac{1}{\rho g(h_0 + \overline{\eta}_{pred})} \frac{\partial(S_{xx} + R_{xx})}{\partial x} dx + \overline{\eta}(x_0), \qquad (3.13)$$

where the integration is initialized at a seaward boundary x_0 (x_0 = -2 m in Figure 3.1) with the observed time-averaged water level $\overline{\eta}(x_0)$ ($\overline{\eta}(x_0) = 0$ if x_0 is in deep water)

and evaluated iteratively. Eq. (3.13) was evaluated with S_{xx} and R_{xx} approximated from the interpolated observations and used to evaluate the skill of S_{xx} and R_{xx} to reproduce observations of $\overline{\eta}$. Lastly, Eq. (3.2) was also used to provide an estimate of the radiation stress $S_{xx,eff}$ required to balance the observed $\overline{\eta}$ as (e.g., Svendsen and Putrevu 1993):

$$S_{xx,eff} = -\int_{x_0}^{x} \rho g(h_0 + \overline{\eta}) \frac{\partial \overline{\eta}}{\partial x} dx + S_{xx}(x_0) + R_{xx}(x_0), \tag{3.14}$$

where S_{xx} (x_0) and R_{xx} (x_0) are the initial values of S_{xx} and R_{xx}, respectively, at the offshore boundary of integration (R_{xx} (x_0) = 0 if x_0 is outside of the surf zone).

3.4.3. Uncertainty estimation

Measurement uncertainties for the GHM and P-EMS are small; calibration confirmed a maximum error of ± 0.5% of the measured range for water levels and ± 0.01 m s^{-1} ± 1% of measured values for velocity (Deltares). At surf zone locations these instruments can be expected to be less accurate due to aeration of the water column during wave breaking (e.g., Stive and Wind 1982). By comparing similar wave gauges with video analysis, Stive and Wind (1982) give a conservative estimate of the uncertainty due to aeration effects of ± 1% of the measured range for time-averaged water levels and ± 2.5% for the measurement of wave heights. Combining uncertainties due to calibration and aeration effects gave ± ~0.5% outside of the surf zone and ± ~1.5% within the surf zone of the measured range for time-averaged water levels. Likewise, the uncertainties for parameters proportional to wave height squared (i.e., wave energy and radiation stress) were ± ~2% outside of the surf zone and ± ~7% inside the surf zone. The effect of these uncertainties on the cross-shore integration of Eq. (3.13) and (3.14) was assessed by performing 100 Monte Carlo simulations, were uncertainties were modelled as having zero-mean Gaussian random distributions with a standard deviation based on the uncertainty. Velocity measurements were only used for estimating the effect of wave reflection (Appendix B), which we show below, has a minor effect on the calculated radiation stress gradients and as such is not considered a large factor in the uncertainty estimates.

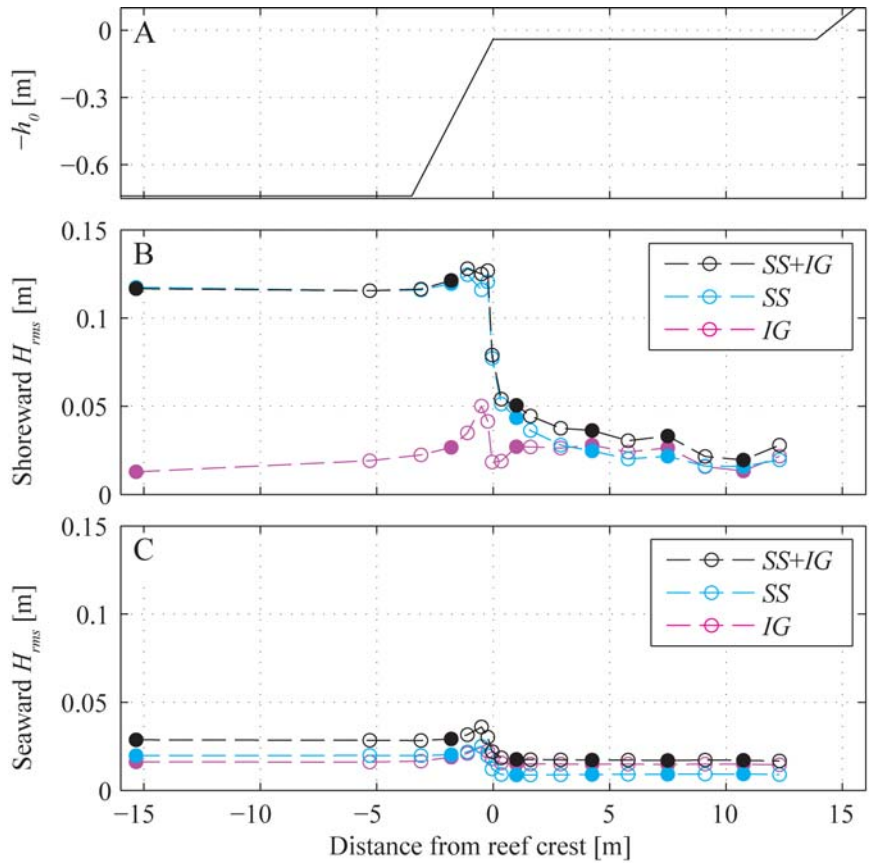

Figure 3.2: (A) The bathymetric profile (h_0), (B) the shoreward propagating component of *rms* wave height, and (C) the seaward propagating component of *rms* wave height are shown for Run 4. In each subplot the total (*SS*+*IG*), sea-swell (*SS*), and infragravity (*IG*) components are shown. In (B) and (C), closed circles are direct estimates of the shoreward and seaward components (i.e., locations with water level and velocity data), while open circles rely on interpolation of the seaward component as described in Section 3.4.2.

3.5. Results

3.5.1. Wave transformation

To illustrate the general features of wave transformation across the reef, we initially focus on results from Run 4 with moderately large wave conditions ($H_{rms,0}$ = 0.12 m, T_p = 2.26 s; or equivalent to $H_{rms,0}$ = 4.3 m, T_p = 13.6 s in field scale) with an intermediate still water depth (h_r = 0.04 m; or h_r = 1.4 m in field scale) (Figure 3.2). This run is used to highlight many of the common trends observed within the full array of runs, which differed primarily in terms of the magnitude of the wave height and setup responses. Figure 3.2 shows a rapid reduction in *SS rms* wave height in the vicinity of the reef crest (x = 0 m) associated with depth-induced breaking. A video sequence of a typical wave plunging near the reef crest is also depicted in Figure 3.3. A comparison with the shoreward component of the total wave height (*SS*+*IG*) shows that the *IG* waves contributed little to the total surf zone wave height gradients, despite *SS* and *IG rms* wave heights being comparable on the reef flat (Figure 3.2B). Wave

reflection was small relative to wave breaking dissipation (Figure 3.2C), with only 3% of *SS* and 6% of the total (*SS+IG*) wave energy flux reflected for Run 4 (values were of similar magnitude for the other runs) (Appendix B).

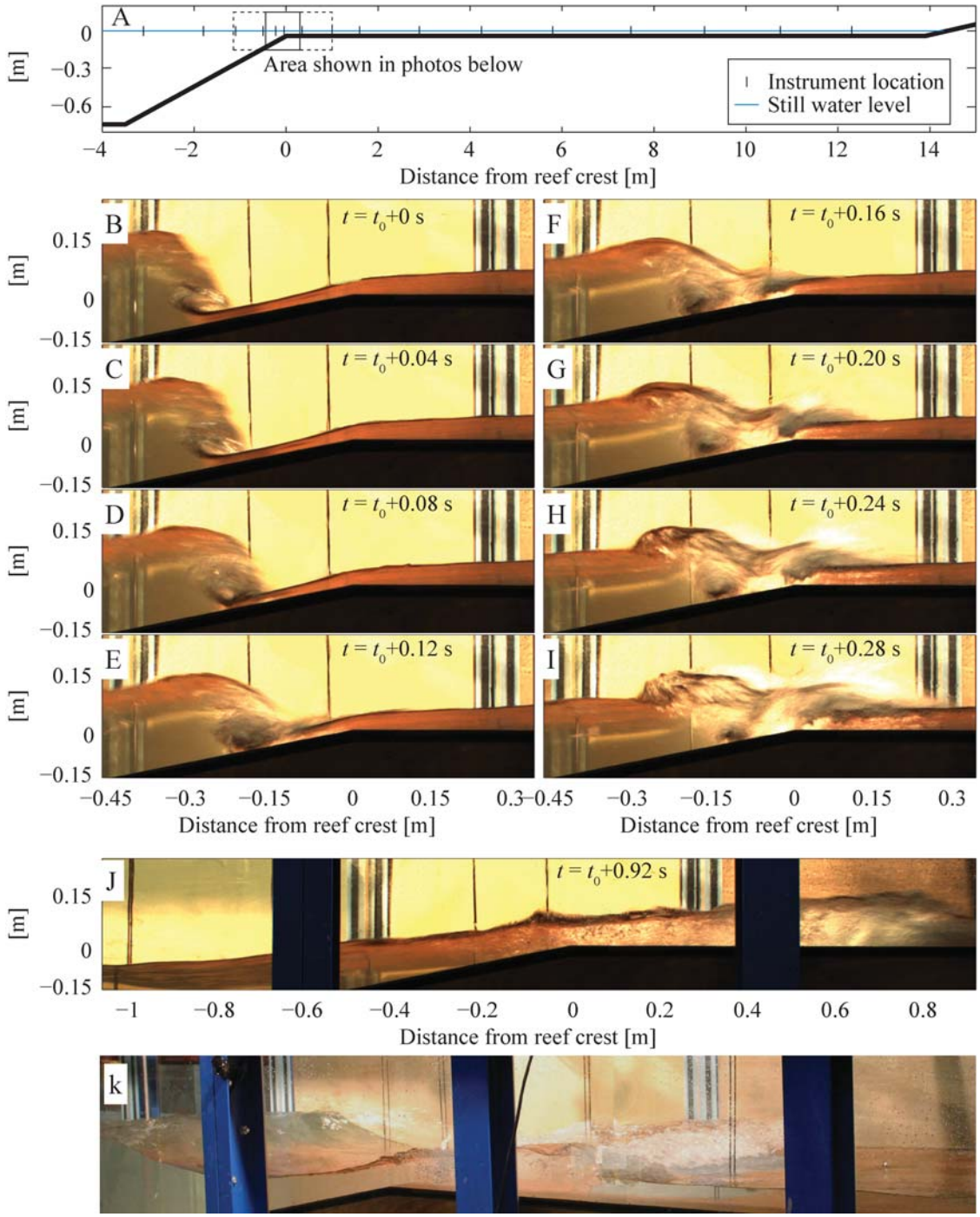

Figure 3.3: (B-I) Wave plunging sequence taken during Run 4 in the immediate vicinity of the reef crest (solid box in subplot A). In subplots B-J the notation t_0 denotes the start of the breaking sequence with a frame rate of ~25 Hz. The area of the photos is where the most intense wave breaking occurred and only covers a small portion of the total reef slope and reef flat shown in (A). (J) Larger area (subplot A dashed box) showing the development of a steady bore at x = 0.8 m propagating shoreward on the reef flat. (K) Oblique photograph showing a bore on the reef flat and a wave steepening on the reef slope.

3.5.2. Radiation stresses, momentum balances, and setup/setdown

The shoreward propagating *SS* and *IG* wave energy fluxes F^+ (Figure 3.4B) were used to evaluate the radiation stress from linear wave theory S_{xx} via Eq. (3.12) and a contribution from the wave roller R_{xx} via Eq. (3.6) (Figure 3.4C). These radiation stresses were used to predict wave setup profile via Eq. (3.13) and compared with the observations (Figure 3.4D). The inclusion of the wave roller improved the predictions of both setdown and setup by introducing a spatial delay between the dissipation of *PE* and the associated radiation stress (S_{xx}+R_{xx}) gradients (Figure 3.4D). The improved agreement was most noticeable on the seaward portion of the reef flat where $\overline{\eta}$ and $\overline{\eta}_{pred}$ calculated from S_{xx}+R_{xx} gradients continue to increase despite $\overline{\eta}_{pred}$ calculated without the wave roller reaching an approximate maximum at x = 0.35 m (Figure 3.4D). However, comparing S_{xx}+R_{xx} with $S_{xx,eff}$ (i.e. the latter reflecting the S_{xx} needed to produce the observed setup per Eq. (3.14)) shows that in order to match the observed wave setup, S_{xx}+R_{xx} would still need to be slightly larger during the initial wave setdown and decay slightly more slowly shoreward of the reef crest (Figure 3.4C). However, these discrepancies only represent a very minor correction of 3-5% to the wave setup predicted from S_{xx}+R_{xx} on the reef flat (Figure 3.4D). Figure 3.5 provides two additional examples of S_{xx} and $\overline{\eta}$ profiles for Runs 13 and 16 (also discussed further below), these runs had the same incident wave forcing as Run 4 but with $h_{0,r}$ of 0 m and 0.09 m, respectively.

Of particular interest is the setup on the reef flat that establishes the water level that will interact with a shoreline. The setup was relatively constant across the majority of the reef flat (x > 4 m, Figure 3.4D, Figure 3.5B, Figure 3.5D) for all sixteen runs, allowing us to define a mean reef setup $\overline{\eta}_r$, between x = 4-10 m. To assess how offshore wave properties and still water levels influenced $\overline{\eta}_r$, we compare $\overline{\eta}_r$ with the cross-shore integrated radiation stress gradient:

$$-\int_{x_0}^{x} \frac{\partial\left(S_{xx}+R_{xx}\right)}{\partial x}dx \equiv -\Delta\left(S_{xx}+R_{xx}\right), \tag{3.15}$$

where the bounds of integration were taken from seaward of the break point (x = -2 m) to a point on the reef flat (x = 4 m) shoreward of the surf zone where $\overline{\eta}$ becomes relatively constant (i.e., $\overline{\eta} \approx \overline{\eta}_r$). As these bounds of integration are both outside of the surf zone, this evaluation is independent of whether the wave roller is considered or not (i.e., -Δ(S_{xx}+R_{xx}) = -ΔS_{xx} depends only on the end-point values of S_{xx}). For runs with

constant T_p and $h_{0,r}$ (Runs 1-6, Table 3.1), $\bar{\eta}_r$ displays a sublinear dependence on -ΔS_{xx} (Figure 3.6). This is consistent with Eq. (3.13), where $\bar{\eta}$ becomes an increasing proportion of $h_0 + \bar{\eta}$ as -ΔS_{xx} increases. For a given range of -ΔS_{xx}, variations in $h_{0,r}$ had a large influence on $\bar{\eta}_r$ (Figure 3.6; both Runs 2,8-12 and 4,13-16), with decreases in $h_{0,r}$ causing $\bar{\eta}_r$ to increase. For example $\bar{\eta}_r$ was ~2.5 times greater for Run 13 ($h_{0,r}$ = 0 m) than Run 16 ($h_{0,r}$ = 0.09 m) despite having a comparable -ΔS_{xx} (Figure 3.5, Figure 3.6).

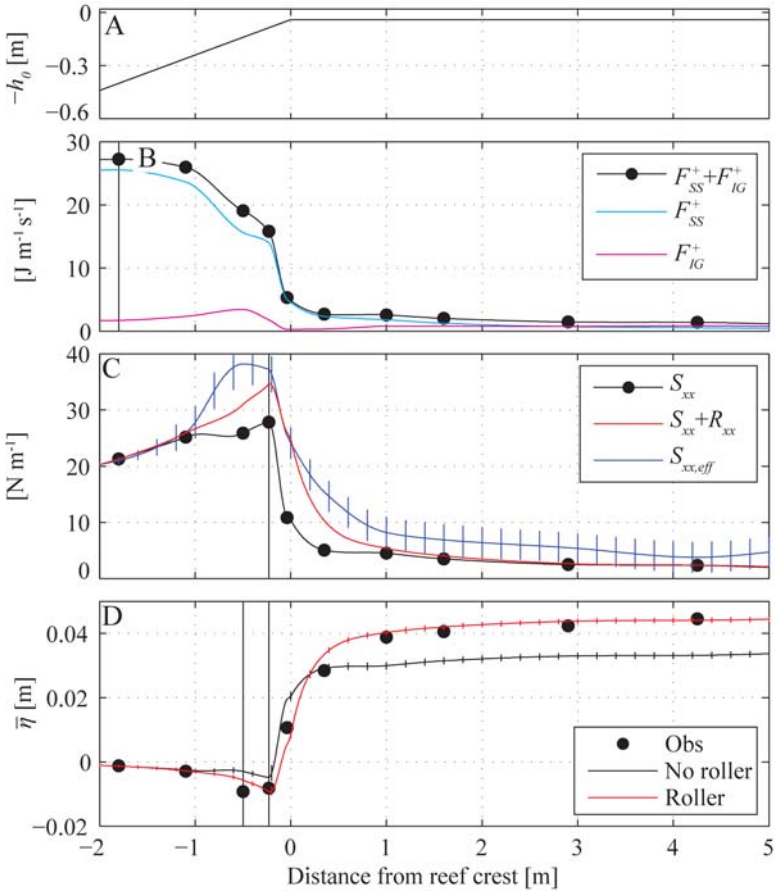

Figure 3.4: (A) The bathymetric profile (h_0)and (B) the shoreward propagating components of the wave energy flux (F^+) are shown in the vicinity of the reef crest for Run 4 (black box in Figure 3.1A). Subscripts *SS* and *IG* denote sea-swell and infagravity, respectively. (C) The radiation stresses S_{xx} and R_{xx} are the contribution from linear wave theory Eq.(3.12) and the wave roller Eq. (3.6), respectively. The "effective" radiation stress ($S_{xx,eff}$) is the radiation stress needed to close the mean momentum equation via Eq. (3.14). (D) Radiation stresses S_{xx} ("No roller") and $S_{xx}+R_{xx}$ ("Roller") were used to evaluate $\bar{\eta}_{pred}$ via Eq. (3.13) and compared with observations "Obs". Vertical error bars are given for $S_{xx,eff}$ and $\bar{\eta}_{pred}$ (see Section 3.4.3). Vertical black lines give:(B) the start of wave dissipation and hence wave roller growth, (C) maximum S_{xx}, and (D) the region of maximum setdown.

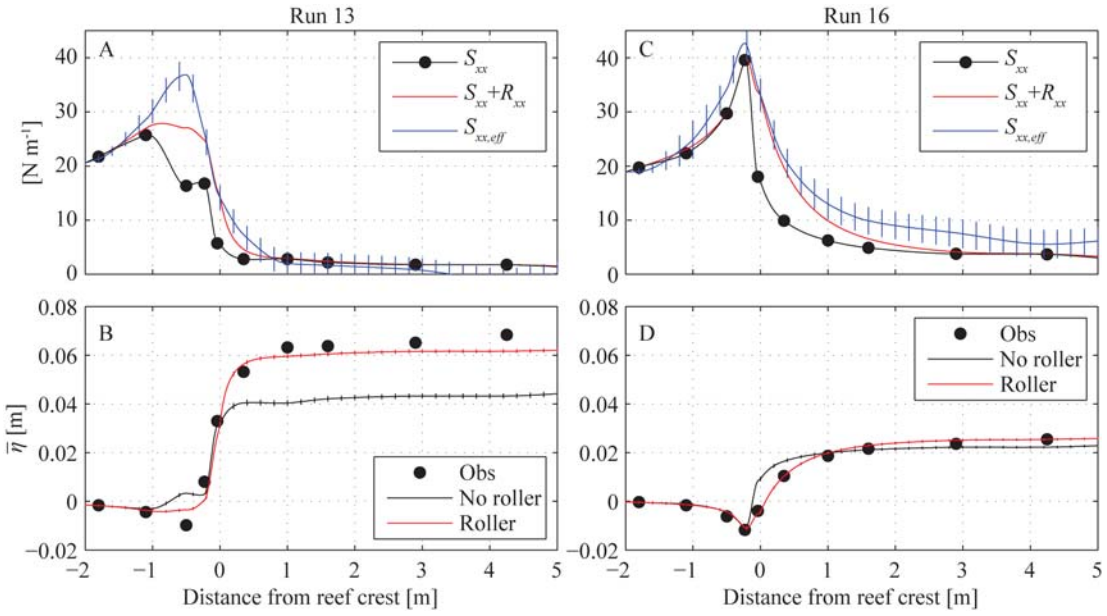

Figure 3.5: (A,C) Radiation stresses S_{xx} ("No roller") and $S_{xx}+R_{xx}$ ("Roller") were used to evaluate (B,D) $\overline{\eta}_{pred}$ via Eq. (3.13) and compared with observations "Obs" in the vicinity of the reef crest for Run 13 (first column) and Run 16 (second column). Vertical error bars are given for $S_{xx,eff}$ and $\overline{\eta}_{pred}$ (see Section 3.4.3).

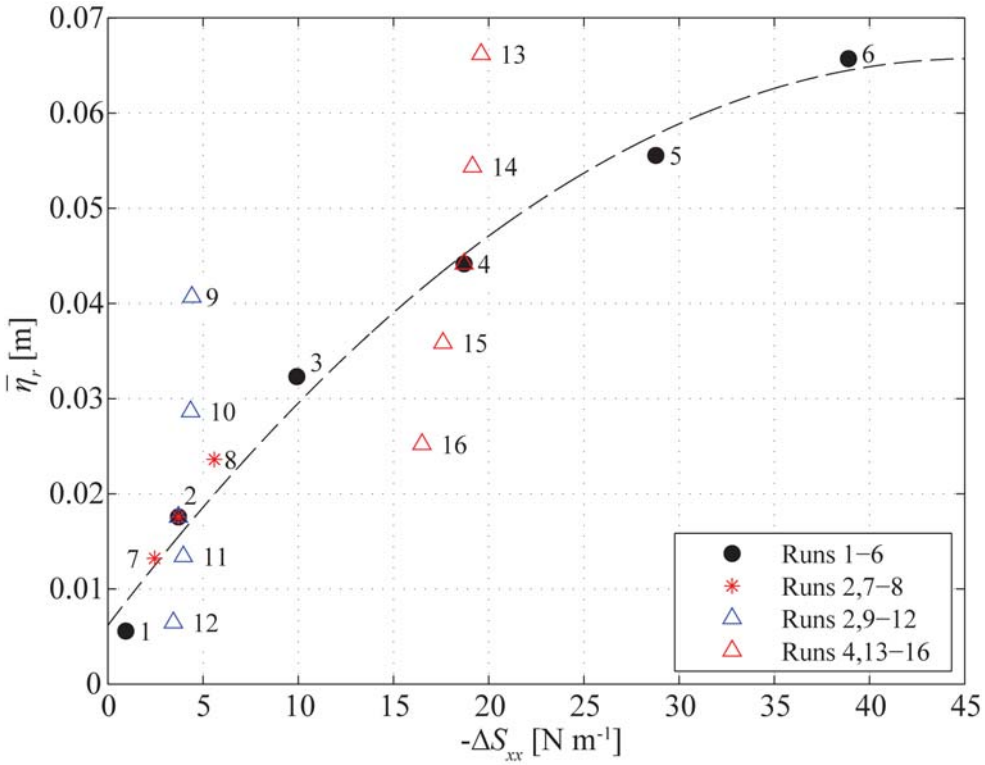

Figure 3.6: Variation of $\overline{\eta}_r$ with -ΔS_{xx} calculated from offshore to x = 4 m. Symbols denote runs with shared conditions and a single variable changed. A quadratic, least-squares trend line is given of Runs 1-6. Numbers adjacent to symbols denote the run number (refer to Table 3.1).

If the cross-shore integrated pressure gradient ($\int \rho g(h_0+\overline{\eta})\frac{\partial \overline{\eta}}{\partial x}dx$) is instead considered (rather than $\overline{\eta}_r$; Figure 3.7), this mostly collapses the trends observed in Figure 3.6. Eq. (3.2) predicts a 1:1 relationship should occur between the cross-shore integrated pressure gradient and $-\Delta S_{xx}$. Our results indicate that the trend is mostly 1:1, with nearly all runs falling within the uncertainty of the measurements (Figure 3.7).

Cross-shore integration over the entire surf zone, as done in Figure 3.7, incorporates the cumulative effects of processes that contribute to both setdown $\left(\partial \overline{\eta}/\partial x<0\right)$ and setup $\left(\partial \overline{\eta}/\partial x>0\right)$. To investigate the dynamics of setdown and setup in more detail, we cross-shore integrated Eq. (3.2) over two separate regions (Figure 3.8): 1) a region of setdown from offshore (x = -2 m) to a "transition point", defined as the point of maximum setdown (usually x = -0.5 to -0.2 m); and 2) a region of setup from the transition point to x = 4 m where $\overline{\eta}$ becomes relatively constant. We note that this transition point of maximum setdown is also used by Svendsen (1984b) to define the transition between the "outer surf zone" and the "inner surf zone", where the outer surf zone is characterized by rapid wave transformation (but comparatively small pressure gradients) and the inner surf zone is characterized by the development of steady turbulent bores and rapid wave setup generation. As the transition point is often within the surf zone (defined by $D_{br} > 0$), $-\Delta(S_{xx}+R_{xx})$ is sensitive to the inclusion of the wave roller. For the setdown region (Figure 3.8A), 11 of the 16 runs had much more negative cross-shore integrated pressure gradients than $-\Delta S_{xx}$ would predict via Eq. (3.2) . This is consistent with the under prediction of setdown shown for Runs 4 and 13 without the wave roller (Figure 3.4D, Figure 3.5B). Conversely, for the wave setup region (Figure 3.8C), 10 of the 16 runs had larger cross-shore integrated pressure gradients than $-\Delta S_{xx}$, consistent with the under prediction of setup shown for Runs 4 and 13 (Figure 3.4D, Figure 3.5B). Together with Eq. (3.2), these results suggest that the actual radiation stresses at the transition point were larger than calculated from observations via the linear wave theory approximation of radiation stress Eq. (3.12). However, as seen in the prediction of setdown/ setup profiles (Figure 3.4D, Figure 3.5B, Figure 3.5D), including the contribution from the wave roller R_{xx} (i.e., $-\Delta(S_{xx}+R_{xx})$ rather than $-\Delta S_{xx}$) substantially improved the agreement between the cross-shore integrated radiation stress and pressure gradients over both the setdown (Figure 3.8B) and setup regions (Figure 3.8D).

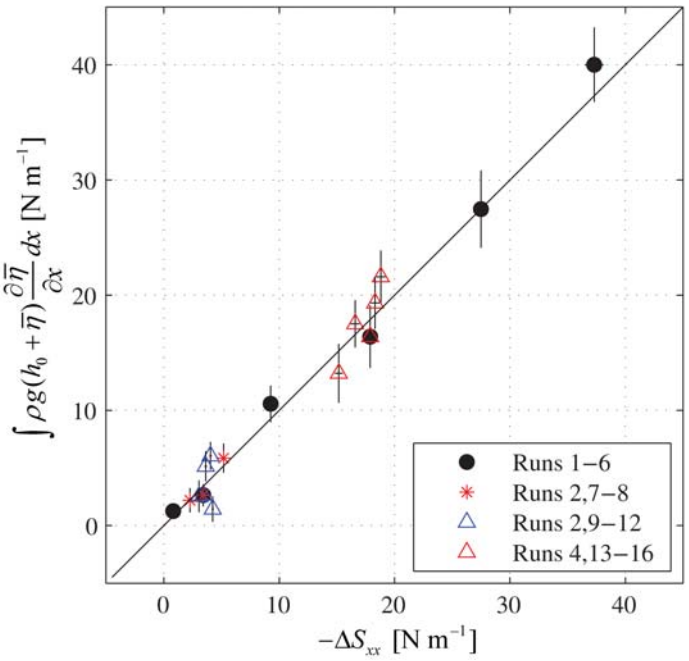

Figure 3.7: Variation of the cross-shore integrated (x = -2 to 4 m) pressure gradient with the cross-shore integrated radiation stress gradient (-ΔS_{xx}; Eq. (3.15)) for the sixteen wave and water level conditions. As the cross-shore integration spans the entire surf zone, this analysis is independent of the wave roller (i.e., -$\Delta(S_{xx}+R_{xx})$= -ΔS_{xx}). The mean momentum equation Eq. (3.2) predicts a 1:1 relationship (black line) should exist. Vertical and horizontal (typically not visible) error bars show the uncertainties due to instrument accuracy (see Section 3.4.3).

Due to these momentum balances, both wave setdown and setup were under predicted for many runs using S_{xx} alone (Figure 3.9). For setdown, 8 of the 16 runs were under predicted by an average of 49%; this under prediction was approximately halved (26%) with the inclusion of the wave roller (i.e., S_{xx}+R_{xx}). For setup, 12 of the 16 runs were under predicted by an average of 21%; inclusion of the wave roller reduced the error to just 3%. The under prediction of setdown and setup, without the inclusion of the wave roller, was most pronounced for runs with larger wave heights and lower still water levels (i.e., cases with the greatest setdown and setup). These runs also had relatively low ξ_0 values due to the dependence on offshore wave height. For the full array of runs, the improvement found by including the wave roller was substantial for $\xi_0 < 2.3$; however, for the five runs with $\xi_0 \geq 2.3$ (Table 3.1) both the setdown and setup predictions were not significantly improved with inclusion of the wave roller. Run 8 (Figure 3.9 A,B; cyan circle) was the most extreme example with $\xi_0 = 3.4$ (Table 3.1), for which a surging breaker type is predicted (Battjes 1974). For this particular run, the predicted wave setdown was considerably larger than observed (Figure 3.9A). Run 8 was also the only run where the predicted setup was substantially less accurate when including the wave roller (Figure 3.9B).

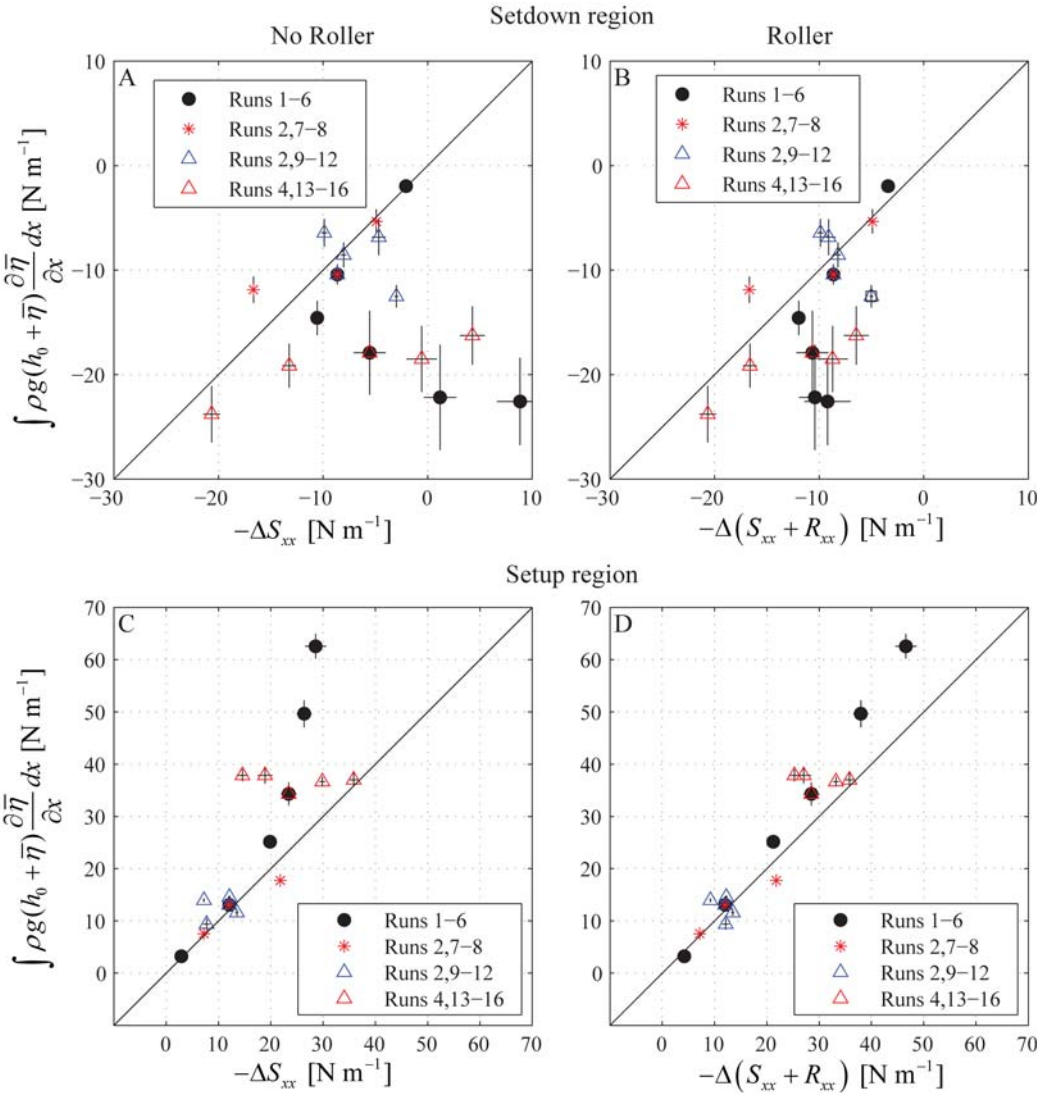

Figure 3.8: Variation of the pressure and radiation stress gradients cross-shore integrated from offshore (x = -2 m) to maximum setdown (first row; A,B) and from maximum setdown to shoreward of the surf zone (x = 4 m) (second row; C,D). The radiation stress gradients were evaluated without ($-\Delta S_{xx}$) (first column) and with ($-\Delta(S_{xx} + R_{xx})$) (second column) the wave roller. The mean momentum equation Eq. (3.2) predicts a 1:1 relationship (black lines) should exist for any integration region. Note the ~2x change in the axis scale between subplots A,B and subplots C,D. Vertical and horizontal (typically not visible) error bars show the uncertainties due to instrument accuracy (see Section 3.4.3).

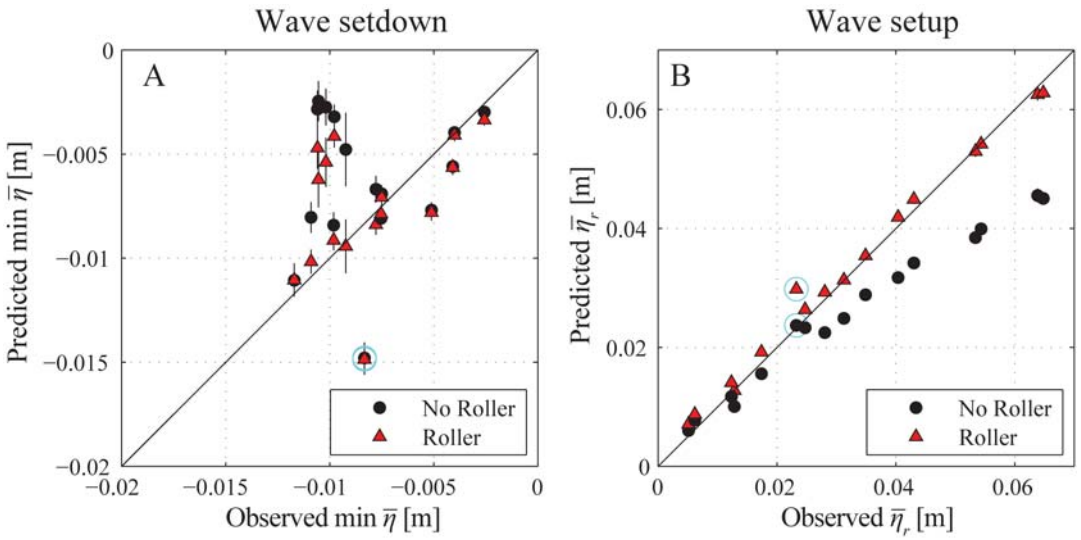

Figure 3.9: Comparison of predicted wave setdown (A) and setup (B) with observations. Predictions are evaluated from Eq. (3.13) without (i.e., S_{xx}) and with (i.e., $S_{xx} + R_{xx}$) the wave roller contribution to S_{xx}. Run 8 (discussed in the text) is highlighted by the cyan circles. Vertical and horizontal (generally not visible) error bars show the uncertainties due to instrument accuracy (see Section 3.4.3). Note the scale change between (A) and (B), which renders error bars in (B) less visible.

3.5.3. Parameterization of the wave roller model

We investigate how the accuracy of the setup prediction $\overline{\eta}_{pred}$ depends on β_D via Eq. (3.8), the sole parameter in the wave roller model. As described in Section 3.4.2, a single optimum value of $\beta_D = 0.19$ had been applied consistently across all runs. This optimum value of β_D was determined based on assessing the sensitivity of the wave roller model by varying β_D from 0 to 0.5 in increments of 0.01 (equivalent to varying θ_r from 0^o to 45^o; recall $\beta_D = \sin\theta_r \cos\theta_r$) that is now described here. To assess how β_D influences the predicted the setdown/ setup profiles via Eq. (3.13), for each run we evaluate the relative *rms* error ϵ_{rms} defined as:

$$\epsilon_{\text{rms}} = \sqrt{\frac{1}{N}\Sigma\left(\frac{\overline{\eta}_{i,pred}}{\overline{\eta}_r} - \frac{\overline{\eta}_{i,obs}}{\overline{\eta}_r}\right)^2}, \qquad (3.16)$$

where N is the total number of measurement sites and i denotes an individual measurement location. For most runs (Figure 3.10), using $\beta_D < 0.10$ results in high error (relative to other β_D values), which is equivalent to the mild wave roller inclination angle of $\theta_r < 6^o$. However, ϵ_{rms} is generally low when $\beta_D > 0.10$ (Figure 3.10). For almost all runs, the optimum β_D fell between 0.1 - 0.3. Runs 1, 8, and 12, where both $\overline{\eta}_r$ was small (Figure 3.6) and $\xi_0 \geq 2.3$ (Table 3.1), are exceptions with lower values of β_D improving the results. However, as noted previously, these were among the only runs

where the setup predictions were not improved by including the wave roller. In addition, Run 10 had a very high optimum β_D of 0.4; however, as seen for several other runs (notably Run 2-4), Run 10 was generally insensitive to $\beta_D > 0.10$. Overall, the mean optimum β_D for all runs was 0.19 ($\theta_r = 11^o$), approximately twice the $\beta_D = 0.1$ Reniers and Battjes (1997) reported to be optimum for spilling waves (with $\xi_0 = 0.2$ - 0.4 for waves breaking on their 1:20 beach slope).

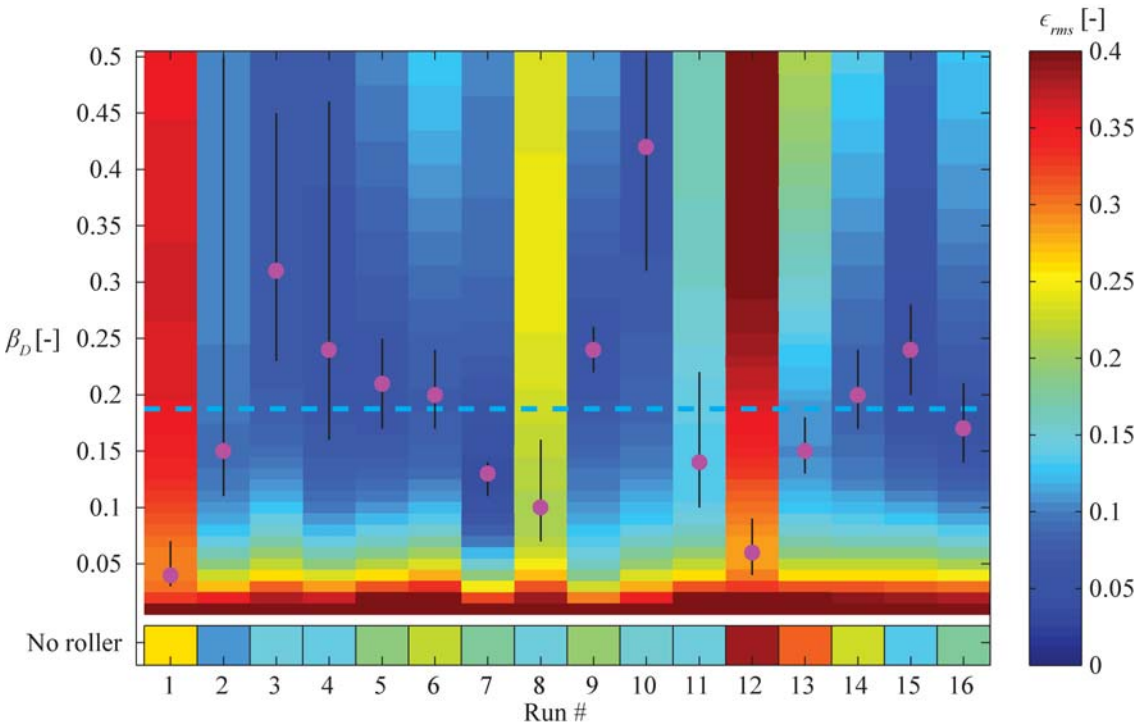

Figure 3.10: Relative *rms* error ϵ_{rms} (Eq. (3.16)) in the predicted setdown/ setup profiles ($\overline{\eta}_{pred}$) calculated from Eq. (3.13) with the wave roller contribution to radiation stress (R_{xx}) evaluated via Eq. (3.6) - (3.8) using various values of the roller slope coefficient (β_D). Magenta dots give the lowest ϵ_{rms} for each run, and the horizontal cyan dashed line gives the mean optimum $\beta_D = 0.19$ ($\theta_r = 11^o$) for the array of runs. For comparison, ϵ_{rms} without the wave roller is shown below the main plot.

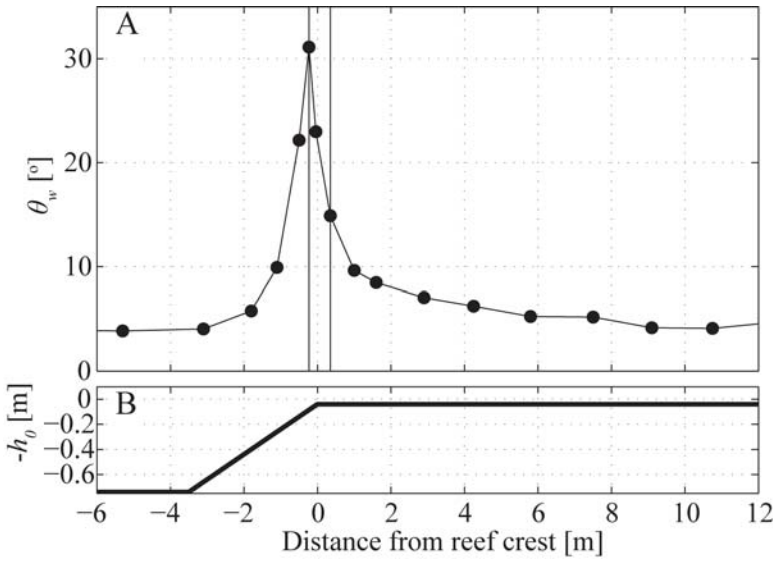

Figure 3.11: (A) Estimated wave front inclination angle (θ_w; Eq. (3.17)) across (B) the reef profile from well offshore of the break point to near the shoreline. Vertical black lines give the averaging area used to calculate the θ_w values shown in Figure 3.12.

Heuristically, we could expect there to be some physical relationship between the wave roller inclination angle θ_r within the wave roller dissipation model Eq. (3.8) and the wave front inclination angle θ_w in the surf zone that generally increases with breaker type from spilling to plunging (Battjes 1974). To investigate this, we obtained an estimate of θ_w from the water level time series in the surf zone and compared these values with the optimum θ_r from Figure 3.10. The instantaneous free surface inclination angle θ_η was estimated from the time rate of change of η from the water level time series based on the kinematic surface boundary condition as:

$$\theta_\eta(x,t) = \tan^{-1}\left(\frac{\partial \eta}{\partial x}\right) \approx \tan^{-1}\left(\frac{1}{c(f_{SS,mean})}\frac{\partial \eta}{\partial t}\right). \qquad (3.17)$$

For the calculation of individual trough-to-crest wave front inclination angles, individual waves were isolated using a zero-crossing analysis, and the *rms* value of the individual trough-to-crest wave front inclination angles were taken as θ_w. Figure 3.11 shows the full cross-shore development of θ_w for Run 4 (thus including non-breaking areas). The wave front inclination angle θ_w rapidly increased in the shoaling region, reaching a maximum value of ~30^o before decreasing during wave breaking. However, as we are only interested in θ_w where there is a wave roller (i.e., in the surf zone), we spatially-averaged θ_w over three surf zone wave gauges and compared the values to the optimum θ_r for each run (Figure 3.12). With the exception of the anomalous Run 10 (discussed previously), despite θ_w being larger than θ_r (as it should from theory), there was a strong linear relationship of increasing θ_r with θ_w. This suggests a physical basis

for assuming the wave roller model via Eq. (3.7) and provides an explanation for the higher optimum β_D (by approximately a factor of two) found here for the initially plunging waves, when compared to the optimum β_D reported by Reniers and Battjes (1997) for spilling waves.

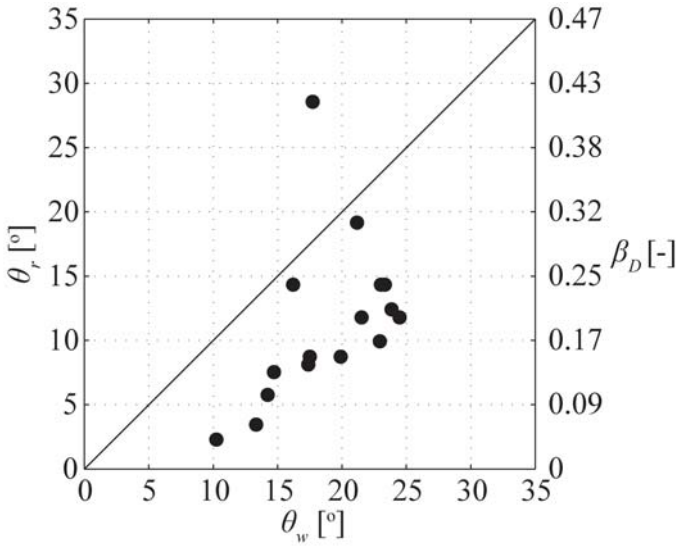

Figure 3.12: Variation of the optimum wave roller inclination angle (θ_r; the equivalent wave roller dissipation coefficient β_D is given on the secondary y-axis) with the measured wave front inclination angle (θ_w; Eq. (3.17)) spatially-averaged over the surf zone region indicated by the vertical black lines in Figure 3.11.

3.6. Discussion

In this study, we describe the first high-resolution observations of wave transformation and wave setup/setdown through the surf zone of a steeply-sloping reef profile, using a laboratory model with a bathymetry analogous to many natural fringing reefs. In contrast to previous reef hydrodynamic studies, this high-resolution dataset allows us to accurately quantify the mean cross-shore momentum balances across the reef from experimental observations alone, without relying on empirical or idealized models to predict radiation stress gradients through the surf zone. We found a breakdown in the local balance between pressure gradients and radiation stress gradients (approximated from linear wave theory) within the surf zone leading to a consistent under prediction in both the wave setdown and setup (Figure 3.4, Figure 3.5, Figure 3.6, and Figure 3.9).

From detailed PIV measurements of the velocities beneath plunging breaking waves (Govender et al. 2002), it appears that this breakdown within the surf zone of the balance between pressure gradients and radiation stress gradients derived from linear wave theory arises from inaccuracies in the theoretical description of the velocity field

within breaking waves. Linear wave theory and other non-breaking wave theories (e.g., cnoidal) assume that *PE* and *KE* are equal (Dean and Dalrymple 1991; Dean and Bender 2006; Svendsen 2006). Alternatively, wave roller theory postulates that *PE* during wave breaking, which is the quantity we can most readily measure, is first converted to *KE* prior to being dissipated (Svendsen 1984a). The increased *KE* is in the form of a wave roller traveling with the breaking wave, which has been observed to quickly form after wave plunging (Okayasu et al. 1986; Bonmarin 1989; Govender et al. 2002). As shown in Figure 3.3I (and further developed in Figure 3.3 J,K) a turbulent bore, not unlike the conceptual wave roller model, does begin to form shortly after the initial plunging point and propagates shoreward over the horizontal reef flat. For Run 4, when applying the mean water level profile with Eq. (3.14), this indicates that 70% of the decay of S_{xx} occurs on the horizontal reef flat, not on the reef slope. This is in agreement with results with the wave roller included, where ~65% of the decay of S_{xx}+R_{xx} occurs on the reef flat, but inconsistent with the results using linear wave theory alone (where only ~35% of S_{xx} decays on the reef flat). Thus despite wave plunging occurring on the steep reef slope (Figure 3.2), our results indicate that a large portion of the decrease in *PE* observed during the initial wave plunging is transferred shoreward onto the reef flat as *KE* in the form of the wave roller. This mechanism allows for $KE > PE$ in the surf zone, which although inconsistent with non-breaking wave theories, is required to locally balance pressure gradients through the surf zone for the majority of the runs (Figure 3.4, Figure 3.5, Figure 3.8).

Despite the wave roller being based on a simple conceptual model, we found that including the wave roller improved the local closure of the cross-shore mean momentum balances (Figure 3.8B,D) and thereby predictions of both setdown and setup (Figure 3.4D, Figure 3.5B, Figure 3.9). Run 16 (Figure 3.5C,D) gives an example of the maximum magnitudes of setdown and setup being well-predicted without the wave roller; however, even for this run the agreement with the observed setdown/ setup profile (not just $\overline{\eta}_r$) is improved by including the wave roller. Indeed, the only runs where the wave roller did not improve setup predictions were for runs approaching a surging breaker type ($\xi_0 \geq 2.3$).

The wave roller model implemented here includes a single parameter $\beta_D = \sin\theta_r \cos\theta_r$ (Dally and Brown 1995). From video analysis, Govender et al. (2002) reported a physical dependence of θ_r on the breaker type, with plunging waves reported to have larger θ_r than spilling waves. Thus, consistent with the measurements of

Govender et al. (2002), we found the optimum value of β_D = 0.19 for the plunging waves in this study to be larger than β_D = 0.1 found by Reniers and Battjes (1997) for spilling waves on their milder-sloping beach with ξ_0 < 0.4 (Figure 3.10). The higher optimum β_D value would thus increase the dissipation rate of the wave roller compared to Reniers and Battjes (1997). Optimum values of β_D for individual runs (Figure 3.12) also displayed a strong linear relationship between the related θ_r and the measured wave front inclination angle θ_w in the surf zone, further supporting that there is a physical basis for assuming a wave roller on this steeply-sloping reef profile.

The predicted wave setup on the reef flat was increased by 14-43% by including the wave roller with the most pronounced increases for runs with large setup (i.e., for runs having large incident wave heights and low still water depths). Wave setup was on-average under predicted by 28% when using linear wave theory alone to approximate radiation stress gradients, for the four runs with the largest setup. Including the wave roller reduced the under prediction to just 1.5%. These particular runs would have field-scale wave heights over 4 m, which are very typical of those experienced during large storms (e.g., Stephens and Ramsay 2014). As such, caution should be used when relying on results from linear wave theory approximations alone to predict setup, especially during the large wave conditions that are often the most important for coastal hazard assessments. We also note that Apotsos et al. (2007) used Eq. (3.7) to model the wave roller on a mild-sloping sandy beach profile (~1/100 slope) under more moderate wave conditions (H_{rms} = 0.2 to 2.1 m). Under these conditions, Apotsos et al. (2007) reported on average only an 11% increase in the predicted wave setup when including the wave roller. However, as we found here for the fringing reef profile, it is possible that further investigation of the effect of the wave roller on mild-slope sandy beaches could very well reveal an increased importance of the wave roller for much larger wave conditions than were considered in that study.

Similar to the imbalance between pressure and radiation stress gradients shown here for linear wave theory, phase-resolving numerical wave models, which include nonlinear effects but not overturning (e.g., those based on the nonlinear shallow water or Boussinesq equations) have also shown discrepancies in predicted wave setup on sleep slopes despite matching wave height observations (Skotner and Apelt 1999; Stansby and Feng 2004; Yao et al. 2012a). As we show for our observations that include a wave roller, these discrepancies are likely the result of not accurately modeling the *KE* of waves shoreward of wave plunging point. Indeed, Stansby and Feng (2004) showed that on the steep ~1:4 slopes of seadikes, model predictions of wave setup could be

improved by including a wave roller in their nonlinear shallow water wave model. It appears that the simple idealized model of a wave roller represents a physical correction to non-breaking wave theory and is capable of mimicking some of the more complex dynamics of wave breaking that would otherwise require a full three-dimensional highly computationally expensive free surface model (e.g., Torres-Freyermuth et al. 2007).

The use of a simple one-dimensional fringing reef profile with a smooth bed and an impenetrable shoreline reduced the general form of the cross-shore mean momentum equation (Eq. (3.1)) to a dynamic balance between the radiation stress and pressure gradients (Eq. (3.2)). However, on more complex two-dimensional reef geometries that include large roughness, both nonlinear advection and bottom stresses will be non-negligible requiring evaluation of a more general form of Eq. (3.1). Nevertheless, we still expect the importance of the wave roller to accurate predictions of setup to remain. In a numerical study of varying two-dimensional reef-lagoon systems, Lowe et al. (2010) found that wave setup generation in the surf zone was dominated by radiation stress gradients, and hence the setup on the seaward portion of the reef flat was largely independent of the lagoon and channel geometries. As such, a similar setup response to what we observed using this fringing reef profile, should likewise occur for more complex two-dimensional reef geometries. Similarly, incorporating wave roller formulations into a phase-resolving numerical wave model capable of modeling wave transformation on steeply-sloping reefs, such as used by Yao et al. (2012a) and Buckley et al. (2014), may improve numerical model predictions of wave setup. Such a model could then be used to further investigate wave setup dynamics and circulation for a much broader range of reef geometries.

An effort clearly needs to be made to more accurately measure the terms in the complete form of S_{xx} (Eq. (3.3)), especially within the surf zone, as this would be the greatest extension of these results. This work may also lead to further refinements in the wave roller model, possibly including the effects of spatially-variable wave front inclination angle. However, we emphasize that the simple idealized wave roller model used in this study reproduced the observations exceedingly well for the majority of wave and water level conditions. Furthermore, θ_r in the wave roller dissipation model was linearly related to the observed mean wave front inclination angle in the surf zone indicating that there is likely a physical basis for the simple shear stress dissipation formula of Dally and Brown (1995).

3.7. Conclusions

High-resolution laboratory observations were used to investigate the dynamics of wave setdown and setup across a steeply-sloping fringing reef profile. The one-dimensional profile with a smooth bed reduced the cross-shore mean momentum equation to a balance between the pressure and radiation stress gradients. This balance was evaluated using observations from seventeen locations across the reef profile for sixteen offshore wave and water level conditions. Radiation stress gradients calculated from observations using linear wave theory under predicted setdown (8 of 16 runs; by up to 77%) and setup (12 of 16 runs; by up to 31%) with inaccuracy increasing with increased offshore wave height. For the twelve runs where setup was under predicted (all having $H_{rms,0} \geq 2.2$ m in field scale), including a wave roller in the estimation of radiation stress gradients reduced the under prediction of setup from 21% to 3% on average. The wave roller accounts for an initial transfer of potential energy to kinetic energy during wave breaking thereby shifting the dissipation shoreward in line with pressure gradient observations. Evaluating the wave roller required a single parameter, the wave roller inclination angle, which was found to be linearly related to our estimates of the wave front inclination angle derived from the wave gauge observations. This relationship, combined with the improved agreement with the observed setdown/ setup profiles, suggests a physical basis for the wave roller. The wave roller was found to be most important for relatively large incident wave cases; therefore, under the conditions most critical to coastal hazard assessment.

3.8. Appendix A: Approximation of the time-averaged bottom stress

The time-averaged bottom stress $\overline{\tau}_B$ in Eq. (3.1) is commonly modelled using a quadratic drag law as (e.g., Grant and Madsen 1979; Feddersen et al. 2000; Mei 2005):

$$\overline{\tau}_b = \rho C_d \overline{|u_b| u_b}, \tag{3.A1}$$

where u_b is the instantaneous near-bed velocity in the cross-shore direction (taken at a height just above the bottom boundary layer) and C_d is a bottom drag coefficient that depends on properties of the bottom roughness, as well as the flow environment and the height above the bed at which u_b is taken. We approximate u_b as the sum of the depth- and time-averaged Eulerian velocity (below the mean water level) U_b and the instantaneous wave orbital velocity u_b'. Local continuity was used to approximate U_b as the offshore directed velocity necessary to balance the onshore directed mass flux above the mean water level due to finite-amplitude non-breaking waves and wave rollers (e.g., Apotsos et al. 2007; Lentz et al. 2008). The wave velocity u_b' was approximated using synthetically generated time-series (Ruessink et al. 2012), which accounted for wave energy density and mean wave period, as well as the velocity asymmetry and skewness predicted from the measured water level time-series.

For the case of the smooth bed, including $\overline{\tau}_b$ via Eq. (3.A1) with a physically meaningful C_d (i.e., order 0.001 for the smooth plywood bed; e.g., Longuet-Higgins 1970) has negligible effect on the closure of the mean momentum balance or the prediction of wave setup. For example, using a large $C_d = 0.005$ when predicting wave setup via Eq. (3.13) resulted in only a ~4% increase in the wave setup on the reef (when compared to using $\overline{\tau}_b = 0$). Furthermore, the cross-shore integrated residual of the pressure and radiation stress gradients varied about zero, and no significant correlation was found between the integrated residual and the integrated velocity term $\int \rho \overline{|u_b| u_b} dx$ (e.g., Feddersen et al. 2003). These findings indicate that for the smooth bed, the time-averaged bottom stress $\overline{\tau}_b$ was negligible for all runs (when compared to the radiation stress gradient), so for this study $\overline{\tau}_b = 0$ was used. However, this will not generally be the case, particularly for coral reefs, where the bottom roughness (and hence C_d) can be large.

3.9. Appendix B: Separation of shoreward and seaward propagating waves

A frequency domain algorithm (assuming linear wave theory) was used to separate shoreward ($^+$) and seaward ($^-$) propagating wave motion from synchronous velocity and water level time series. The shoreward F_η^+ and seaward F_η^- propagating Fourier components of a water level time series are related to the observed "total" Fourier components as $F_\eta = F_\eta^+ + F_\eta^-$; likewise, for the velocity components $F_u = F_u^+ + F_u^-$. Using the kinematic relationship between wave height and velocity, gives:

$$\begin{aligned} F_u^+ &= \frac{gk}{2\pi f} K_u F_\eta^+, \text{ and} \\ F_u^- &= -\frac{gk}{2\pi f} K_u F_\eta^-, \end{aligned} \tag{3.B1}$$

where k (f) is the wave number, and K_u (f) is the linear wave theory velocity response function, defined as:

$$K_u = \frac{\cosh\left(kh_u\right)}{\cosh\left(k(h_0 + \bar{\eta})\right)}, \tag{3.B2}$$

in which h_u is the height above the bed where velocity is measured. This gives a system of four equations with four unknown variables (F_η^+, F_η^- and F_u^+, F_u^-); rearranging yields equations for F_η^+ and F_η^- as:

$$\begin{aligned} F_\eta^+ &= \frac{1}{2}\left(F_\eta + \frac{2\pi f}{gkK_u} F_u \right), \text{ and} \\ F_\eta^- &= \frac{1}{2}\left(F_\eta - \frac{2\pi f}{gkK_u} F_u \right). \end{aligned} \tag{3.B3}$$

The inverse Fourier transformations of F_η^+ and F_η^- were used to generate time series of the shoreward and seaward propagating components of the wave signals, respectively.

4. Wave setup over a fringing reef with large bottom roughness

4.1. Abstract

The effect of bottom roughness on setup dynamics was investigated using high-resolution observations across a laboratory fringing reef profile with roughness elements scaled to mimic the frictional wave dissipation of a coral reef. Results with roughness were compared with smooth bottom runs across sixteen offshore wave and still water level conditions. The time-averaged and depth-integrated force balance was evaluated from observations collected at seventeen locations along the flume and consisted of cross-shore pressure and radiation stress gradients whose sum was balanced by quadratic mean bottom stresses. The introduction of roughness had two primary effects. First, for runs with roughness, frictional wave dissipation occurred on the reef slope offshore of the breakpoint reducing wave heights prior to wave breaking. Second, offshore directed mean bottom stresses were generated by the interaction of the combined wave-current velocity field with the roughness elements. These two mechanisms acted counter to one another. Frictional wave dissipation resulted in radiation stress gradients that were predicted to generate 18% (on average) less setup on the reef flat for rough runs than smooth runs when neglecting mean bottom stresses. However, mean bottom stresses increased the predicted setup by 16% on average for runs with roughness. As a result, setup on the reef flat was comparable (7% mean difference) between corresponding rough and smooth runs. These findings are used to assess prior results from numerical modelling studies of reefs, and also to discuss the broader implications for how large roughness influence setup dynamics in the nearshore zone.

4.2. Introduction

Bottom roughness contributes to frictional wave dissipation and time-averaged (mean) bottom stresses, which modify surf zone force balances and resulting wave setup and wave-driven circulation (Longuet-Higgins 1970, 2005; Dean and Bender 2006; Lowe et al. 2009a). As a result, the large roughness features (O(0.1 - 1 m)) typical of coral reefs can substantially influence a wide range of physical dynamics and dependent processes both physical (e.g., coastal inundation and sediment transport) and biological (e.g., larval and nutrient transport and dispersal) (Roberts et al. 1975; Monismith 2007; Lowe et al. 2010; Lowe and Falter 2015). Coral reefs are subject to a range of stressors (e.g., climate-induced coral bleaching, eutrophication), which can

ultimately reduce physical roughness through loss of coral cover (Alvarez-Filip et al. 2009) and in turn modify bottom stresses and alter reef hydrodynamics (Sheppard et al. 2005; Baldock et al. 2014; Quataert et al. 2015). In this paper we specifically investigate how the presence of bottom roughness modifies wave setup dynamics.

Wave setup (the mean increase in water level due to wave breaking), along with tides and storm surge, are the primary mechanisms controlling the water level at shorelines. Roughness affects setup through its contribution to the wave-averaged cross-shore momentum balance. For an alongshore uniform reef with normally-incident waves, the wave-averaged and depth-integrated momentum equation in the cross-shore direction (*x*-coordinate positive shoreward) can be expressed as (see Buckley et al. 2015a):

$$\underbrace{\frac{\partial\left(S_{xx}+R_{xx}\right)}{\partial x}}_{\substack{\text{radiation stress}\\ \text{gradient}}}+\underbrace{\rho g h\frac{\partial\overline{\eta}}{\partial x}}_{\substack{\text{pressure}\\ \text{gradient}}}+\underbrace{\overline{\tau}_b\sqrt{1+\left(\frac{\partial h_0}{\partial x}\right)^2}}_{\text{time-averaged bottom stress}}=0, \tag{4.1}$$

where the overbars denote time-averaging over many wave periods, S_{xx} is the cross-shore component of the wave radiation stress tensor (Longuet-Higgins and Stewart 1964), R_{xx} is the wave roller contribution to radiation stress (Svendsen 1984b), ρ is density, g is the gravitational acceleration, h_0 is still water depth, $\overline{\eta}$ is the time-averaged deviation of the free surface (η) from h_0, $h = h_0 + \overline{\eta}$ is the total water depth, and $\overline{\tau}_b$ is the mean bottom stress.

Eq. (4.1) describes the balance between the cross-shore components of the radiation stress and pressure gradients and the mean bottom stress. The radiation stress gradient term results from cross-shore gradients in potential and kinetic energy (e.g., due to wave shoaling and breaking) (Buckley et al. 2015a). In linear and other non-breaking wave theories (e.g., cnoidal; Svendsen 2006, p. 420), both potential and kinetic energy are equal, allowing radiation stresses to be calculated with wave energy taken as twice the potential energy (e.g., Dean and Dalrymple 1991; Dean and Bender 2006). However, for breaking waves there is an additional source of kinetic energy (and radiation stress) from the wave roller traveling with the breaking wave (Duncan 1981; Svendsen 1984b). The pressure gradient term results from cross-shore gradients in setdown and setup. The mean bottom stress ($\overline{\tau}_b$) is generated by the interaction of the combined wave-current velocity field with bottom roughness and is commonly modelled using a quadratic drag law as (e.g., Grant and Madsen 1979; Feddersen et al. 2000; Mei 2005):

$$\overline{\tau_b} = \rho C_d \overline{|u_b| u_b}, \tag{4.2}$$

where C_d is an empirical bulk bottom drag coefficient and u_b is the instantaneous cross-shore free-stream velocity above the bottom roughness. Consistent with the general form of the cross-shore momentum equation (Mei 2005, p. 554; Svendsen 2006, p. 532), $\overline{\tau_b}$ is modified by a bottom slope correction ($\sqrt{1+\left(\partial h_0/\partial x\right)^2}$) in Eq. (4.1). Though negligible for mild-slopes, the bottom slope correction to the cross-shore (horizontal) momentum balance increases with steeper bottom slopes due to the increased exposure of the near-bed flow to normal stresses on the vertically-sloping reef face (Svendsen 2006, p. 529-532).

Over smooth bottoms, Eq. (4.1) reduces to a balance between the radiation stress and pressure gradient terms (e.g., Bowen et al. 1968; Stive and Wind 1982; Buckley et al. 2015a). However, in the presence of roughness the momentum balance is altered in two primary ways: 1) by increasing frictional wave dissipation, which in turn modifies radiation stress gradients; and 2) by increasing the magnitude of $\overline{\tau_b}$ (Longuet-Higgins 2005; Dean and Bender 2006). Rates of frictional wave dissipation on coral reefs are commonly found to be at least one order of magnitude larger than is typical over smooth sandy bottoms (Lowe et al. 2009b; Huang et al. 2012; Monismith et al. 2013; Monismith et al. 2015). Lowe et al. (2009a) and Quataert et al. (2015) suggest that frictional wave dissipation offshore of the breakpoint may reduce setup on reefs. However, in part due to the difficulties in obtaining detailed surf zone measurements on coral reefs, the effects of these high frictional wave dissipation rates on setup dynamics have not yet been rigorously investigated experimentally.

The presence of a mean bottom stress ($\overline{\tau_b}$) can contribute to either reducing or enhancing setup, depending on the sign of the velocity term in Eq. (4.2) (Dean and Bender 2006). Like frictional wave dissipation, $\overline{\tau_b}$ is commonly reported to be an order of magnitude larger on reefs than smooth sandy beaches under the same flow conditions (Lowe et al. 2009a; Rosman and Hench 2011). Numerical studies have predicted a significant portion of the total setup over fringing coral reefs (i.e., those fronting a coastline) is due to $\overline{\tau_b}$ generated by offshore directed, near-bottom velocities (i.e., undertow) interacting with roughness (e.g., Franklin et al. 2013; Quataert et al. 2015). In contrast, Dean and Bender (2006) predicted that setup can theoretically be reduced when nonlinear wave orbital velocities interact with large roughness in the absence of any mean current.

Table 4.1: Simulated wave and water level conditions, including the deep water *rms* wave height ($H_{rms,0}$), peak period (T_p), still water depth on the reef flat ($h_{0,r}$), deep water wave steepness ($H_{rms,0}/L_0$), and deep water surf similarity parameter (ξ_0). Parameter values are given for both the laboratory scale (i.e., 1:36 geometric scaling and $1:\sqrt{36}$ scaling of time) and the equivalent field scale.

	Lab scale			Field scale				
	$H_{rms,0}$	T_p	$h_{0,r}$	$H_{rms,0}$	T_p	$h_{0,r}$	$H_{rms,0}/L_0$	ξ_0
Run	[m]	[s]	[m]	[m]	[s]	[m]	[-]	[-]
1	0.03	2.26	0.04	1.1	13.6	1.4	0.004	3.3
2	0.06	2.26	0.04	2.2	13.6	1.4	0.007	2.4
3	0.09	2.26	0.04	3.2	13.6	1.4	0.011	1.9
4	0.12	2.26	0.04	4.3	13.6	1.4	0.015	1.7
5	0.14	2.26	0.04	5.0	13.6	1.4	0.018	1.5
6	0.17	2.26	0.04	6.1	13.6	1.4	0.021	1.4
7	0.06	1.31	0.04	2.2	7.9	1.4	0.021	1.4
8	0.06	3.20	0.04	2.2	19.2	1.4	0.004	3.4
9	0.06	2.26	0.00	2.2	13.6	0.0	0.009	2.2
10	0.06	2.26	0.02	2.2	13.6	0.7	0.009	2.2
11	0.06	2.26	0.06	2.2	13.6	2.2	0.008	2.3
12	0.06	2.26	0.09	2.2	13.6	3.2	0.008	2.3
13	0.12	2.26	0.00	4.3	13.6	0.0	0.015	1.7
14	0.12	2.26	0.02	4.3	13.6	0.7	0.015	1.7
15	0.12	2.26	0.06	4.3	13.6	2.2	0.015	1.7
16	0.12	2.26	0.09	4.3	13.6	3.2	0.015	1.6

In this study, we quantify the effect of large bottom roughness on setup dynamics using a high-resolution laboratory dataset. Experiments were conducted in a 55-m long flume (1:36 scale) with a 1:5 reef slope leading to a wide shallow reef flat and sloping beach. The effect of roughness on setup was assessed by evaluating the cross-shore momentum balance from observations collected at seventeen locations along the flume. Buckley et al. (2015a) detail the cross-shore dynamics from the same flume, reef geometry, and wave conditions using a smooth bottom. In the present study, the sixteen offshore wave heights and still water level conditions of Buckley et al. (2015a) were repeated with the addition of a staggered array of cubes affixed to the reef slope and reef flat, which mimicked the typical bulk frictional wave dissipation characteristics of a coral reef. In this analysis, we specifically focus on how the introduction of the bottom roughness alters the wave dynamics and resulting setup profile. While this study is specifically motivated by how roughness modifies setup across reefs, our results are also broadly relevant to understanding how setup can be modified in other coastal systems having large roughness (e.g., as formed by aquatic vegetation, coarse sediment, bedforms, and karst topography).

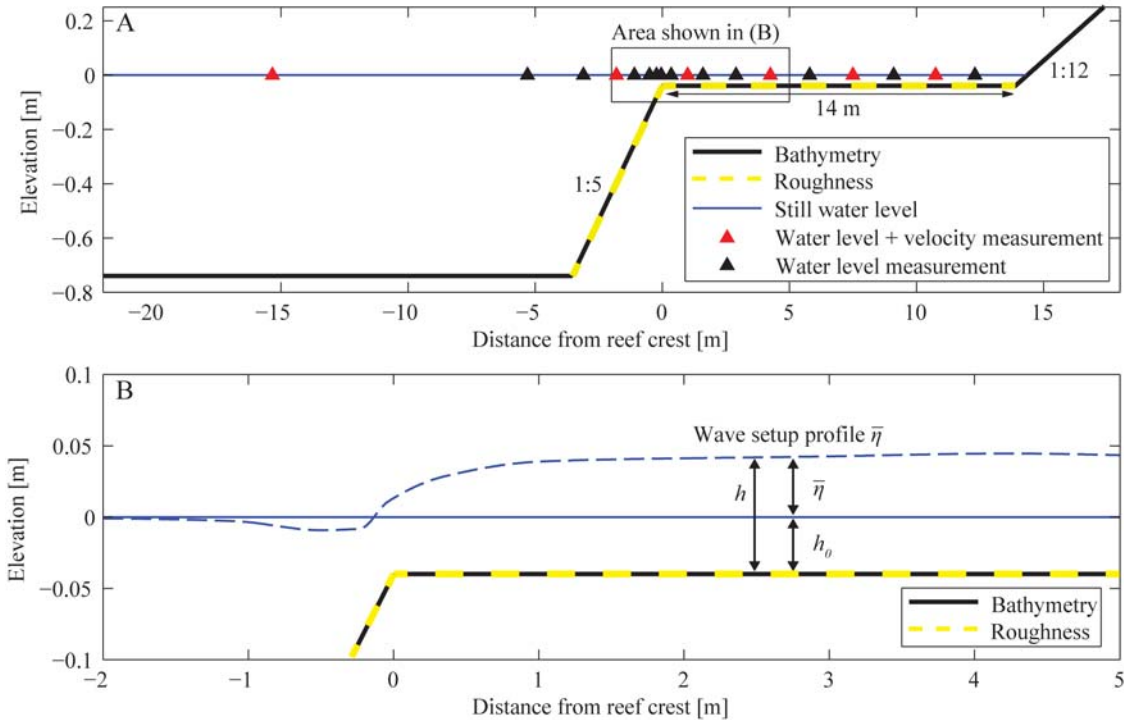

Figure 4.1: (A) Schematic of the fringing reef showing the reef slope (1:5), reef flat length (14 m; ~500 m field scale), beach slope (1:12), and instrument locations. Sections of the bathymetry (reef slope and reef flat) highlighted in dashed yellow were affixed with roughness elements as shown in Figure 4.2. (B) An example of the wave setup profile ($\overline{\eta}$) in the vicinity of the reef crest for Run 4, defining the still water depth (h_0) and the total water depth (h).

4.3. Methods

4.3.1. Experimental setup

Experiments were performed in a 55-m long wave flume (Eastern Scheldt Flume) at Deltares, the Netherlands (Figure 4.1). A 1:36 geometric scale fringing reef profile was constructed from marine plywood with a 1:5 reef slope, a 14 m horizontal reef flat (500 m in field (prototype) scale), and a 1:12 beach (Figure 4.1). The bathymetric characteristics of this reef fall within a typical range for fringing coral reefs (see Buckley et al. 2015a). Two sets of sixteen runs were conducted with varying still water depths on the reef flat ($h_{0,r}$) and offshore wave conditions (Table 4.1). The first set of runs, detailed by Buckley et al. (2015a), used a smooth bottom to minimize the role of bottom roughness on wave transformation and setup dynamics. In the second set of runs, bottom roughness was introduced using a staggered array of 1.8 cm (65 cm in field scale) concrete cubes affixed to the plywood bottom on the reef slope and reef flat (Figure 4.2). This idealized array of roughness elements was designed to replicate the typical bulk frictional wave dissipation characteristics of reefs (Lowe et al. 2005a),

while still being simple enough to have predictable hydrodynamic properties and be described with relatively few geometric variables. Analogous staggered arrays of roughness elements have been used to study flow through a variety of "canopies" (or "roughness-sublayers"), including buildings (Macdonald 2000; Belcher et al. 2003), aquatic vegetation (Nepf and Vivoni 2000), and coral reefs (Chamberlain and Graus 1975; Lowe et al. 2005b; Lowe et al. 2008; Zeller et al. 2015). The geometric properties of the cube array are defined by the horizontal and vertical dimensions of roughness elements l_h and l_v, respectively, and the density of roughness elements N (i.e., the number of roughness elements per unit plan area). From these variables, two non-dimensional parameters are defined:

$$\begin{aligned} \lambda_f &\equiv l_h l_v N, \text{ and} \\ \lambda_p &\equiv l_h l_h N, \end{aligned} \tag{4.3}$$

where λ_f is the frontal area of roughness elements per unit plan area and λ_p is the plan area of roughness elements per unit plan area. For the array of cubes used in this study, $N = 400$ m^{-2}, $l_h = l_v = 1.8$ cm, and $\lambda_f = \lambda_p = 0.13$ (Figure 4.2), which is smaller than $\lambda_f = 0.42 - 6.31$ and comparable to $\lambda_p = 0.02 - 0.38$ reported for branched reef corals by Lowe et al. (2005a). We note that the presence of the solid roughness elements can modify the total water depth. Defining the total water depth (h) as the fluid volume in the water column divided by the plan area yields:

$$h = h_0 + \overline{\eta} - \lambda_p l_v \tag{4.4}$$

where $h_0 + \overline{\eta}$ is the total water depth over a smooth bottom and $\lambda_p l_v = 0.002$ m is a correction due to the solid volume occupied by the roughness elements. However, this depth correction is less than 6% of the observed $h_0 + \overline{\eta}$, even on the shallow reef flat for cases where h_0 was lowest.

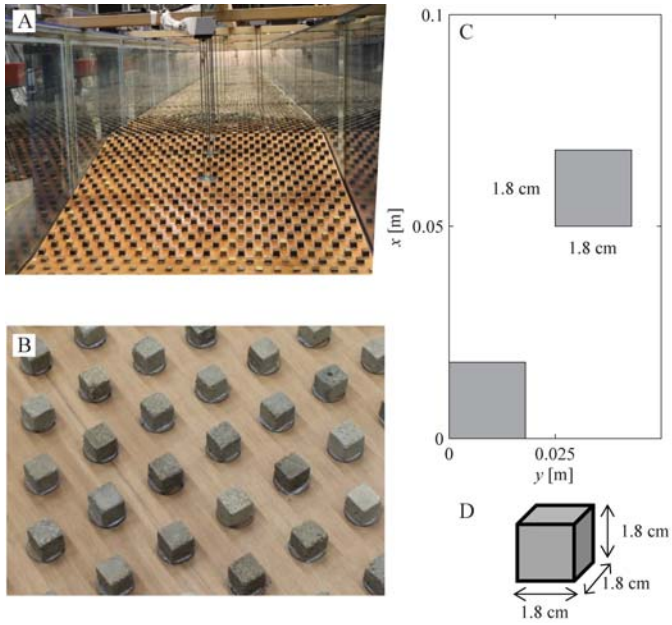

Figure 4.2: (A) View of the dry flume with roughness elements looking shoreward from offshore of the reef slope. (B) Roughness elements used were (D) 1.8 cm concrete cubes affixed in the repeating staggered pattern shown in (C). This pattern gave $N = 400$ m^{-2} cubes per unit plan area, with 7,000 cubes in total covering the reef slope and flat.

Irregular waves with a TMA spectrum (Bouws et al. 1985) were generated with a piston-type wave maker with second-order wave generation and active reflection compensation (van Dongeren et al. 2002). Water levels (17 locations with resistance-type gauges) and horizontal velocities (6 locations with electromagnetic current meters) were measured synchronously at 40 Hz, with the highest density of measurements in the surf zone region near the reef crest at $x = 0$ m (Figure 4.1). On the reef flat and reef slope, instruments were recessed into the bed to sample in the shallow depths (Eslami Arab et al. 2012). At these locations, velocities were sampled over a volume extending from 2 - 2.5 cm above the bottom (the center of the volume was located at $z = -h_0 + 0.0225$ m, where z is the vertical coordinate positive upward from h_0). At other offshore locations, velocities were sampled at approximately the middle of the water column.

4.3.2. Calculation of radiation stresses

The methods used to evaluate both the wave (S_{xx}) and wave roller (R_{xx}) contributions to radiation stress are described in detail in Buckley et al. (2015a) and briefly recounted here. Wave spectra ($C_{\eta\eta}$) were computed using Welch's modified periodogram with a Hanning window and a segment length of 2^{14} samples (~410 s; 41 min in field scale). From $C_{\eta\eta}$, the wave energy flux (F) was evaluated as:

$$F = \rho g \int c_g C_{\eta\eta}\, df. \tag{4.5}$$

The wave energy flux was separated into a component F_{SS} from sea-swell (*SS*) waves and a component F_{IG} from infragravity (*IG*) waves. The *SS* band was defined as $f \geq f_p/2$ and the *IG* band was defined as $0.025 \leq f < f_p/2$, where f_p is the peak forcing frequency of each wave case (Table 4.1). Following Buckley et al. (2015a), the co-located synchronous water level and velocity measurements were used to estimate the shoreward propagating components of wave energy flux (F_{SS}^{+} and F_{IG}^{+}) from which S_{xx} was evaluated at instrument locations as:

$$S_{xx} = \frac{F_{SS}^{+}}{c_g(f_{SS,mean})}\left(2\frac{c_g(f_{SS,mean})}{c(f_{SS,mean})} - \frac{1}{2}\right) + \frac{F_{IG}^{+}}{c_g(f_{IG,mean})}\left(2\frac{c_g(f_{IG,mean})}{c(f_{IG,mean})} - \frac{1}{2}\right), \tag{4.6}$$

where $f_{SS,mean}$ and $f_{IG,mean}$ are defined as the mean frequencies for the *SS* and *IG* waves, respectively.

As discussed in Buckley et al. (2015a), wave rollers contribute an additional source of radiation stress R_{xx} in the surf zone as (Svendsen 1984b):

$$R_{xx} = 2E_r, \tag{4.7}$$

where E_r is the kinetic energy of the wave roller, modeled using an approximate energy balance following Stive and De Vriend (1994):

$$\frac{\partial}{\partial x}\left(2E_r c\right) = D_{br} - \overline{\tau}_t c. \tag{4.8}$$

Here D_{br} is the wave breaking dissipation rate and $\overline{\tau}_t$ is the mean shear stress at the boundary between the turbulent roller and the underlying organized wave motion. Following Buckley et al. (2015a), $\overline{\tau}_t$ is modeled according to Dally and Brown (1995) with the wave roller dissipation coefficient β_D =0.019 found to be optimum by Buckley et al. (2015a) for the smooth runs. Wave breaking dissipation was isolated from the total dissipation as:

$$D_{br} = \underbrace{-\frac{\partial(F_{SS}^{+} + F_{IG}^{+})}{\partial x}}_{\substack{\text{total}\\ \text{dissipation}}} - \underbrace{D_{fric}}_{\substack{\text{roughness}\\ \text{dissipation}}}, \tag{4.9}$$

where D_{fric} is the frictional wave dissipation, modelled as (Jonsson 1966):

$$D_{fric} = \frac{1}{2}\rho f_w \overline{\left|u_b'^3\right|}, \tag{4.10}$$

where f_w is the wave friction factor (detailed in Section 4.4.1) and u_b' is the wave component of u_b (see Section 4.3.3).

The methods by which radiation stresses were estimated account for nonlinear wave shape through a spectral representation of the wave field (see Buckley et al. 2015a). Conservative nonlinear interactions between sea-swell and infragravity waves are inherently accounted for, as Eq. (4.1) is averaged over both sea-swell and infragravity wave frequencies. All waves are assumed to be free and progressive despite that a portion of the shoreward propagating infragravity energy offshore of the breakpoint is likely bound to the sea-swell wave groups (Longuet-Higgins and Stewart 1962; Longuet-Higgins and Stewart 1964). However, due to the low proportion (less than 4%) of infragravity wave energy offshore of the breakpoint (Buckley et al. 2015a), the assumption of free versus bound infragravity waves has negligible effect on the calculation of S_{xx} and hence wave setup. Likewise, nonlinear interactions between sea-swell and infragravity waves which can modify the infragravity wave energy balance (Henderson et al. 2006; Pequignet et al. 2014) are calculated to be less than 5% of the combined sea-swell and infragravity wave energy flux and therefore negligible in this evaluation of wave setup dynamics.

4.3.3. Evaluation of velocities

Although velocities were measured at 6 locations (Figure 4.1), higher spatial resolution was required to determine the mean bottom stress term in Eq. (4.1) across the reef profile. The methods used to predict velocities are detailed below and comparisons of the predicted and observed velocities are included in Section 4.4.4. The instantaneous velocity (u_b) was composed of a steady (current) component U_b and an unsteady (wave) component u_b':

$$u_b = U_b + u_b', \tag{4.11}$$

where the subscript "*b*" denotes the free-stream velocity at the top of the roughness elements $(z = -h_0 + l_v)$. The steady component U_b was approximated as the time- and depth-averaged Eulerian velocity (Apotsos et al. 2007; Lentz et al. 2008). For all cases considered here, the system was in steady-state when averaged over many wave cycles (i.e., $\overline{\partial / \partial t} = 0$) and the shoreline was impermeable, such that the time-averaged and depth-integrated Lagrangian mass flux was zero (e.g., Mei 2005). This allowed U_b to be approximated from local continuity as the offshore directed velocity necessary to balance the onshore directed mass flux above the mean water level due to finite-

amplitude non-breaking waves and wave rollers (Faria et al. 2000; Apotsos et al. 2007; Lentz et al. 2008):

$$U_b = -\underbrace{\frac{M_w}{\rho h}}_{\substack{\text{wave}\\ \text{mass fux}}} - \underbrace{\frac{M_r}{\rho h}}_{\substack{\text{wave roller}\\ \text{mass flux}}}, \tag{4.12}$$

where $M_w = E/c$ (based on the wave energy density $E = F/c_g$) and $M_r = 2E_R/c$ are the depth-integrated and time-averaged Eulerian mass fluxes due to the non-breaking waves and wave rollers, respectively.

The wave velocity (u_b') for the combined sea-swell and infragravity wave field was approximated using a time-series of nonlinear waves based on Ruessink et al. (2012):

$$u_b' = \underbrace{\frac{H_{rms}\omega_{mean}\cosh(k_{mean}l_v)}{2\sinh(k_{mean}h)}}_{\text{velocity amplitude}} \underbrace{\Psi(t, f_{mean}, A_u, S_u)}_{\text{periodic forcing function}}, \tag{4.13}$$

where H_{rms} is the combined sea-swell and infragravity root-mean-squared (*rms*) wave height, f_{mean} is the mean frequency, $\omega_{mean} = 2\pi f_{mean}$ is the mean angular frequency, and k_{mean} is the mean wave number approximated from linear wave theory. The first term represents the linear wave theory-derived wave velocity amplitude for free progressive waves and the second term is a normalized periodic forcing function (Ψ) that generates a time (t) dependent signal of frequency f_{mean} with velocity asymmetry (A_u) and velocity skewness (S_u) (see Ruessink et al. (2012) for the mathematical form and evaluation of Ψ). Velocity skewness (S_u) and asymmetry (A_u) are measures of the asymmetry of the velocity signal about the horizontal and vertical axes, respectively, and thus influence the mean bottom stress via the velocity term in Eq. (4.2). Velocity skewness is defined as:

$$S_u \equiv \frac{\overline{u_b'^3}}{\sigma_u^3}, \tag{4.14}$$

where σ_u is the standard deviation of u_b'. Velocity asymmetry (A_u) is defined similarly to Eq. (4.14), but with u_b' replaced by its Hilbert transform (Ruessink et al. 2012). The velocity nonlinearity parameters (S_u and A_u) were evaluated from velocity time-series where available and by using the linear wave theory transfer function (e.g., Guza and Thornton 1980) to first convert water level time-series to predicted velocity time-series for sites with only water level measurements (Figure 4.1).

4.3.4. Evaluation of the mean momentum equation

Terms in mean momentum equation were evaluated from observations of Su, Au, $\overline{\eta}$, f_{mean}, $f_{SS,mean}$, $f_{IG,mean}$, F_{SS}^{+}, and F_{IG}^{+}, which were interpolated using a shape-preserving piecewise cubic algorithm onto a uniform 0.01 m grid extending from offshore (x = -4.0 m) to near the shoreline (x = 14 m) (Buckley et al. 2015a). Over this domain, the cross-shore spacing between wave gauges varied from 0.19 m (~1/40 of the incident wave length) in the surf zone to 1.7 m (~1/4 of the incident wave length) on the reef flat (Figure 4.1). At each grid location, the mean bottom stress was evaluated from the interpolated observations via Eq. (4.2), where U_b and u_b' were evaluated via Eq. (4.12) and (4.13), respectively. The radiation stresses (S_{xx} and R_{xx}) were evaluated from the interpolated observations via Eq. (4.6) and Eq. (4.7), respectively. Cross-shore pressure and radiation stress gradient terms were computed using central differencing. The contributions of radiation stress gradients and mean bottom stresses to the setup response were evaluated by "predicting" setup across the reef, via Eq. (4.1) as (e.g., Raubenheimer et al. 2001; Buckley et al. 2015a):

$$\overline{\eta}_{pred} = -\int_{x_0}^{x} \frac{1}{\rho g h}\left[\frac{\partial(S_{xx}+R_{xx})}{\partial x} + \overline{\tau}_b\sqrt{1+\left(\frac{\partial h_0}{\partial x}\right)^2}\right]dx + \overline{\eta}\left(x_0\right), \qquad (4.15)$$

where the integration was initialized at a seaward deep-water boundary x_0 (x_0 = -4 m in Figure 4.1), where we assume $\overline{\eta}$ (x_0) = 0, and was evaluated iteratively using trapezoidal integration.

4.3.5. Uncertainty estimates

Using the same resistance-type water level gauges, Buckley et al. (2015a) estimated uncertainties of ± 0.5% outside of the surf zone and ± 1.5% within the surf zone of the measured range for time-averaged water levels. Likewise, uncertainties were estimated to be ± 2% outside of the surf zone and ± 7% inside the surf zone for parameters proportional to wave height squared (e.g., wave energy and radiation stresses). The larger uncertainty values within the surf zone are due to aeration of the water column during wave breaking (Stive and Wind 1982). The effect of these uncertainties on the cross-shore integration of Eq. (4.1) and (4.15) was assessed by performing 100 Monte Carlo simulations, where uncertainties were modeled as having zero-mean Gaussian random distributions with a standard deviation equivalent to the uncertainty.

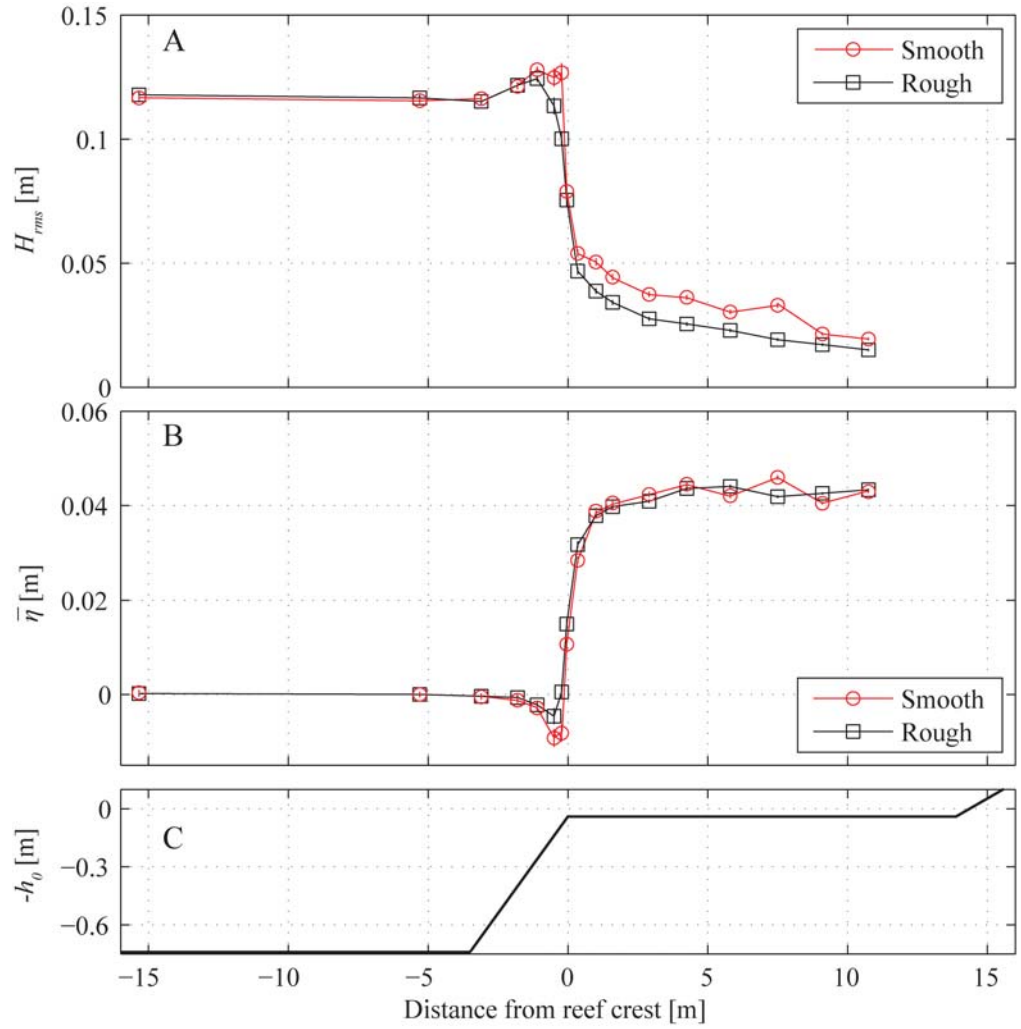

Figure 4.3: (A) Wave height (H_{rms}) and (B) wave setup ($\overline{\eta}$) across (C) the fringing reef profile for Run 4 both including ("rough") and without ("smooth") roughness. Vertical error bars show the uncertainties due to instrument accuracy and are negligible here (see Section 4.3.5).

4.4. Results

4.4.1. Wave transformation and setup dynamics

Buckley et al. (2015a) describe the dynamics of wave transformation and resulting setdown and setup for the smooth runs; here we specifically focus on the dynamical differences due to the inclusion of bottom roughness. Following Buckley et al. (2015a), we first outline the results from a moderate case (Run 4), which had a relatively large (0.12 m; 4.3 m in field scale) deep water wave height and an intermediate (0.04 m; 1.4 m in field scale) still water depth (Table 4.1). Compared to Run 4 over the smooth bottom, including roughness led to a slightly reduced wave height at the breakpoint and across the reef flat (Figure 4.3A). This pattern was consistent across all runs (Figure 4.4A). The wave height-to-water depth ratios on the reef flat were also lower for runs with roughness (Figure 4.4B), due to increased frictional wave dissipation on the reef flat. From the dimensions and spacing of the

roughness elements and the wave forcing, the wave friction factor predicted using the canopy flow equations of Lowe et al. (2007) is f_w = 0.16. Using Eq. (4.9) and (4.10) along with the wave energy dissipation rate $(\partial(F_{SS}^{+} + F_{IG}^{+})/\partial x)$ measured on the reef flat shoreward of surf zone where wave breaking was absent (x > 8m), we find a comparable f_w = 0.2 for all runs with roughness. The value f_w = 0.2 is also within the typical range for many coral reefs; for example, f_w = 0.15 (Nelson 1996), f_w = 0.22 (Falter et al. 2004), and f_w = 0.24 (Lowe et al. 2005b).

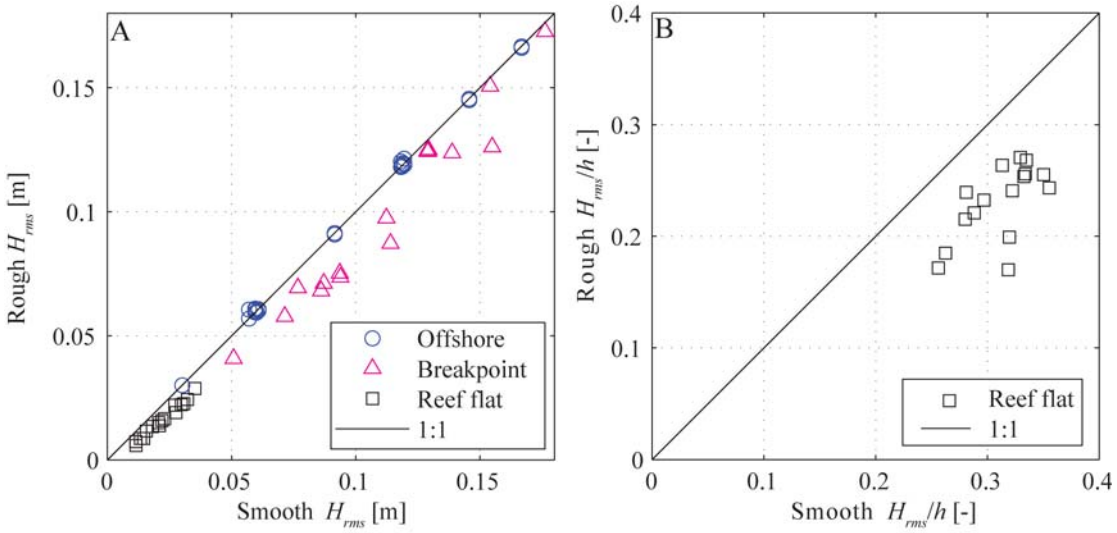

Figure 4.4: (A) Comparison of the *rms* wave heights (H_{rms}) and (B) wave height-to-water depth ratios (H_{rms}/h) on the reef flat for runs including ("rough") and without ("smooth") roughness.

Setup profiles for Run 4 were similar between the rough and smooth runs (Figure 4.3B); however, we note that there were differences near the reef crest (x = 0 m) and that setdown for the smooth Run 4 was twice that of the rough Run 4 (Figure 4.3B). On average across all runs, setdown was 80% larger for the smooth runs than the rough runs (Figure 4.5A). Of particular interest is setup on the reef flat, which was relatively constant for x > 4 m (Figure 4.3B). As such, following Buckley et al. (2015a), we define the representative setup on the reef flat $\overline{\eta}_r$ as the spatially-averaged $\overline{\eta}$ between x = 4 - 10 m (Figure 4.3B). Despite differences in the wave height profiles and $\overline{\eta}$ near the reef crest, for Run 4 $\overline{\eta}_r$ was identical ($\overline{\eta}_r$ = 0.043 m) for both the rough and smooth runs (Figure 4.3B). On average across all runs, there was only a 7% difference in $\overline{\eta}_r$ between rough and smooth runs (Figure 4.5B). The total setup generated ($\Delta\overline{\eta}$), defined as the difference between maximum setdown and $\overline{\eta}_r$, was larger in the smooth runs, with the exception of Run 1 that had the smallest $\Delta\overline{\eta}$ (Figure 4.5C).

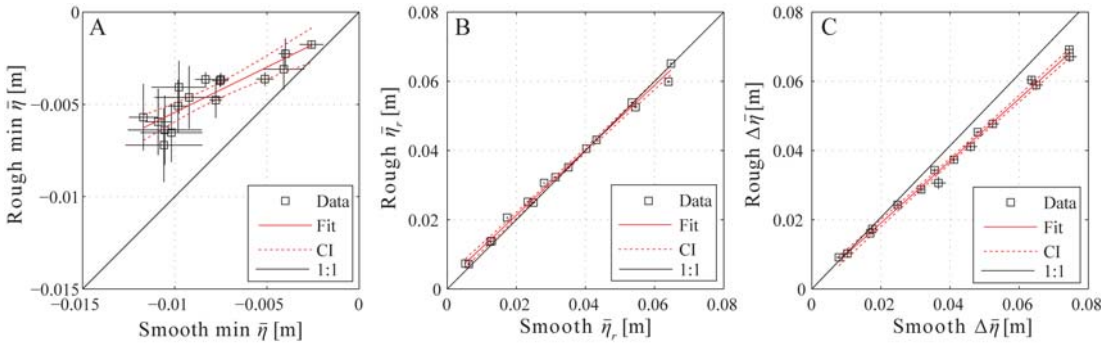

Figure 4.5: (A) Comparison of maximum setdown, (B) setup on the reef flat ($\bar{\eta}_r$), and (C) setup generation ($\Delta\bar{\eta}$) for runs including ("rough") and without ("smooth") roughness. Solid red lines give the linear least squares trend lines ("fit") and dashed red curves give the upper and lower bounds of the 95% confidence interval ("CI") for the trend line. Vertical and horizontal error bars show the uncertainties due to instrument accuracy (see Section 4.3.5). Note the scale change between (A) and (B) and (C), which renders error bars in (B) and (C) less visible.

4.4.2. Evaluation of the mean bottom stress

To relate the observations of $\bar{\eta}$ to the mean momentum balance, we first integrate Eq. (4.1) in the cross-shore direction:

$$\int_{x_0}^{x} \frac{\partial\left(S_{xx}+R_{xx}\right)}{\partial x}dx+\int_{x_0}^{x}\rho gh\frac{\partial\bar{\eta}}{\partial x}dx+\int_{x_0}^{x}C_d\rho\overline{|u_b|u_b}\sqrt{1+\left(\frac{\partial h_0}{\partial x}\right)^2}dx=0, \qquad (4.16)$$

where the bounds of integration were taken from seaward of the breakpoint (x_0 = -4 m) to a point on the reef flat (x = 4 m) shoreward of the surf zone where $\bar{\eta}$ becomes relatively constant (i.e., $\bar{\eta}(x)\approx\bar{\eta}_r$). We note that the cross-shore integrated radiation stress gradient is only dependent on the endpoint values, allowing us to restate the term as $\Delta\left(S_{xx}+R_{xx}\right)$. Buckley et al. (2015a) found that for the smooth runs where $\bar{\tau}_b\approx 0$, Eq. (4.16) reduced to a balance between the cross-shore integrated pressure and radiation stress gradients (red circles approximately along the 1:1 line in Figure 4.6). Conversely for runs with roughness, the cross-shore integrated pressure gradient was typically larger than the cross-shore integrated radiation stress gradient (black squares in Figure 4.6). Assuming the momentum balance (Eq. (4.16)), these differences should be accounted for by the contribution of the cross-shore integrated mean bottom stress term.

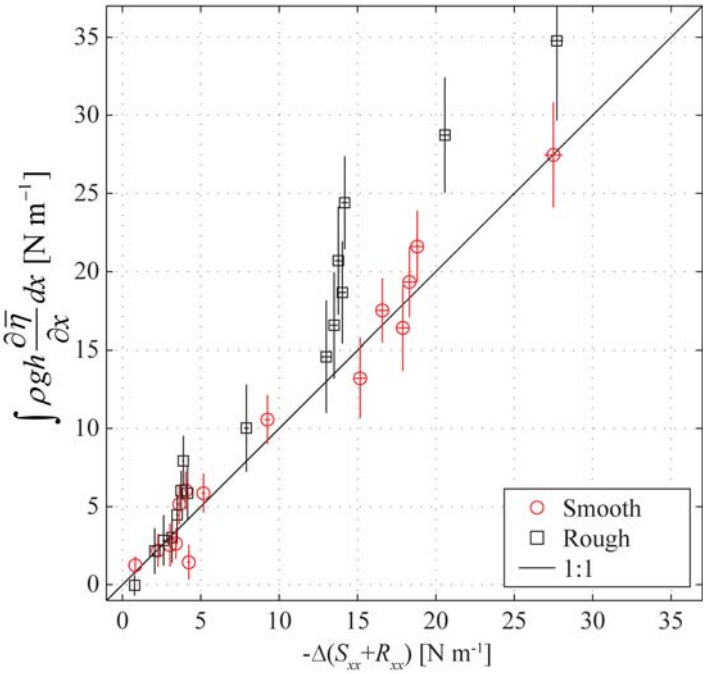

Figure 4.6: Comparison of the cross-shore integrated radiation stress ($-\Delta\left(S_{xx}+R_{xx}\right)$) and pressure gradient terms for runs including ("rough") and without ("smooth") roughness. Vertical and horizontal (generally not visible) error bars show the uncertainties due to instrument accuracy (see Section 4.3.5).

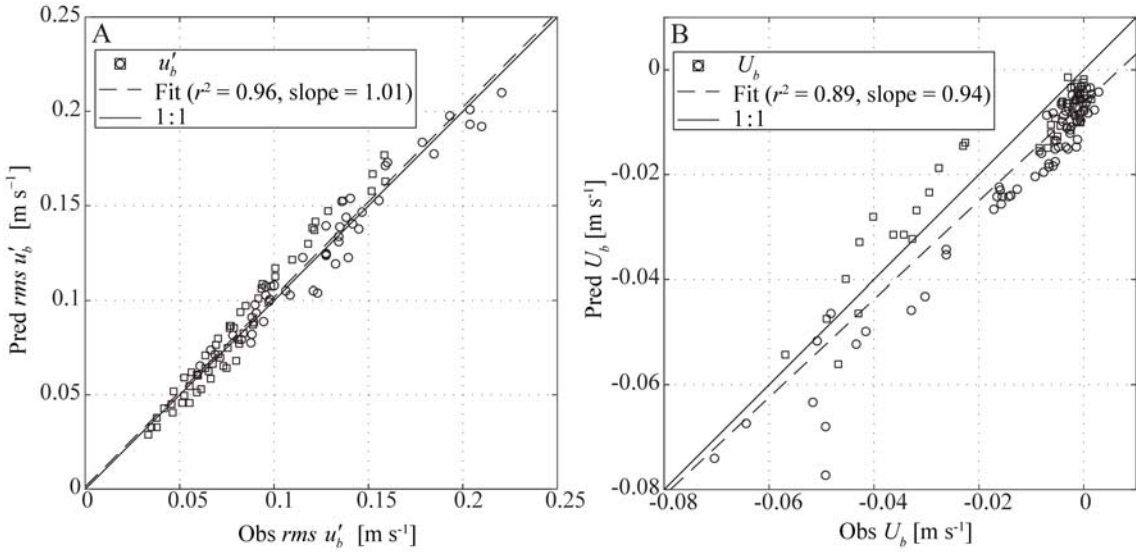

Figure 4.7: Comparisons of the observed ("obs") and predicted ("pred") time-averaged (A) *rms* wave velocities (u_b') and (B) mean velocities (U_b). Data are shown for both smooth runs (open circles) and with roughness (open squares). Dashed lines give the linear least squares trend lines while the solid line indicates 1:1.

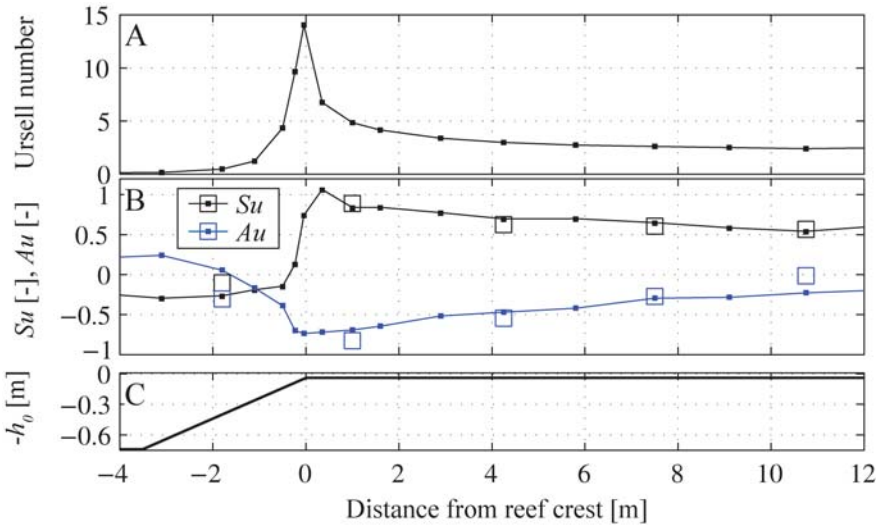

Figure 4.8: (A) Ursell number (a measure of wave nonlinearity; Doering and Bowen 1995) and (B) velocity skewness (*Su*) and asymmetry (*Au*) are shown over (C) the bathymetric profile for runs including roughness. In (B) small filled squares and connecting lines are *Su* and *Au* approximated from water level time-series and large open squares are values calculated from the velocity time-series.

To evaluate the mean bottom stress term via Eq. (4.2) requires estimates of the bulk bottom drag coefficient (C_d) and the instantaneous free-stream near-bottom velocity (u_b). The near-bottom velocity (u_b) was estimated as the sum of a mean current component and a nonlinear wave component (following Eq. (4.12) and (4.13), respectively). The *rms* wave velocity was determined via linear wave theory based on the observed wave field. At locations where velocity was measured the estimated wave velocities agreed with the observations (r^2 = 0.96; slope = 1.01; Figure 4.7A). As the waves and corresponding velocities demonstrated nonlinear characteristics (Figure 4.8), velocity skewness (*Su*) and asymmetry (*Au*) were included via the periodic forcing function in Eq. (4.13). The mean current velocities predicted based on the wave and wave roller mass flux also compared well with observations (r^2 = 0.89; slope = 0.94; Figure 4.7B). From Eq. (4.16), a representative C_d was estimated as the least-squares slope between the sum of the cross-shore integrated pressure and radiation stress gradients and the cross-shore integrated velocity term from all runs including roughness (e.g., Feddersen and Guza 2003) (Figure 4.9). This yielded C_d = 0.028 (r^2 =0.7), which is an order of magnitude larger than that typically found on smooth sandy beaches O(0.001) (e.g., Faria et al. 1998), but within the range from 0.02 to 0.1 reported for coral reefs (Lowe et al. 2009a; Rosman and Hench 2011).

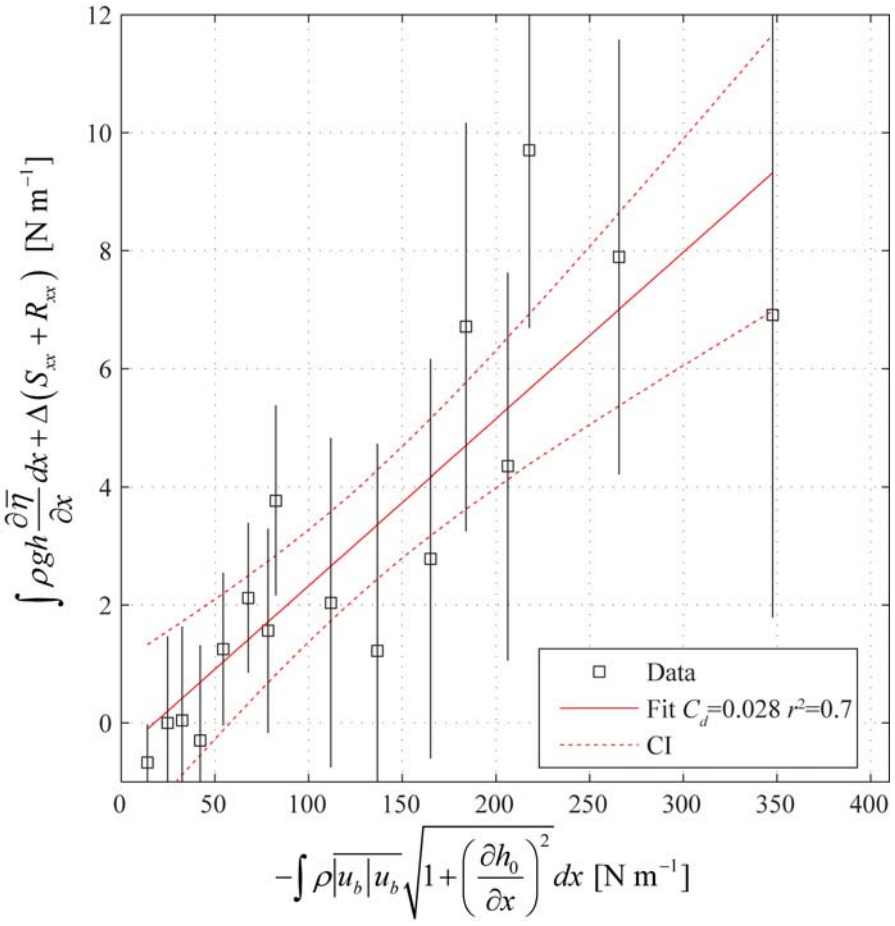

Figure 4.9: Comparison of the cross-shore integrated time-averaged velocity term with the sum of the cross-shore integrated pressure and radiation stress gradient terms for runs including roughness. Per Eq. (4.16), the linear least squares trend line ("fit"; solid red lines) gives the estimated bulk bottom drag coefficient (C_d = 0.028) cross-shore averaged and averaged across all runs with roughness. The dashed red curves show the upper and lower bounds of the 95% confidence interval ("CI") for the trend line. Vertical error bars show the uncertainties due to instrument accuracy (see Section 4.3.5).

4.4.3. Predicted wave setup

The estimated radiation stresses and mean bottom stresses (computed using C_d = 0.028 and u_b) were used to predict the cross-shore setup profiles via Eq. (4.15) and compared with the observed setup (Figure 4.10 and 4.11). For Run 4 with roughness (Figure 4.10), neglecting $\bar{\tau}_b$ (C_d = 0) resulted in a 16% underprediction of $\bar{\eta}_r$, which was reduced to only 2% when $\bar{\tau}_b$ (C_d = 0.028) was included (Figure 4.10). Across all runs with roughness, $\bar{\eta}_r$ was underpredicted by 18% on average when $\bar{\tau}_b$ was neglected (Figure 4.11) compared to 7% when $\bar{\tau}_b$ was included with C_d = 0.028 (Figure 4.11). Neglecting infragravity waves decreased the predicted $\bar{\eta}_r$ by only 3% on average.

Table 4.2: The instantaneous near-bottom velocity (u_b) was composed of a near-bottom current (U_b) and a wave component (u_b') that had both asymmetry (*Au*) and skewness (*Su*) (Figure 4.7B). The full velocity approximation following Eq. (4.12) and (4.13) is presented in row four, as well as velocity estimates neglecting: 1) u_b' and the contribution of the wave roller mass flux (M_r), 2) u_b', and 3) *Au* and *Su*. These velocity approximations are implemented in various classes of models as indicated in the "application" column. Large discrepancies in the predicted velocities (Figure 4.11) result in variation in the bulk bottom drag coefficients (C_d) (Figure 4.12).

Velocity approximation	**Application**	C_d
$u_b = U_b$ with $M_r = 0$	Most analytical models	0.23
$u_b = U_b$	Most models including a wave roller	0.066
$u_b = U_b + u_b'$ with $Au = Su = 0$	Most phase-averaged models including a wave roller	0.027
$u_b = U_b + u_b'$ with Au and Su	Phase-resolving models and some phase-averaged models including a wave roller	0.028

4.4.4. Bottom stress decomposition

Thus far, $\overline{\tau}_b$ has been evaluated via Eq. (4.2) using velocity estimates that include contributions from near-bottom currents (Eq. (4.12)), wave velocities (Eq. (4.13)), and the interactions between the two. However, many analytical and numerical models estimate u_b in differing ways and generally only resolve certain contributions to the true velocity field, as summarized in Table 4.2. Figure 4.12 shows a comparison of $\overline{|u_b|u_b}$ calculated using the observed velocity from locations with current meters on the reef flat (Figure 4.1) with $\overline{|u_b|u_b}$ predicted via Eq. (4.12) and Eq. (4.13) and with various individual contributions to u_b neglected (see Table 4.2). The full velocity estimate using Eq. (4.12) and (4.13) (i.e., $u_b = U_b + u_b'$ with *Au* and *Su* calculated from observations) provides the best match to the observed velocities (r^2 = 0.8 and slope = 0.98, Figure 4.12). For the other methods in Table 4.2, the agreement between observed and predicted $\overline{|u_b|u_b}$ deteriorates as various velocity contributions are neglected (Figure 4.12). As $\overline{|u_b|u_b}$ directly relates to the mean bottom stress, this demonstrates the sensitivity of $\overline{\tau}_b$ to which components of a combined wave-current velocity field are resolved (e.g., as are assumed within different classes on numerical models; Table 4.2).

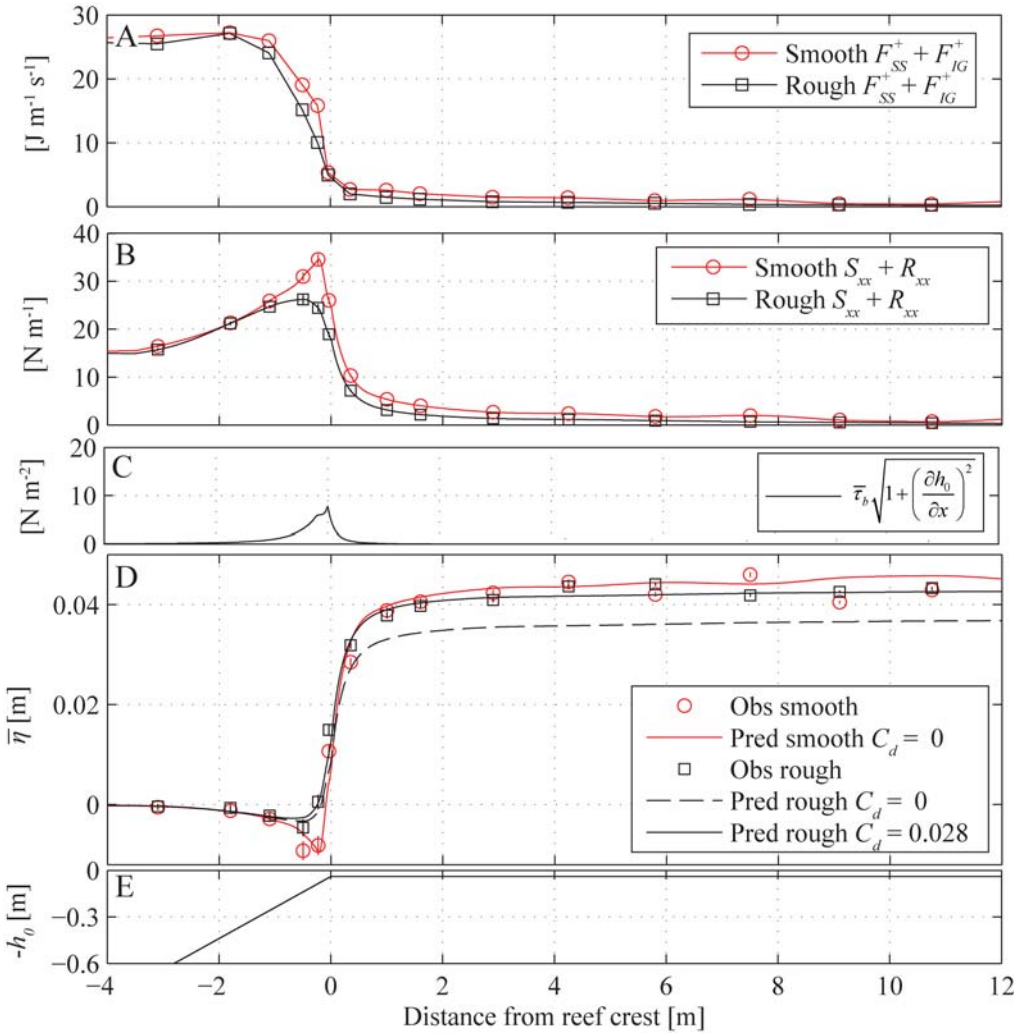

Figure 4.10: (A) Shoreward wave energy flux from sea-swell (F_{SS}^+) and infragravity (F_{IG}^+) waves, (B) radiation stresses (S_{xx} + R_{xx}), and (C) mean bottom stresses ($\bar{\tau}_b$) across (E) the fringing reef profile for Run 4 including ("rough") and without ("smooth") roughness. (D) Radiation stress gradients and mean bottom stresses were used to predicted ("pred") setup ($\bar{\eta}$) via Eq. (4.15) and compared with observations ("obs"). For the smooth run, $\bar{\eta}$ was well predicted without $\bar{\tau}_b$ (i.e., C_d = 0). However, for the rough run $\bar{\eta}$ was underpredicted without $\bar{\tau}_b$ (i.e., C_d = 0) but was well predicted with the estimated $\bar{\tau}_b$ (C_d = 0.028).

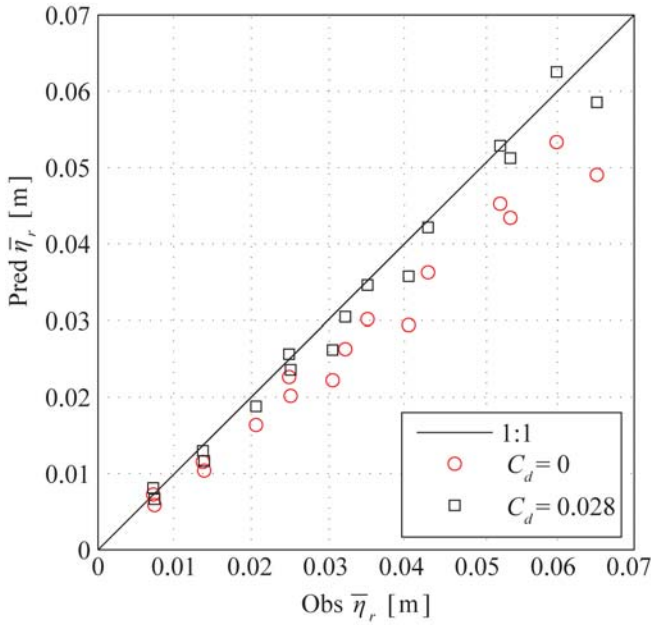

Figure 4.11: Comparison of observed ("obs") and predicted ("pred") wave setup on the reef flat ($\overline{\eta}_r$) for runs with roughness. Wave setup is predicted from observation of radiation stress gradients via Eq. (4.15) neglecting (red circles; C_d = 0) and including (black squares; C_d = 0.028) the predicted mean bottom stress.

Here, we repeat the analysis performed in Figure 4.8 with the various implementations of u_b described in Table 4.2 (Figure 4.13). This allows us to quantitatively assess how neglecting various contributions to u_b affect empirical estimates of the bulk bottom drag coefficient C_d that is the basis for predicting $\overline{\tau}_b$ (Figure 4.13). The range of different classes of numerical models in Table 4.2, can thus be expected to reproduce $\overline{|u_b|u_b}$ with varying accuracies and bias (Figure 4.12). For example, neglecting the role of unsteady wave velocities (u_b') results in a significant underprediction of $\overline{|u_b|u_b}$. Conversely, neglecting velocity nonlinearity (i.e., assuming $Au = Su = 0$) slightly overpredicts $\overline{|u_b|u_b}$ (Figure 4.12). Local inaccuracies in the predicted $\overline{|u_b|u_b}$ can therefore result in both higher and lower predictions of the cross-shore integrated $\overline{|u_b|u_b}$ term (Figure 4.13), which thus requires adjusting C_d in order to balance the sum of the cross-shore integrated pressure and radiation stress gradients per Eq. (4.16) (Figure 4.13; Table 4.2). As a result, C_d estimates using these various approaches range by nearly an order of magnitude (0.027 and 0.23) when applied to the identical dataset (Table 4.2). Neglecting both wave velocities and the wave roller (i.e., $u_b = U_b$ with $M_r = 0$) yielded the smallest estimate of $\overline{|u_b|u_b}$ (Figure 4.12) and hence the

largest C_d = 0.23 (a factor of 8 larger than C_d = 0.028; Figure 4.13; Table 4.2). Neglecting *Au* and *Su* (i.e., $u_b = U_b + u_b'$ with *Su* = *Au* = 0) yielded the smallest C_d = 0.027 (albeit only 4% less than C_d = 0.028; Figure 4.13; Table 4.2). These results highlight a possible non-physical source of variability and uncertainty in C_d based on estimates from various field studies and numerical model applications to coral reefs with large bottom roughness (see Lowe et al. (2009a) and Rosman and Hench (2011) for a review of C_d values reported on coral reefs).

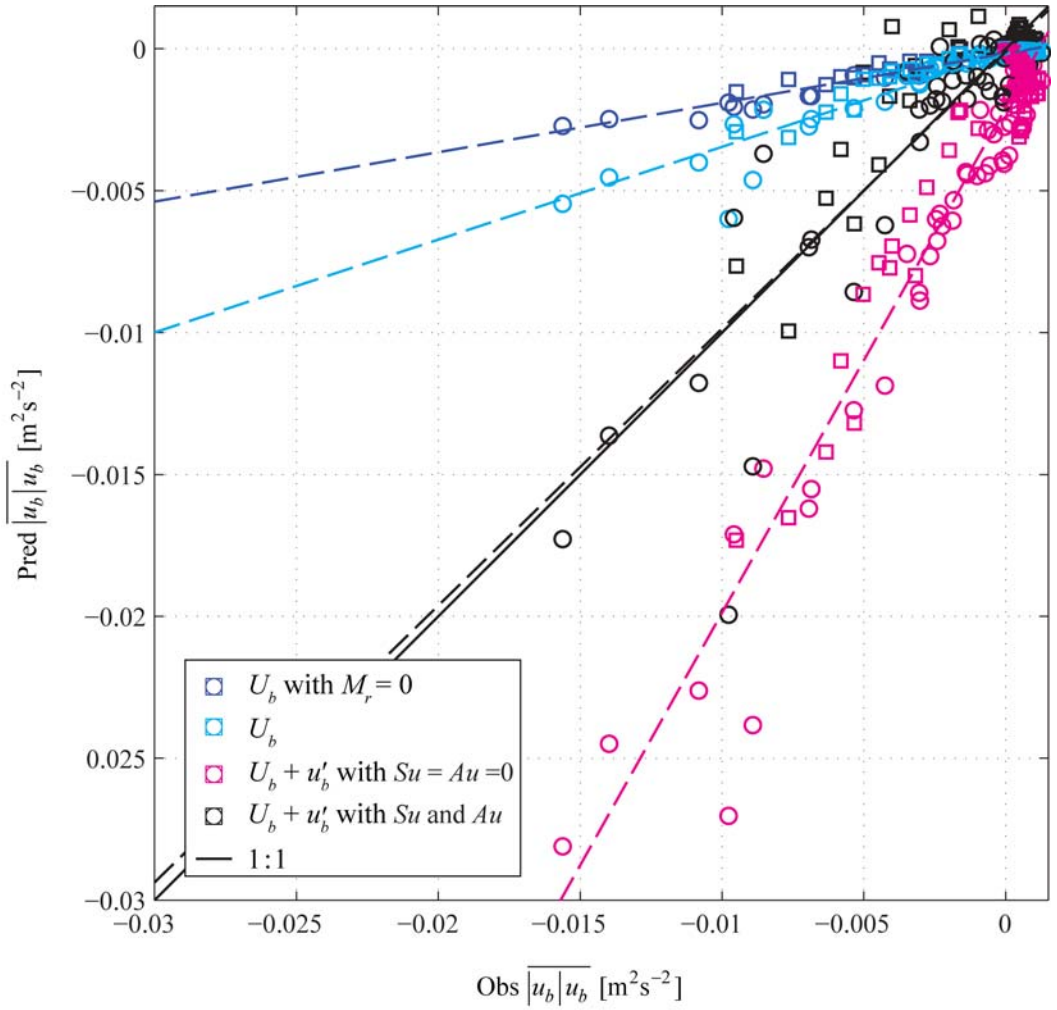

Figure 4.12: Comparisons of the observed ("obs") and predicted ("pred") velocity term $\overline{|u_b|u_b}$ relevant to the calculation of mean bottom stress per Eq. (4.2), for instrument sites with velocity data on the reef flat. Data are shown for both smooth runs (open circles) and with roughness (open squares). Dashed linear least squares trend lines are shown for each method of predicting velocity (Table 4.2). The estimated velocity used in this study (shown in black) includes a near-bottom current (U_b) and a wave component (u_b') with velocity asymmetry (A_u) and skewness (S_u).

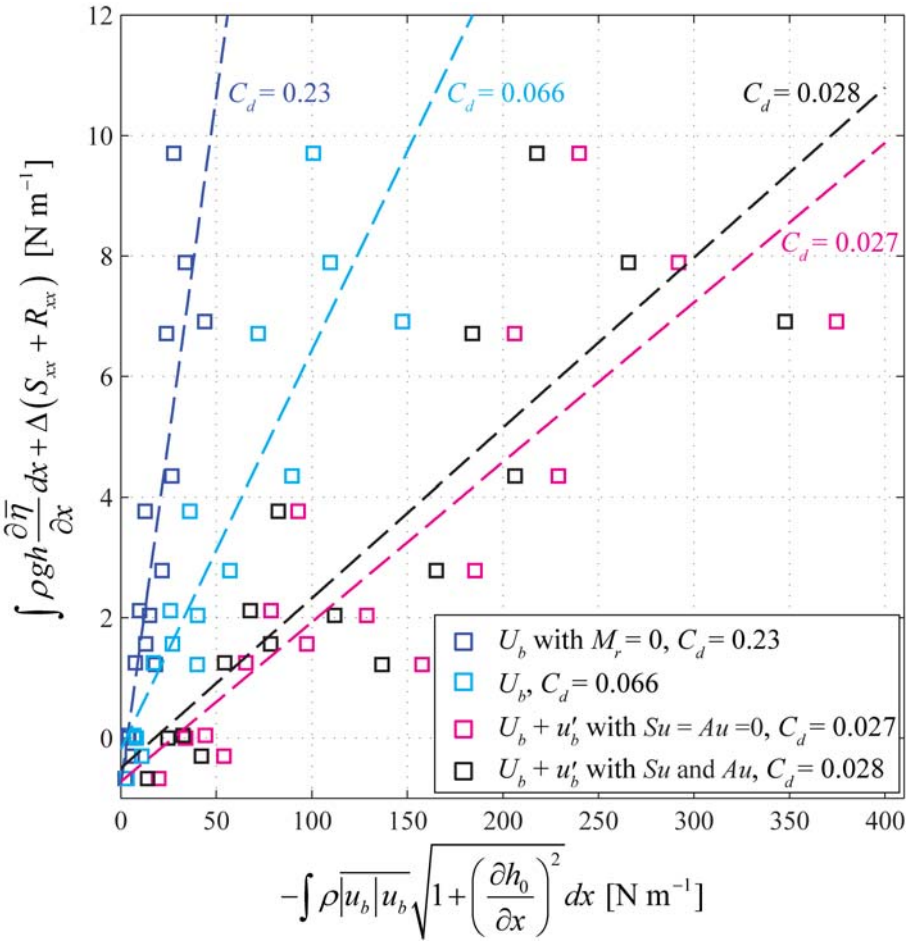

Figure 4.13: The velocity approximations given in Table 4.2 and Figure 4.11 were used to compute the cross-shore integrated time-averaged velocity term in Eq. (4.16) (*x*-axis) and compared with the sum of the cross-shore integrated pressure and radiation stress gradients (*y*-axis) for runs with roughness. Per Eq. (4.16), the linear least squares trend lines (dashed lines) give the estimated bulk bottom drag coefficients (C_d) for each velocity approximation (values given in legend). The estimated velocity used in this study (shown in black) includes a near-bottom current (U_b) and a wave component (u_b') with velocity asymmetry (A_u) and skewness (S_u).

4.5. Discussion

The presence of bottom roughness has two principal effects relevant to the calculation of wave setup:

1) the cross-shore distribution of wave energy is modified, and

2) mean bottom stresses are generated.

In mechanism (1), frictional wave dissipation results from the work done by bottom roughness resistance forces on wave velocities and is parameterized per Eq. (4.10) as being proportional to $\overline{|u_b'^3|}$ and f_w. In mechanism (2), mean bottom stress is generated by the time-averaged resistance forces exerted by the bottom roughness on the combined wave-current velocities, and is parameterized per Eq. (4.2) as being proportional to

$\overline{|u_b|u_b}$ and C_d. Both C_d and f_w are a function of the flow characteristics and the physical scale of bottom roughness (Nielsen 1992). However, f_w is typically found to be an order of magnitude or larger than C_d in the presence of roughness (see Nielsen (1992) for a review). For example, in this study we found $C_d = 0.028$ and $f_w = 0.2$ on average for runs that included roughness.

Through the first mechanism, we found that the inclusion of bottom roughness resulted in the frictional dissipation of wave energy seaward of the breakpoint (Figure 4.3, 4.4, and 4.10A). This redistribution of wave energy (Figure 4.10A) resulted in an average 13% decrease in the H_{rms} at the breakpoint and an average 26% decrease in maximum radiation stresses ($S_{xx} + R_{xx}$) when comparing the rough runs to the smooth runs (shown for Run 4 in Figure 4.10B). As a result, despite the magnitude of the cross-shore integrated radiation stress gradients being 9% larger on average when roughness was included (Figure 4.6), $\overline{\eta}_r$ predicted from the radiation stress gradients (neglecting mean bottom stresses; $C_d = 0$) was on average 18% less for the rough runs compared to the smooth runs (Figure 4.11). However, through the second mechanism, mean bottom stresses for the rough runs increased the predicted $\overline{\eta}_r$ by 16% on average compared to predictions neglecting mean bottom stresses (Figure 4.11). Mechanisms (1) and (2) thus counteracted each another, and despite modifying the setdown and changing the partitioning of radiation stress gradients and mean bottom stresses, the roughness did not considerably alter the final values of setup on the reef flat, which differed less than 10% on average for corresponding rough and smooth runs (Figure 4.3 and 4.5).

Mechanisms (1) and (2) apply generally to nearshore systems governed by Eq. (4.1), including many relatively alongshore-uniform reefs and beaches. However, in contrast to our experimental findings, numerical model predictions (Apotsos et al. 2007; Franklin et al. 2013) have suggested there can be appreciable increases in setup due to bottom roughness principally through mean bottom stresses.

By neglecting frictional wave dissipation in their phase-averaged wave transformation model (i.e., neglecting mechanism (1)) and using a $C_d = 0.028$ in the surf zone to predict mean bottom stresses (hence the same C_d we found in our study), Apotsos et al. (2007) estimated that 30% of the setup response on a sandy beach was due to bottom roughness. Although frictional wave dissipation is commonly assumed to be small compared to wave breaking dissipation on sandy beaches (e.g., Guza and Thornton 1981), wave friction factors (f_w) typically are an order of magnitude larger than the drag coefficient (C_d) used to estimate bottom stresses. Thus given the

C_d = 0.028 used by Apotsos et al. (2007) to predict mean bottom stresses, one would also expect a correspondingly large f_w to have resulted in modifications to the wave field in their study. In our experiments, if we neglected the frictional wave dissipation (mechanism 1) by using the smooth simulations but include mean bottom stresses with C_d = 0.028 (mechanism 2), an average 25% increase in setup is predicted via Eq. (4.15) across all runs, thus comparable to the 30% increase predicted by Apotsos et al. (2007). In another numerical study, Franklin et al. (2013) reported a ~20% increase in setup due to roughness across a fringing reef. They based their study on numerical simulations with a phase-resolving Reynolds-Averaged-Navier-Stokes (RANS) model of the smooth laboratory reef experiments of Demirbilek et al. (2007), and assessed how setup responded to increasing Nikuradse roughness coefficients between 0 and 0.05 m (corresponding to C_d = 0 to ~0.01). Inconsistent with our findings, they predicted that an increase in the roughness coefficient increased the mean bottom stress without resulting in any significant reduction in wave heights at the breakpoint (Franklin et al. 2013). This creates a dynamic similar to Apotsos et al. (2007), where wave forces are held relatively constant and mean bottom stresses are increased.

Ultimately, the accuracy of theoretical and numerical model predictions of setup over rough bottoms will be determined by both the representation of wave transformation (see Buckley et al. 2015a) and the prediction of mechanisms (1) and (2). Although the RANS model used by Franklin et al. (2013) incorporates a more physically-complete description of wave transformation and other dynamics compared to phase-averaged models, a single bulk bottom drag coefficient is applied within these models irrespective of type of flow (i.e., wave versus current). Such an approach does not account for the known differences between f_w and C_d in the presence of roughness (Nielsen 1992). Alternatively, in coupled phase-averaged wave and flow models, f_w and C_d are often independently varied. This was done in a recent numerical study aimed at predicting the hydrodynamic impacts of climate change on coral reefs by Quataert et al. (2015) using the XBeach model (Van Dongeren et al. 2013). In agreement with the mechanisms (1) and (2) discussed above, Quataert et al. (2015) theoretically predicted decreasing setup with increasing f_w (mechanism (1)) and increasing setup with increasing C_d (mechanism (2)). However, Quataert et al. (2015) lacked data to validate their numerical predictions and a physical basis for how f_w and C_d should be related. These numerical studies highlight the need for a more precise method of modelling mechanisms (1) and (2) in both phase-resolving and phase-averaged numerical models.

Although not considered in traditional nearshore models (e.g., Franklin et al. 2013; Quataert et al. 2015), nor explicitly in either Eq. (4.2) or Eq. (4.10), it is the velocity terms $\overline{\left|u'^3\right|}$ and $\overline{|u|u}$ within the "roughness-sublayer" (or "canopy") (not above) that interact with roughness to generate wave dissipation and mean bottom stresses, respectively. For large roughness, previous studies have shown these velocities within the canopy are both reduced compared to those above and that the attenuation is frequency dependent; being most attenuated in a unidirectional flow (Lowe et al. 2005a; Luhar et al. 2010; Zeller et al. 2015). Traditionally, Eq. (4.2) and Eq. (4.10) are cast in terms of the velocities at the top of the roughness (e.g., Apotsos et al. 2007; Franklin et al. 2013; Quataert et al. 2015). As such, in addition to relating the local flow velocities to the resistance forces and the work done by resistance forces, respectively, C_d and f_w must also account for the attenuation of velocities within the canopy that modify the velocities directly interacting with the roughness elements. The attenuation of velocities within canopies has previously been modeled by treating the canopy as a sub-layer using a spatially- and depth-averaged momentum equation (Nepf and Vivoni 2000; Lowe et al. 2005a; Zeller et al. 2015). Canopy flow models have been successfully used to predict the frequency dependent dissipation of wave energy without the need to specify differing empirical coefficients for waves and currents (Lowe et al. 2007; Jadhav et al. 2013). Thus, implementing canopy flow dynamics into existing numerical models, such as those used by Franklin et al. (2013) and Quataert et al. (2015), should improve the representation of mechanisms (1) and (2) and allow for more accurate numerical predictions of setup under different bathymetric configurations, hydrodynamic conditions, and roughness characteristics.

While the present study specifically focuses on how bottom roughness influences setup over a representative fringing coral reef profile, the results are also expected to be broadly applicable to other nearshore systems with large roughness (e.g., due to vegetation, coarse sediment, bedforms). The setup response to roughness will be determined by both the response of the radiation stress gradients (mechanism (1)) and the mean bottom stress (mechanism (2)). In many environments, as was the case here, the two mechanisms may cancel resulting in no appreciable change in setup at the shoreline. However, in other environments the specific physical setting may result in one of the mechanisms becoming more important, resulting in a net setup response to roughness. For example, if our experiments were repeated with a smooth reef slope and rough reef flat, it is expected that setup would be marginally increased as frictional wave dissipation on the reef slope prior to wave breaking would be reduced (i.e.

reducing mechanism (1)). Conversely, in the more likely scenario where spatially-variable coral die-off on a shallow reef flat results in a smoother reef flat but roughness is maintained on the reef slope (e.g., Quataert et al. 2015), it is expected that setup would decrease. In addition, on slopes steeper than the 1:5 slope used here, the setup response to roughness would be expected to increase, as less frictional wave dissipation would be expected to occur prior to wave breaking. Conversely, on milder reef slopes the opposite could occur. On reefs with open lagoons (i.e., barrier reef systems and atolls), as well as other systems where local-continuity does not drive undertows and corresponding offshore directed mean bottom stresses, it is expected that roughness will reduce setup. As hypothesized by Dean and Bender (2006) in the most extreme example and consistent with the mechanisms we observed, setdown rather than setup would be expected for positively skewed waves interacting with roughness to generate onshore directed mean bottom stresses in the absence of wave breaking or an undertow.

4.6. Conclusions

High-resolution laboratory observations were used to investigate the dynamics of wave setup across a fringing reef profile using scaled roughness elements to mimic the large bottom roughness of coral reefs. Sixteen offshore wave and still water level conditions were considered, first with a smooth bottom (results detailed in Buckley et al. 2015a) and then with a staggered array of cubes mimicking the bulk wave frictional dissipation of reefs. In contrast to previous numerical studies (Apotsos et al. 2007; Franklin et al. 2013), setup on the reef flat for corresponding rough and smooth simulations was found to agree with an average difference of only 7%. The similarity in setup was explained through the detailed assessment of the cross-shore mean momentum balances using the observations, which revealed that roughness both modified radiation stress gradients due to frictional wave dissipation, and generated offshore-directed mean bottom stresses. These two mechanisms acted counter to one another, resulting in the observed similarities in setup on the reef flat between rough and smooth runs. When neglecting mean bottom stresses, frictional wave dissipation resulted in radiation stress gradients that were predicted to generate 18% (on average) less setup on the reef flat for rough runs than smooth runs. However, mean bottom stresses for runs with roughness increased the predicted setup by 16% on average compared to neglecting mean bottom stresses. With both frictional wave dissipation and mean bottom stresses accounted for, setup on the reef flat was accurately predicted across all runs with roughness. Comparison of our findings with previous numerical

model predictions highlights the need for an improved framework to predict the setup response to both frictional wave dissipation and mean bottom stresses associated with bottom roughness.

5. General Discussion

5.1. Introduction

The steep slopes and large bottom roughness of coral reefs contrast with the milder slopes and smoother bottoms of sandy beaches where most historical research on surf zone processes has been targeted. These physical characteristics of reefs may thus explicitly violate the underlying assumptions and applicability of existing surf zone models when applied to reef systems. This thesis was directed at examining wave and setup dynamics on steep slope fringing coral reefs. Laboratory datasets provided the high-spatial resolution measurements required to resolve these dynamics, as data is yet to be measured with adequate resolution in the field. The state of surf zone modeling on reefs prior to this thesis was assessed in chapter two by applying three commonly used numerical models to reproduce wave and setup measurements on a steep 1:11 laboratory fringing reef profile from a previous experiment. The cross-shore distribution of wave setup was identified as a key indicator of model performance, as predicting this distribution requires precise reproduction of both the wave field and bottom stresses. In chapter three, the dynamics of wave setup were evaluated with new and much higher spatial-resolution observations collected in a 1:36 scale wave flume with a smooth bottom and characteristic fringing reef profile. Finally in chapter four, the effect of large bottom roughness on wave setup was determined by comparing the results from the smooth laboratory flume experiments with the same experiments conducted including scaled roughness elements.

5.2. Model evaluation (chapter 2)

Focusing on wave breaking and wave setup dynamics, we reviewed three widely used open-source nearshore wave models and assessed their performance in reproducing laboratory observations across a steep fringing reef profile under a range of different conditions. These models were: 1) SWASH (Zijlema et al. 2011); 2) SWAN (Booij et al. 1999); and 3) XBeach (Roelvink et al. 2009). SWASH is a phase-resolving nonlinear shallow water wave model with added non-hydrostatic terms, which solves the time-dependent momentum and conservation equations without including a wave roller term. Wave breaking is modeled implicitly through the use of a shock capturing momentum scheme (Smit et al. 2013). However, a wave steepness criteria controlled by the coefficient α is used to turn off non-hydrostatic terms for breaking waves and enhance breaking dissipation. SWAN is a phase-averaged spectral wave model, which

is either run as a standalone model or coupled with a flow model. As a standalone model, for the calculation of setup SWAN evaluates the time-averaged (mean) momentum without a roller and without mean bottom stress. Linear wave theory radiation stresses are used with the cross-shore distribution of wave energy predicted by evaluating the wave action equations (Bouws et al. 1985), where wave breaking is modeled parametrically. XBeach is a coupled phase-averaged spectral wave model (applied to modeling sea-swell waves) and a nonlinear shallow water model (applied to modeling infragravity waves). Sea-swell waves are modeled with the wave action equations (Bouws et al. 1985). Infragravity waves and wave setup are modeled with time-dependent momentum and conservation equations evaluated on the wave group time-scale (Roelvink et al. 2009).

Previously, Lowe et al. (2009b), Hoeke et al. (2011), Storlazzi et al. (2011), Filipot and Cheung (2012) applied SWAN and Pomeroy et al. (2012) and Van Dongeren et al. (2013) applied XBeach to field studies of coral reefs. Zijlema (2012) and Torres-Freyermuth et al. (2012) applied SWASH to laboratory and field datasets of coral reefs. However, little validation of these models had been conducted for application to coral reefs, and most importantly, no inter-comparison of these models had been performed. In this thesis, we consistently applied each model to the 29 laboratory test conditions of Demirbilek and Nwogu (2007), which incorporated a wide range of incident spectral wave conditions and still water levels. Models were assessed for their performance in predicting sea-swell wave heights, infragravity wave heights, wave spectra, and setup at 5 locations across the fringing reef profile.

Simulations were performed with the “recommended” (“default”) empirical coefficients as documented for each model. This yielded on average 12%, 22%, and 40% errors in the combined sea-swell and infragravity *rms* wave heights on the reef flat and on average 17%, 61%, and 13% errors in wave setup on the reef flat for SWASH, SWAN, and XBeach, respectively. Tuning the models to best match sea-swell *rms* wave heights on the reef flat yielded on average 9%, 23%, and 6% errors in the combined sea-swell and infragravity *rms* wave heights on the reef flat and on average 18%, 39%, and 16% errors in wave setup on the reef flat for SWASH, SWAN, and XBeach, respectively. These errors are viewed as reasonable considering that the steep (1:11) reef slope explicitly violates the mild-slope and other fundamental assumptions that underpin the numerical models. However, a partial explanation of the good agreement with observations, may be owing to the tuning of empirical coefficients and hence may not be physically meaningful. Indeed, in many cases tuning model parameters to best

reproduce the observed wave height decay resulted in a reduction in the accuracy of wave setup predictions, which indicates a fundamental breakdown in the theoretical relationship between the predicted radiation stress gradients and the observed wave setup. However, as detailed surf zone measurements were not available, it was not possible to further evaluate the details of wave and setup dynamics and the source of this discrepancy.

5.3. Wave setup dynamics on a smooth reef profile (chapter 3)

The general lack of detailed surf zone measurements on reefs was rectified by conducting the high-resolution laboratory experiment detailed in chapters three and four. In these chapters, we utilized new datasets to evaluate the time-averaged cross-shore momentum equation from observations of water levels and velocities, rather than the traditional approach of using empirical models to predict wave transformation through the surf zone.

These high-resolution laboratory observations were used to investigate the dynamics of wave setdown and setup across the steeply-sloping fringing reef profile. The one-dimensional profile with a smooth bed reduced the cross-shore mean momentum equation to a balance between the pressure and radiation stress gradients. This balance was evaluated using observations at seventeen locations across the reef profile for sixteen offshore wave and water level conditions. Radiation stress gradients calculated from observations using linear wave theory under predicted setdown (8 of 16 runs; by up to 77%) and setup (12 of 16 runs; by up to 31%), with the inaccuracy increasing with increased offshore wave height. For the twelve runs where setup was under predicted (all having $H_{rms,0} \geq 2.2$ m in field scale), including a wave roller in the estimation of radiation stress gradients reduced the under prediction of setup from 21% to 3% on average. The wave roller accounts for an initial transfer of potential energy to kinetic energy during wave breaking thereby shifting the dissipation shoreward in line with pressure gradient observations. Evaluating the wave roller required a single parameter, the wave roller inclination angle, which was found to be linearly related to our estimates of the wave front inclination angle derived from the wave gauge observations. This relationship, combined with the improved agreement with the observed setdown/ setup profiles, suggests a physical basis for the wave roller. The wave roller was found to be most important for relatively large incident wave cases; therefore, under the conditions most critical to coastal hazard assessment.

5.4. Wave setup dynamics on a reef profile with large roughness (chapter 4)

High-resolution laboratory observations were used to investigate the dynamics of wave setup across a fringing reef profile using scaled roughness elements to mimic the large bottom roughness of coral reefs. Sixteen offshore wave and still water level conditions were considered, first with a smooth bottom (as detailed in chapter three) and then repeated with a staggered array of cubes mimicking the bulk wave frictional dissipation of reefs. In contrast to previous numerical studies (Apotsos et al. 2007; Franklin et al. 2013), setup on the reef flat for corresponding rough and smooth simulations was found to agree with an average difference of only 7%. The similarity in setup was explained through the detailed assessment of the cross-shore mean momentum balances using the observations. This analysis revealed that the roughness both modified radiation stress gradient profiles due to frictional wave dissipation and generated offshore-directed mean bottom stresses. These two mechanisms acted counter to one another, resulting in the observed similarities in setup on the reef flat between rough and smooth runs. When neglecting mean bottom stresses, frictional wave dissipation resulted in radiation stress gradient profiles that were predicted to generate 18% (on average) less setup on the reef flat for rough runs than smooth runs. However, mean bottom stresses for runs with roughness increased the predicted setup by 16% on average compared to neglecting mean bottom stresses. With both frictional wave dissipation and mean bottom stresses accounted for, setup on the reef flat was accurately predicted across all runs with roughness. Comparison of our findings with previous numerical model predictions highlights the need for an improved framework to predict the setup response to both frictional wave dissipation and mean bottom stresses associated with bottom roughness.

5.5. Conclusions

The results from this thesis support the following main conclusions:

1. Wave setup is highly sensitive to the details of the bathymetry, radiation stresses, and mean bottom stresses.
2. Although traditional nearshore models (e.g., SWAN, XBeach, SWASH used in chapter two) may accurately reproduce some of the hydrodynamics on reefs, there are still deficiencies in the representation of wave transformation and bottom roughness.

3. Accurate modelling of radiation stresses in the surf zone using linear wave theory requires the inclusion of an additional source of radiation stress from a wave roller to account for inequality between potential and kinetic energy within breaking waves.
4. Large roughness alters both radiation stresses and mean bottom stresses, both of which are important to the prediction of wave setup. As shown for a representative fringing reef profile in chapter four, in certain physical settings large changes in roughness may result in little net change to setup as frictional wave dissipation effects on radiation stress gradients and off-shore directed mean bottom stresses act counter to one another in the generation of setup.

5.6. Future work

This thesis has led to the following recommendations for future research:

1. Analysis in chapters three and four revealed the importance of high-spatial resolution in evaluating surf zone gradients. Video analysis of the water surface is recommended to further increase the spatial resolution of observations within the surf zone region.
2. In chapter three, the contribution from wave rollers to radiation stress was found to improve the agreement between the observed and predicted setup profiles. Wave roller theory indicates that the velocity field within breaking waves is enhanced compared to non-breaking waves and linear wave theory. New experimental studies using particle image velocimetry of the surf zone region is recommended to further investigate this finding, including how the partitioning of potential versus kinetic energy varies within the surf zone.
3. In chapter four, canopy flow dynamics are discussed as a method of improving the representation of wave frictional dissipation and mean bottom stress within numerical models (e.g., those used in chapter two). Implementation and validation of such a model against the dataset detailed in chapters three and four is recommended. This should allow for more accurate numerical predictions of setup under different bathymetric configurations, hydrodynamic conditions, and roughness characteristics.
4. Targeted field studies including detailed surf zone observations are recommended to build on the findings of this thesis, including extension to more complex reef systems.

References

Alsina, J. M., and T. E. Baldock, 2007: Improved representation of breaking wave energy dissipation in parametric wave transformation models. *Coastal Eng.*, **54,** 765-769.

Alvarez-Filip, L., N. K. Dulvy, J. A. Gill, I. M. Cote, and A. R. Watkinson, 2009: Flattening of Caribbean coral reefs: region-wide declines in architectural complexity. *P R Soc B*, **276,** 3019-3025.

Apotsos, A., B. Raubenheimer, S. Elgar, and R. T. Guza, 2008: Testing and calibrating parametric wave transformation models on natural beaches. *Coastal Eng.*, **55,** 224-235.

Apotsos, A., B. Raubenheimer, S. Elgar, R. T. Guza, and J. A. Smith, 2007: Effects of wave rollers and bottom stress on wave setup. *J. Geophys. Res.*, **112,** C02003.

Baldock, T., P. Holmes, S. Bunker, and P. Van Weert, 1998a: Cross-shore hydrodynamics within an unsaturated surf zone *Coastal Eng.*, **34,** 173-196

Baldock, T. E., P. Holmes, S. Bunker, and P. Van Weert, 1998b: Cross-shore hydrodynamics within an unsaturated surf zone. *Coastal Eng.*, **34,** 173-196.

Baldock, T. E., A. Golshani, D. P. Callaghan, M. I. Saunders, and P. J. Mumby, 2014: Impact of sea-level rise and coral mortality on the wave dynamics and wave forces on barrier reefs. *Mar. Pollut. Bull.*, **83,** 155-164.

Barbier, E. B., S. D. Hacker, C. Kennedy, E. W. Koch, A. C. Stier, and B. R. Silliman, 2011: The value of estuarine and coastal ecosystem services. *Ecol Monogr*, **81,** 169-193.

Battjes, J. A., 1972: Radiation Stresses in Short-Crested Waves. *J. Mar. Res.*, **30**.

——, 1974: Surf Similarity. *Coastal Engineering Proceedings*.

——, 1988: Surf-Zone Dynamics. *Annu Rev Fluid Mech*, **20,** 257-293.

Battjes, J. A., and J. P. F. M. Janssen, 1978: Energy loss and set-up due to breaking of random waves. *Proc. 16th Int. Conf. Coastal Engineering, ASCE***,** 569-587.

Battjes, J. A., and M. J. F. Stive, 1985: Calibration and Verification of a Dissipation Model for Random Breaking Waves. *J. Geophys. Res.*, **90,** 9159-9167.

Becker, J. M., M. A. Merrifield, and M. Ford, 2014: Water level effects on breaking wave setup for Pacific Island fringing reefs. *J. Geophys. Res.*, **119,** 914-932.

Belcher, S. E., N. Jerram, and J. C. R. Hunt, 2003: Adjustment of a turbulent boundary layer to a canopy of roughness elements. *J. Fluid Mech.*, **488,** 369-398.

Birkemeier, W. A., and E. B. Thornton, 1994: The DUCK94 nearshore field experiment. *Coastal Dynamics***,** 815-821.

Bonmarin, P., 1989: Geometric-Properties of Deep-Water Breaking Waves. *J. Fluid Mech.*, **209,** 405-433.

Booij, N., R. C. Ris, and L. H. Holthuijsen, 1999: A third-generation wave model for coastal regions 1. Model description and validation. *J. Geophys. Res.*, **104,** 7649-7666.

Bouws, E., H. Gunther, W. Rosenthal, and C. L. Vincent, 1985: Similarity of the Wind Wave Spectrum in Finite Depth Water .1. Spectral Form. *J. Geophys. Res.*, **90,** 975-986.

Bowen, A. J., D. L. Inman, and V. P. Simmons, 1968: Wave Set-down and Set-Up. *J. Geophys. Res.*, **73,** 2569-2577.

Buckley, M., R. Lowe, and J. Hansen, 2014: Evaluation of nearshore wave models in steep reef environments. *Ocean Dyn.*, **64,** 847-862.

Buckley, M., R. Lowe, J. Hansen, and A. Van Dongeren, 2015a: Dynamics of wave setup over a steeply-sloping fringing reef. *J. Phys. Oceanogr.*, **45**.

——, 2015b: Wave setup over a fringing reef with large bottom roughness. *J. Phys. Oceanogr.*, **In review**.

Cavaleri, L., and Coauthors, 2007: Wave modelling – The state of the art. *Prog. Oceanogr.*, **75,** 603-674.

Chamberlain, J. A., and R. R. Graus, 1975: Water-Flow and Hydromechanical Adaptations of Branched Reef Corals. *Bull. Mar. Sci.*, **25,** 112-125.

Cienfuegos, R., E. Barthélemy, and P. Bonneton, 2010: Wave-breaking model for Boussinesq-type equations including roller effects in the mass conservation equation. *Journal of Waterway, Port, Coastal and Ocean Engineering*, **136,** 10-26.

Dally, W. R., and C. A. Brown, 1995: A modeling investigation of the breaking wave roller with application to cross-shore currents. *J. Geophys. Res.*, **100,** 24873-24883.

Dean, R. G., and R. A. Dalrymple, 1991: Water Wave Mechanics for Engineers and Scientist. *World Scientific*.

Dean, R. G., and C. J. Bender, 2006: Static wave setup with emphasis on damping effects by vegetation and bottom friction. *Coastal Eng.*, **53,** 149-156.

Demirbilek, Z., and O. G. Nwogu, 2007: Boussinesq Modeling of Wave Propagation and Runup over Fringing Coral Reefs, Model Evaluation Report. *Data Report. ERDC/CHL TR-07-12, Coastal and Hydraulics Laboratory*

Demirbilek, Z., O. G. Nwogu, and D. L. Ward, 2007: Laboratory Study of Wind Effect on Runup over Fringing Reefs, Report 1: Data Report. *ERDC/CHL TR-07-4, Coastal and Hydraulics Laboratory*.

Doering, J. C., and A. J. Bowen, 1995: Parametrization of Orbital Velocity Asymmetries of Shoaling and Breaking Waves Using Bispectral Analysis. *Coastal Eng.*, **26,** 15-33.

Duncan, J. H., 1981: An Experimental Investigation of Breaking Waves Produced by a Towed Hydrofoil. *Proceedings of the Royal Society of London Series a-Mathematical Physical and Engineering Sciences*, **377,** 331-&.

Elgar, S., T. H. C. Herbers, M. Okihiro, J. Oltman-Shay, and R. T. Guza, 1992: Observations of Infragravity Waves. *J. Geophys. Res.*, **97,** 15573-15577.

Elgar, S., R. T. Guza, W. C. O'Reilly, B. Raubenheimer, and T. H. C. Herbers, 2001: Wave energy and direction observed near a pier. *J Waterw Port C-Asce*, **127,** 2-6.

Emery, K. O., and G. G. Kuhn, 1982: Sea cliffs: Their processes, profiles, and classification. *Geol. Soc. Am. Bull.*, **93,** 644-654.

Eslami Arab, S., A. van Dongeren, and P. Wellens, 2012: Studying the effect of linear refraction on low-frequency wave propagation (physical and numerical study). *Coastal Engineering Proceedings*.

Falter, J. L., M. J. Atkinson, and M. A. Merrifield, 2004: Mass transfer limitation of nutrient uptake by a wave-dominated reef flat community. *Limnol. Oceanogr.*, **49,** 1820-1831.

Falter, J. L., R. J. Lowe, Z. L. Zhang, and M. McCulloch, 2013: Physical and Biological Controls on the Carbonate Chemistry of Coral Reef Waters: Effects of Metabolism, Wave Forcing, Sea Level, and Geomorphology. *Plos One*, **8**.

Faria, A. F. G., E. B. Thornton, T. C. Lippmann, and T. P. Stanton, 2000: Undertow over a barred beach. *J Geophys Res-Oceans*, **105,** 16999-17010.

Faria, A. F. G., E. B. Thornton, T. P. Stanton, C. V. Soares, and T. C. Lippmann, 1998: Vertical profiles of longshore currents and related bed shear stress and bottom roughness. *J. Geophys. Res.*, **103,** 3217-3232.

Feddersen, F., 2004: Effect of wave directional spread on the radiation stress: comparing theory and observations. *Coastal Eng.*, **51,** 473-481.

Feddersen, F., and R. T. Guza, 2003: Observations of nearshore circulation: Alongshore uniformity. *J Geophys Res-Oceans*, **108,** 6-1–6-10.

Feddersen, F., R. T. Guza, S. Elgar, and T. H. C. Herbers, 2000: Velocity moments in alongshore bottom stress parameterizations. *J. Geophys. Res.*, **105,** 8673-8686.

Feddersen, F., E. L. Gallagher, R. T. Guza, and S. Elgar, 2003: The drag coefficient, bottom roughness, and wave-breaking in the nearshore. *Coastal Eng.*, **48,** 189-195.

Filipot, J.-F., and K. F. Cheung, 2012: Spectral wave modeling in fringing reef environments. *Coastal Eng.*, **67,** 67-79.

Franklin, G., I. Marino-Tapia, and A. Torres-Freyermuth, 2013: Effects of reef roughness on wave setup and surf zone currents. *J. Coast. Res.*, 2005-2010.

Gerritsen, F., 1980: Wave attenuation and wave set-up on a coastal reef. *Proceedings of the International Conference on Coastal Engineering; No 17 (1980): Proceedings of 17th Conference on Coastal Engineering, Sydney, Australia, 1980.*

Gourlay, M. R., 1994: Wave transformation on a coral reef. *Coastal Eng.*, **23,** 17-42.

——, 1996a: Wave set-up on coral reefs. 2. set-up on reefs with various profiles. *Coastal Eng.*, **28,** 17-55.

——, 1996b: Wave set-up on coral reefs. 1. Set-up and wave-generated flow on an idealised two dimensional horizontal reef. *Coastal Eng.*, **27,** 161-193.

Gourlay, M. R., and G. Colleter, 2005: Wave-generated flow on coral reefs—an analysis for two-dimensional horizontal reef-tops with steep faces. *Coastal Eng.*, **52,** 353-387.

Govender, K., G. P. Mocke, and M. J. Alport, 2002: Video-imaged surf zone wave and roller structures and flow fields. *J. Geophys. Res.*, **107,** 3071 3079 3071-3021.

Govender, K., H. Michallet, M. J. Alport, U. Pillay, G. P. Mocke, and M. Mory, 2009: Video DCIV measurements of mass and momentum fluxes and kinetic energies in laboratory waves breaking over a bar. *Coastal Eng.*, **56,** 876-885.

Grant, W. D., and O. S. Madsen, 1979: Combined Wave and Current Interaction with a Rough Bottom. *J. Geophys. Res.*, **84,** 1797-1808.

Grilli, S. T., I. A. Svendsen, and R. Subramanya, 1997: Breaking criterion and characteristics for solitary waves on slopes. *J Waterw Port C-Asce*, **123,** 102-112.

Guza, R. T., and E. B. Thornton, 1980: Local and Shoaled Comparisons of Sea-Surface Elevations, Pressures, and Velocities. *J. Geophys. Res.*, **85,** 1524-1530.

——, 1981: Wave Set-up on a Natural Beach. *J. Geophys. Res.*, **86,** 4133-4137.

Hamm, L., P. A. Madsen, and D. H. Peregrine, 1993: Wave transformation in the nearshore zone: A review. *Coastal Eng.*, **21,** 5-39.

Hasselmann, D. E., M. Dunckel, and J. A. Ewing, 1980: Directional Wave Spectra Observed during JONSWAP 1973. *J. Phys. Oceanogr.*, **10,** 1264-1280.

Hearn, C. J., 1999: Wave-breaking hydrodynamics within coral reef systems and the effect of changing relative sea level. *J. Geophys. Res.*, **104,** 30007-30019.

Henderson, S. M., R. T. Guza, S. Elgar, T. H. C. Herbers, and A. J. Bowen, 2006: Nonlinear generation and loss of infragravity wave energy. *J Geophys Res-Oceans*, **111**.

Hoeke, R., C. Storlazzi, and P. Ridd, 2011: Hydrodynamics of a bathymetrically complex fringing coral reef embayment: Wave climate, in situ observations, and wave prediction. *J. Geophys. Res.*, **116,** C04018.

Huang, Z. C., L. Lenain, W. K. Melville, J. H. Middleton, B. Reineman, N. Statom, and R. M. McCabe, 2012: Dissipation of wave energy and turbulence in a shallow coral reef lagoon. *J. Geophys. Res.*, **117,** C03015.

Hughes, T. P., and Coauthors, 2003: Climate change, human impacts, and the resilience of coral reefs. *Science*, **301,** 929-933.

Iribarren, C. R., and C. Nogales, 1949: Protection des Ports. *XVIIth International Navigation Congress, Section II, Communication***,** 31–80.

Iwata, K., and T. Tomita, 1992: Variation of potential and kinetic wave energy in surf zone. *In: Proc. 23rd Int. Conf. Coastal Eng., Venice. ASCE, pp. 336-349*.

Jadhav, R. S., Q. Chen, and J. M. Smith, 2013: Spectral distribution of wave energy dissipation by salt marsh vegetation. *Coastal Eng.*, **77,** 99-107.

Janssen, T. T., and J. A. Battjes, 2007: A note on wave energy dissipation over steep beaches. *Coastal Eng.*, **54,** 711-716.

Jonsson, I. G., 1966: Wave boundary layers and friction factors, paper presented at Tenth Conference on Coastal Engineering. *Am. Soc. of Civ. Eng., Tokyo*.

Lentz, S., and B. Raubenheimer, 1999: Field observations of wave setup. *J. Geophys. Res.*, **104,** 25867-25875.

Lentz, S. J., M. Fewings, P. Howd, J. Fredericks, and K. Hathaway, 2008: Observations and a Model of Undertow over the Inner Continental Shelf. *J. Phys. Oceanogr.*, **38,** 2341-2357.

Longuet-Higgins, M. S., 1970: Longshore Currents Generated by Obliquely Incident Sea Waves .1. *J. Geophys. Res.*, **75,** 6778-&.

——, 2005: On wave set-up in shoaling water with a rough sea bed. *J. Fluid Mech.*, **527,** 217-234.

Longuet-Higgins, M. S., and R. W. Stewart, 1962: Radiation stress and mass transport in gravity waves, with application to. *J. Fluid Mech.*, **13,** 481-504.

Longuet-Higgins, M. S., and R. w. Stewart, 1964: Radiation stresses in water waves; a physical discussion, with applications. *Deep Sea Research and Oceanographic Abstracts*, **11,** 529-562.

Lowe, R. J., and J. L. Falter, 2015: Oceanic Forcing of Coral Reefs. *Annual Review of Marine Science*, **7,** 43-66.

Lowe, R. J., J. R. Koseff, and S. G. Monismith, 2005a: Oscillatory flow through submerged canopies: 1. Velocity structure. *J. Geophys. Res.*, **110,** C10016.

Lowe, R. J., C. Hart, and C. B. Pattiaratchi, 2010: Morphological constraints to wave-driven circulation in coastal reef-lagoon systems: A numerical study. *J. Geophys. Res.*, **115,** C09021.

Lowe, R. J., J. L. Falter, S. G. Monismith, and M. J. Atkinson, 2009a: Wave-driven circulation of a coastal reef-lagoon system. *J. Phys. Oceanogr.*, **39,** 873-893.

Lowe, R. J., J. L. Falter, S. G. Monismith, and M. J. Atkinson, 2009b: A numerical study of circulation in a coastal reef-lagoon system. *J. Geophys. Res.*, **114,** C06022.

Lowe, R. J., J. L. Falter, J. R. Koseff, S. G. Monismith, and M. J. Atkinson, 2007: Spectral wave flow attenuation within submerged canopies: Implications for wave energy dissipation. *J. Geophys. Res.*, **112,** C05018.

Lowe, R. J., U. Shavit, J. L. Falter, J. R. Koseff, and S. G. Monismith, 2008: Modeling flow in coral communities with and without waves: A synthesis of porous media and canopy flow approaches. *Limnol. Oceanogr.*, **53,** 2668-2680.

Lowe, R. J., J. L. Falter, M. D. Bandet, G. Pawlak, M. J. Atkinson, S. G. Monismith, and J. R. Koseff, 2005b: Spectral wave dissipation over a barrier reef. *J. Geophys. Res.*, **110,** C04001.

Luhar, M., S. Coutu, E. Infantes, S. Fox, and H. Nepf, 2010: Wave-induced velocities inside a model seagrass bed. *J Geophys Res-Oceans*, **115,** C12005.

Macdonald, R. W., 2000: Modelling the mean velocity profile in the urban canopy layer. *Bound-Lay Meteorol*, **97,** 25-45.

Madsen, P. A., O. R. Sørensen, and H. A. Schäffer, 1997: Surf zone dynamics simulated by a Boussinesq type model. Part I. Model description and cross-shore motion of regular waves. *Coastal Eng.*, **32,** 255-287.

Mansard, E. P. D., and E. R. Funke, 1980: Measurement of incident and reflected spectra using a least squares method. *17th International Conference on Coastal Engineering, Sydney, Australia***,** pp. 95–96.

Massel, S. R., and M. R. Gourlay, 2000: On the modelling of wave breaking and set-up on coral reefs. *Coastal Eng.*, **39,** 1-27.

Mei, C. C., 2005: Theory and applications of ocean surface waves. *World Sci., Singapore*.

Moberg, F., and C. Folke, 1999: Ecological goods and services of coral reef ecosystems. *Ecol Econ*, **29,** 215-233.

Monismith, S. G., 2007: Hydrodynamics of coral reefs. *Annu Rev Fluid Mech*, Annual Reviews, 37-55.

Monismith, S. G., L. M. M. Herdman, S. Ahmerkamp, and J. L. Hench, 2013: Wave Transformation and Wave-Driven Flow across a Steep Coral Reef. *J. Phys. Oceanogr.*, **43,** 1356-1379.

Monismith, S. G., J. S. Rogers, D. Koweek, and R. B. Dunbar, 2015: Frictional wave dissipation on a remarkably rough reef. *Geophys. Res. Lett.*, **42,** 4063-4071.

Murphy, A. H., and E. S. Epstein, 1989: Skill Scores and Correlation Coefficients in Model Verification. *Monthly Weather Review*, **117,** 572-582.

Nairn, R. B., 1990: Prediction of cross-shore sediment transport and beach profile evolution, Civil Eng, Imperial College, 391 pp.

Nelson, R. C., 1994: Depth limited design wave heights in very flat regions. *Coastal Eng.*, **23,** 43-59.

——, 1996: Hydraulic roughness of coral reef platforms. *Appl. Ocean Res.*, **18,** 265-274.

Nelson, R. C., and E. J. Lesleighter, 1985: Breaker height attenuation over platform coral reefs. *In: Preprints 1985 Australasian Conf. on Coastal and Ocean Eng., Christchurch*.

Nepf, H. M., and E. R. Vivoni, 2000: Flow structure in depth-limited, vegetated flow. *J Geophys Res-Oceans*, **105,** 28547-28557.

Nielsen, P., 1992: Coastal bottom boundary layers and sediment transport. *World Sci., Singapore*.

Okayasu, A., T. Shibayama, and N. Mimura, 1986: Velocity Field Under Plunging Waves. *Coastal Engineering Proceedings*.

Pequignet, A. C. N., J. M. Becker, and M. A. Merrifield, 2014: Energy transfer between wind waves and low-frequency oscillations on a fringing reef, Ipan, Guam. *J Geophys Res-Oceans*, **119,** 6709-6724.

Péquignet, A. C. N., J. M. Becker, M. A. Merrifield, and J. Aucan, 2009: Forcing of resonant modes on a fringing reef during tropical storm Man-Yi. *Geophys. Res. Lett.*, **36**.

Phillips, O. M., 1977: The Dynamics of the Upper Ocean. Vol. 2. *Cambridge Monographs on Mechanics and Applied Mathematics, Cambridge University Press*, **2**.

Pomeroy, A., R. Lowe, G. Symonds, A. Van Dongeren, and C. Moore, 2012: The dynamics of infragravity wave transformation over a fringing reef. *J. Geophys. Res.*, **117**.

Quataert, E., C. Storlazzi, A. van Rooijen, O. Cheriton, and A. van Dongeren, 2015: The influence of coral reefs and climate change on wave-driven flooding of tropical coastlines. *Geophys. Res. Lett.***,** n/a-n/a.

Raubenheimer, B., 2002: Observations and predictions of fluid velocities in the surf and swash zones. *J. Geophys. Res.*, **107**.

Raubenheimer, B., R. T. Guza, and S. Elgar, 1996: Wave transformation across the inner surf zone. *J. Geophys. Res.*, **101,** 25589-25597.

——, 2001: Field observations of wave-driven setdown and setup. *J. Geophys. Res.*, **106,** 4629-4638.

Reniers, A. J. H. M., and J. A. Battjes, 1997: A laboratory study of longshore currents over barred and non-barred beaches. *Coastal Eng.*, **30,** 1-21.

Roberts, H. H., S. P. Murray, and J. N. Suhayda, 1975: Physical processes in a fringing reef system. *J. Mar. Res.*, **33,** 233-260.

Roelvink, D., A. Reniers, A. van Dongeren, J. van Thiel de Vries, R. McCall, and J. Lescinski, 2009: Modelling storm impacts on beaches, dunes and barrier islands. *Coastal Eng.*, **56,** 1133-1152.

Roelvink, J. A., 1993: Dissipation in random wave groups incident on a beach. *Coastal Eng.*, **19,** 127-150.

Rosman, J. H., and J. L. Hench, 2011: A framework for understanding drag parameterizations for coral reefs. *J Geophys Res-Oceans*, **116,** C08025.

Ruessink, B. G., D. J. R. Walstra, and H. N. Southgate, 2003: Calibration and verification of a parametric wave model on barred beaches. *Coastal Eng.*, **48,** 139-149.

Ruessink, B. G., G. Rarnaekers, and L. C. van Rijn, 2012: On the parameterization of the free-stream non-linear wave orbital motion in nearshore morphodynamic models. *Coastal Eng.*, **65,** 56-63.

Ruessink, B. G., J. R. Miles, F. Feddersen, R. T. Guza, and S. Elgar, 2001: Modeling the alongshore current on barred beaches. *J. Geophys. Res.*, **106,** 22451-22463.

Schäffer, H. A., P. A. Madsen, and R. Deigaard, 1993: A Boussinesq model for waves breaking in shallow water. *Coastal Eng.*, **20,** 185-202.

Seelig, W. N., 1983: Laboratory study of reef- lagoon system hydraulics. *Journal of Waterway, Port, Coastal & Ocean Engineering - ASCE*, **109,** 380-391.

Sheppard, C., D. J. Dixon, M. Gourlay, A. Sheppard, and R. Payet, 2005: Coral mortality increases wave energy reaching shores protected by reef flats: Examples from the Seychelles. *Estuarine Coastal and Shelf Science*, **64,** 223-234.

Sheremet, A., J. M. Kaihatu, S. F. Su, E. R. Smith, and J. M. Smith, 2011: Modeling of nonlinear wave propagation over fringing reefs. *Coastal Eng.*, **58,** 1125-1137.

Skotner, C., and C. J. Apelt, 1999: Application of a Boussinesq model for the computation of breaking waves Part 2: Wave-induced setdown and setup on a submerged coral reef. *Ocean Eng*, **26,** 927-947.

Smit, P., M. Zijlema, and G. Stelling, 2013: Depth-induced wave breaking in a non-hydrostatic, near-shore wave model. *Coastal Eng.*, **76,** 1-16.

Smith, J. A., 2006: Wave-current interactions in finite depth. *J. Phys. Oceanogr.*, **36,** 1403-1419.

Stansby, P. K., and T. Feng, 2004: Surf zone wave overtopping a trapezoidal structure: 1-D modelling and PIV comparison. *Coastal Eng.*, **51,** 483-500.

Stephens, S. A., and D. L. Ramsay, 2014: Extreme cyclone wave climate in the Southwest Pacific Ocean: Influence of the El Nino Southern Oscillation and projected climate change. *Global Planet. Change*, **123,** 13-26.

Stive, M. J. F., and H. G. Wind, 1982: A Study of Radiation Stress and Set-up in the Nearshore Region. *Coastal Eng.*, **6,** 1-25.

Stive, M. J. F., and H. J. De Vriend, 1994: Shear Stresses and Mean Flow in Shoaling and Breaking Waves. *Coastal Engineering Proceedings*.

Storlazzi, C. D., E. Elias, M. E. Field, and M. K. Presto, 2011: Numerical modeling of the impact of sea-level rise on fringing coral reef hydrodynamics and sediment transport. *Coral Reefs*, **30,** 83-96.

Svendsen, I. A., 1984a: Mass flux and undertow in a surf zone. *Coastal Eng.*, **8,** 347-365.

——, 1984b: Wave Heights and Set-up in a Surf Zone. *Coastal Eng.*, **8,** 303-329.

——, 2006: Introduction to Nearshore Hydrodynamics. *World Sci., Singapore*.

Svendsen, I. A., and U. Putrevu, 1993: Surf Zone Wave Parameters from Experimental-Data. *Coastal Eng.*, **19,** 283-310.

Symonds, G., K. P. Black, and I. R. Young, 1995: Wave-driven flow over shallow reefs. *J. Geophys. Res.*, **100,** 2639-2648.

Thomson, J., S. Elgar, B. Raubenheimer, T. H. C. Herbers, and R. T. Guza, 2006: Tidal modulation of infragravity waves via nonlinear energy losses in the surfzone. *Geophys. Res. Lett.*, **33**.

Ting, F. C. K., and J. T. Kirby, 1994: Observation of undertow and turbulence in a laboratory surf zone. *Coastal Eng.*, **24,** 51-80.

Torres-Freyermuth, A., I. J. Losada, and J. L. Lara, 2007: Modeling of surf zone processes on a natural beach using Reynolds-Averaged Navier-Stokes equations. *J. Geophys. Res.*, **112**.

Torres-Freyermuth, A., and Coauthors, 2012: Wave-induced extreme water levels in the Puerto Morelos fringing reef lagoon. *Nat. Hazards Earth Syst. Sci.*, **12,** 3765-3773.

van der Westhuysen, A. J., 2010: Modeling of depth-induced wave breaking under finite depth wave growth conditions. *J Geophys Res-Oceans*, **115**.

van Dongeren, A., G. Klopman, A. Reniers, and H. Petit, 2002: High-Quality Laboratory Wave Generation for Flumes and Basins. *Ocean Wave Measurement and Analysis (2001)*, American Society of Civil Engineers, 1190-1199.

Van Dongeren, A., R. Lowe, A. Pomeroy, D. M. Trang, D. Roelvink, G. Symonds, and R. Ranasinghe, 2013: Numerical modeling of low-frequency wave dynamics over a fringing coral reef. *Coastal Eng.*, **73,** 178-190.

Vetter, O., J. M. Becker, M. A. Merrifield, A. C. Pequignet, J. Aucan, S. J. Boc, and C. E. Pollock, 2010: Wave setup over a Pacific Island fringing reef. *J. Geophys. Res.*, **115**.

Yao, Y., Z. H. Huang, S. G. Monismith, and E. Y. M. Lo, 2012a: 1DH Boussinesq modeling of wave transformation over fringing reefs. *Ocean Eng*, **47,** 30-42.

Yao, Y., Z. Huang, S. G. Monismith, and E. Y. M. Lo, 2012b: Characteristics of Monochromatic Waves Breaking over Fringing Reefs. *J. Coast. Res.*, 94-104.

Zeller, R. B., F. J. Zarama, J. S. Weitzman, and J. R. Koseff, 2015: A simple and practical model for combined wave–current canopy flows. *J. Fluid Mech.*, **767,** 842-880.

Zijlema, M., 2012: Modelling wave transformation across a fringing reef using SWASH. *Coastal Engineering Proceedings*, **1(33)**.

Zijlema, M., and G. S. Stelling, 2008: Efficient computation of surf zone waves using the nonlinear shallow water equations with non-hydrostatic pressure. *Coastal Eng.*, **55,** 780-790.

Zijlema, M., G. Stelling, and P. Smit, 2011: SWASH: An operational public domain code for simulating wave fields and rapidly varied flows in coastal waters. *Coastal Eng.*, **58,** 992-1012.